Nonlinear Dynamics of Coupled Microring Resonators

By

Siamak Abdollahi

A thesis submitted in partial fulfillment of the requirements for the degree of

Doctor of Philosophy

in

Photonics and Plasmas

Department of Electrical and Computer Engineering

University of Alberta

© Siamak Abdollahi, 2017

Abstract

Microring resonators are compact integrated optics resonators which have found a wide range application in optical communication and optical signal processing, including spectral filters, optical delay lines, switches, modulators and wavelength converters. In recent years, there has also been increased interest in studying the dynamical behaviours of nonlinear microresonators, especially in the instability regimes, for applications in all-optical switching, high-frequency optical clock generation, and fast optical pulse generation. In addition to these practical applications, the study of instability phenomena in optical microresonator systems can also provide important contributions to fundamental research on nonlinear dynamical systems.

The aim of this thesis is to investigate the nonlinear dynamics in single and coupled microring resonators in the presence of instantaneous and non-instantaneous nonlinearities. Methods based on the energy coupling and power coupling formalisms of microring resonators are developed to analyze and investigate various types of instability in these systems, including bistability, self-pulsation and period-doubling oscillations. An important objective is to study the influences of various device parameters on the threshold powers for reaching self-pulsation, with the aim of reducing these thresholds to levels that can be realistically achieved in practical integrated optics devices. In particular, in a single microring resonator with free carrier induced nonlinearity, the region of self-pulsation is constrained by a minimum free carrier lifetime. By exploring high-order instability, we show that on higher-order branches of the stability curve, the free carrier lifetime has a less restrictive influence on the nonlinear dynamics, allowing

self-pulsation to be achieved over a wider range of free carrier lifetimes and with a wider range of oscillation frequencies.

We also study the nonlinear dynamical behaviours of system of coupled microring resonators – also known as Coupled Resonator Optical Waveguides (CROWs). The aim here is that, by enhancing the spatial complexity of the nonlinear system, we can achieve novel instability effects and further reduce the threshold powers for observing self-pulsation. Using the power coupling formalism developed, we show that period-doubling oscillations can occur in a chain of coupled microring resonators with instantaneous Kerr nonlinearity, although the threshold power required to reach this instability increases with the number of resonators. On the other hand, we found that there exists an optimum CROW waveguide length for which the threshold power for observing self-pulsation is minimized. Finally, we also develop a formalism based on the Coupled Map Lattice for describing nonlinear dynamics of CROW waveguides with long length. The formalism allows us to investigate temporal instability in these structures, and potentially spatiotemporal chaos pattern forming if gain is introduced in the resonators.

Preface

The simulations, analysis, design of experiment, data analysis and writing of this thesis was done by the author under the supervision of Professor Vien Van. All the other data collection and analysis was performed by the author, excluding the following data collection step:

SEM image (Figure 5.10 (b)) was taken by Ms. Rice Mi PhD student at the department of Electrical and Computer Engineering.

Dedicated to Bahar

Acknowledgement

I would like to express my deepest gratitude to my Ph.D. advisor, Professor Van. This dissertation could not be completed without his patience and guidance.

I would like to extend my thank from bottom of my heart to my uncle and aunt Mr. Mohsen Nabi and Mrs. Mechthild Nabi who alleviated hardest days of my life by their endless support and meaningful advice.

My warm appreciation goes to my friend that I made in Edmonton. Without their deep friendship and unconditional support, I couldn't enjoy this journey. I leave them unknown out of the fear of leaving a friend behind.

During my grad studies, I had the chance to meet my wife, Bahar, who is spring of my life. I am extremely grateful for her unconditional and unrestricted love. Without being on my side, I couldn't go through my difficult times.

Last but not least I would like to express my keen gratitude to most influential teachers of my life, my parents who established my worldview by their lifetime patience, love, and support.

Contents

List of Figures

List of Tables

List of Symbols

$\varphi_{f,i}$	Steady state phase shift due to linear and nonlinear phase detune
$\varphi_{NL,i}$	Nonlinear phase detunes in the i^{th} MRR
A_{eff}	Effective area of the waveguide
$\mathbf{a}_f$	Vector of the normalized steady state stored energy of the CROW waveguide
$\mathbf{A}_f$	Matrix of Steady state of the normalized power of the i^{th} MRR
$A_{f,i}$	Vector of the normalized steady state stored power of the CROW waveguide
$a_{f,i}$	Steady state normalized energy of the i^{th} MRR
a_i	Normalized stored energy of the i^{th} MRR
a_{rt}	Round trip loss of Microring resonator
C	Free space EM wave speed
C_a	Ambipolar Auger recombination
D	Duty Cycle of pulse train
$\mathbf{D_{f,i}}$	Steady state traveling power in the i^{th} MRR at the $4^{/4}$ arc
E_{in}	Input optical field of the Bus waveguide
E_{out}	Output optical field of the Bus waveguide
F	Finesse Factor of the Microring Resonator
f	Discrete local map
$F_{modulation}$	Modulation frequency of pulse train
f_{sp}	Frequency of Self pulsation
g	Gain or loss of the Microring Resonator
H	Coupling Matrix of PC formalism
ħ	Reduced plank constant
J	Jacobian matrix of time-delay and time-differential equation
k_0	Wave number
$\mathbf{K_{coupling}}$	Coupling coefficient matrix of the CROW waveguide
L_{eff}	Effective length of waveguide
L_z	Length of SOI-waveguide
m	Resonance number mode
$\mathbf{M}_{E\_L}$	Linear Coupling Matrix of EC formalism
$\mathbf{M}_{E\_NL}$	Nonlinear Coupling Matrix of EC formalism
n_0	Linear index of medium
n_2	Kerr coefficient

n_{core}	Index of core of waveguide
N_{dc}	Steady state density of generated free carrier by TPA
n_{eff}	Effective index of dielectric Waveguide
n_g	Group index of dielectric waveguide
N_i	Generated free carrier density in the i^{th} MRR
$N_{f,i}$	Steady state free carrier density in the i^{th} MRR
n_t	Index of discrete time
n_z	Index of arc segment
P	Induced polarization
$P_{a,i}$	Steady state stored power in the i^{th} MRR
p_{ac}	AC part of propagated optical wave along the waveguide
P_{bias}	DC- level of input pulse train
P_{dc}	Steady state power in the waveguide
P_{in}	Power of input optical wave
P_L	Linear induced polarization
P_{NL}	Nonlinear induced polarization
P_{out_ac}	AC part of propagated optical wave at the end of waveguide
Q	Quality factor
R	Radius of Microring Resonator
S	Matrix of input optical wave of CROW
S	Surface recombination velocity-Front
$S^{'}$	Surface recombination velocity-Back
t	Time
T_{Off}	Off interval of pulse train
T_{On}	On interval of pulse train
T_{rt}	Induced round trip delay by MRR
U(t)	Heaviside function
v_g	Group velocity
V_π	Half-wave voltage
z	Eigenvalue in discrete space
α_0	Linear loss
α_{NL}	Round trip nonlinear loss of MRR
β_{TPA}	Two photon absorptions

γ	Total loss in the MRR including roundtrip loss and coupling to bus waveguide
γ_{FCA}	Strength of nonlinearity associated with free carrier absorption
γ_{kerr}	Strength of nonlinear frequency detuning due to Kerr effect
$\Delta\varphi_{L,i}$	Linear phase detunes of i^{th} Cavity
Δn_{NL}	Nonlinear index change
ΔP	AC power
$\Delta\Theta_i$	Phase detune between I and i+1 MRR
$\Delta\omega_i$	Frequency detuning of the i^{th} MRR
$\Delta\omega_{NL,i}$	Kerr or free carrier dispersion induced nonlinear frequency detune
$\varepsilon\varphi_{NL,i}$	Perturbation term of induced nonlinear phase shift in the i^{th} MRR
ε_0	Free space permittivity
$\varepsilon_{a,i}$	Perturbation term of the stored Energy of the i^{th} MRR
$\varepsilon_{A,i}$	Perturbation term of the stored Power of the i^{th} MRR
$\varepsilon_{N,i}$	Perturbation term of Free carrier density of the i^{th} MRR
ζ_{FCA}	Strength of FC induced nonlinear phase detune
ζ_{Kerr}	Strength of Kerr induced nonlinear phase detune
η	The ratio of free carrier absorption to free carrier dispersion
κ_i	Coupling strength between i^{th} and $i+1^{th}$ MRR
λ	Resonant Wavelength of the MRR
Λ	Phase detune matrix
μ_i	Energy coupling coefficient between i^{th} and $i+1^{th}$ MRR
σ_{FCA}	Free carrier Absorption cross-section
σ_{FCD}	free carrier dispersion volume
τ_0	FC density independent Free carrier lifetime
τ_{Aug}	Auger recombination lifetime
τ_b	Bulk recombination lifetime
τ_c	Critical carrier lifetime
$\tau_{cp,i}$	Transmission rate of the i^{th} MRR
$\tau_{eff,fc}$	Decay lifetime associated with free carrier
$\tau_{eff,Off,fc}$	Effective free carrier lifetime of optical pulse during off time
$\tau_{eff,Off,out}$	Effective decay rate of optical power during off time
$\tau_{eff,On,fc}$	Effective free carrier lifetime of optical pulse during on time
$\tau_{eff,On,out}$	Effective decay rate of optical power during on time

$\tau_{eff,out}$	Small signal of decay rate of optical power
τ'_{fc}	Small signal of free carrier lifetime
τ_{fc}	Free carrier lifetime
τ_n	Normalized free carrier lifetime
$\tau_{ph,i}$	Cavity lifetime of the i^{th} MRR
τ_{SIR}	Surface interface recombination lifetime
τ_{SRH}	Shockley-Reed Hall lifetime
χ^n	n^{th}-order susceptibilities
Ω	Associated phase of oscillation
ω_i	Resonance Frequency of i^{th} MRR
Φ	Angle of eigenvalue

List of Abbreviations

CML	Coupled Map Lattice
CROW	Coupled Ring Oscillator Waveguide
EC	Energy Coupling
FCA	Free Carrier Absorption
FCD	Free Carrier Dispersion
MRR	Microring Resonator
NLSE	Nonlinear Schrodinger Equation
PC	Power Coupling
ROC	Region of Convergence
SBS	Stimulated Brillouin Scattering
SRS	Stimulated Raman Scattering
TO	Thermo-Optic
TPA	Two photon absorptions
XPM	Cross-Phase Modulation
SEM	Scanning Electron Microscope

EDFA	Erbium Doped Fiber Amplifier
PD	Power Detector

1 Introduction

With the invention of the laser at the beginning of the 1960's, a new branch of optics known as nonlinear optics was born [1]. This regime of operation is characterized by high intensity of the optical laser beam, which causes the relation between the optical field and the induced polarization of the medium to become nonlinear. This nonlinear polarization gives rise to new physical phenomena which are not observed in the linear regime of operation at lower optical intensities. The observation of harmonic generation effect by G. Winreich in 1961 was the first experimental work in this area [2].

A variety of instantaneous and non-instantaneous optical nonlinearities can be observed in semiconductor materials such as silicon [3]. Instantaneous nonlinearity such as Kerr effect arises from the interaction of the optical field with bound electrons, with the response time in the order of a few femtoseconds [4], which causes the refractive index of the medium to depend on the applied optical intensity [5]. On the other hand, nonlinearity due to free carrier dispersion (FCD) [6] is a non-instantaneous effect with interaction times ranging from 1ps to 10μs [3]. In this effect, a high-intensity optical signal generates free carriers (FC) in the semiconductor material through the two-photon absorption (TPA) process, and these generated free carriers in turn induce a change in the refractive index and absorption of the material. Soref et al. have derived an empirical relation for the index and absorption changes due to free carriers for crystalline silicon [7]. The response time of FCD and free carrier absorption (FCA) is determined by the

relaxation time of the generated free carriers in the medium, which can range from picoseconds to microseconds. In addition to Kerr and free carrier induced nonlinearities, thermo-optic (TO) effect may also arise from the generated heat due to nonlinear absorption (TPA and FCA) of light in the material [8]. The thermo-optic effect typically has much slower response time than Kerr and FC induced nonlinearities, in the order of micro to milliseconds. It is also worth mentioning that the relaxation times of different nonlinear effects are highly dependent on the materials [4, 8, 9].

In this thesis, to investigate the nonlinear dynamic behaviors of optical micro-resonators due to instantaneous and non-instantaneous nonlinearities, we choose chalcogenide glass and silicon as the nonlinear optical media. Chalcogenide glass is a material with large Kerr coefficient and almost instantaneous response [10]. Silicon is a widely-used material for integrated optical devices which possesses both instantaneous Kerr effect and non-instantaneous FC induced nonlinearities.

In a nonlinear optical waveguide, two common nonlinear effects that can be observed are self-phase modulation (SPM) [11] and cross-phase modulation (XPM) [12]. SPM occurs when a high-intensity optical pump changes the effective index of the waveguide, which in turn induces a nonlinear phase shift in the pump signal. When a low-intensity probe signal also co-propagates with the high-intensity pump, the probe signal experiences the nonlinear index change in the medium caused by the pump so that its phase is also modified. This effect is known as cross-phase modulation. The propagation of an optical signal in a nonlinear waveguide can be described by the Nonlinear Schrödinger Equation (NLSE). This equation can be modified to account for various material nonlinearities,

including instantaneous Kerr nonlinearity, two-photon absorption, free carrier dispersion and free carrier absorption [13].

In addition to these material nonlinearities, Stimulated Raman scattering (SRS), Stimulated Brillouin scattering (SBS), and four wave mixing (FWM) are other significant nonlinear effects in a semiconductor waveguide [1, 3]. SRS and SBS can provide optical gain but do not alter the nonlinear dynamic behavior of an optical system with feedback, such as in a microresonator [1]. For this reason we do not consider these effects in this thesis. Four wave mixing is a process which involves energy transfer between at least two optical waves with different wavelengths under appropriate phase matching condition. We also do not consider this effect in the microresonators studied in this thesis.

In a nonlinear optical system with feedback, such as in an optical resonator filled with a nonlinear material, nonlinear dynamic behaviors such as self-pulsation [14], period doubling [15], and chaos [16] can arise. An optical resonator also serves to enhance the nonlinear effect by amplifying the optical intensity inside the cavity. Microring resonators (MRRs) are the simplest and most robust optical resonators that can be realized in integrated optics. An MRR device consists of a closed loop waveguide (ring) acting as the resonator and a straight waveguide for coupling light into and out of the ring. Coupling between the straight waveguide and the ring waveguide is achieved through the evanescent waveguide fields [17]. Near a resonance frequency, a large optical intensity is built up in the ring cavity, which serves to amplify the nonlinearity. Thus, nonlinear effects can be observed with less optical power in an MRR compared to a straight waveguide with the same cross-section. The ring cavity also provides a natural

feedback mechanism which gives rise to richer nonlinear dynamic behaviors than in a straight waveguide. In addition, multiple MRRs can be arranged in a coupled resonator array, which greatly enhances the spatial complexity of the light-confining structure and enables even more complex nonlinear dynamic behaviors to be observed.

The objective of this thesis is to investigate the nonlinear dynamic behaviors in single and coupled microring resonators, with instantaneous and non-instantaneous nonlinearities. These dynamic behaviors can have novel applications in optical information technology, such as all-optical switching and the generation of high-frequency optical clocks. In the next section, we provide more details on the background and motivation of our research.

1.1 Background and Motivation

In the linear regime of operation, MRRs have a broad range of applications in optical communication and information processing, for example, as wavelength filters, multiplexers and demultiplexers [18-20]. When made of a highly nonlinear material, these devices can also exhibit rich nonlinear dynamic behaviors such as self-pulsation, bistability, period doubling and even chaos [14-16]. These effects have many interesting and important applications for optical communication and all-optical signal processing. A particular application of interest in our research is the realization of high-frequency optical oscillators. Local oscillators are used to generate harmonic signals and are essential components in coherent optical communication systems, which employ advanced modulation-coding/coherent receiver for improving spectral efficiency [4]. Local oscillators are typically built with a Mach-Zehnder modulator and an electrical

microwave signal generator, as shown in Figure 1.1.

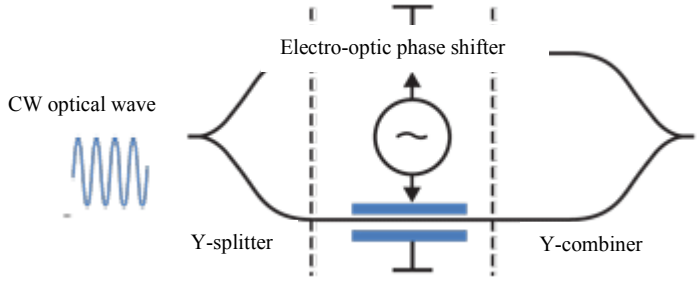

Figure 1.1, Schematic of MZI as an electro-optic local oscillator

The main drawback of this E/O (electro-optical) oscillator is fabrication complexity, since it requires integration of electrical and optical parts, as well as the speed limitation of the electronics. All-optical oscillators may offer a better alternative. Mode-locked and DFB lasers can be used to generate optical clock signals [2] but they are not compatible with silicon photonics technology. Optical comb generation by FWM in a silicon microring resonator is another solution [5], although the performance of the oscillator is degraded by FCA, which reduces the efficiency of the FWM process [3].

Self-pulsation (SP) and Ikeda instability in MRRs provide a novel way to generate optical clock signals which can be simpler and more cost effective compared to techniques based on mode-locked lasers and optical comb generation. There is particularly great interest and potential value in endeavoring to achieve self-pulsation and other nonlinear dynamic behaviors in silicon MRRs, given the prevalence of silicon photonics technology in integrated optics. However, there exist long standing obstacles to achieving these behaviours in practice, especially on an integrated optics platform. For example, we need pump signals of very high optical intensities to observe instability in an integrated MRR and in many instances, the required optical intensity is so high that it may cause

permanent damages to the photonic chip. Another challenge is that self-pulsation in an MRR with non-instantaneous nonlinearity is limited by the relaxation time of the nonlinear medium. As shown in [21] and [22], there exists an upper limit on the FC lifetime in a semiconductor MRR for FC-induced SP to be achieved. Unfortunately, this critical relaxation time constant is much shorter than the typical FC lifetime in a silicon waveguide, so that SP due to FCD has not been experimentally observed in a silicon MRR.

Given these challenges, we are motivated to explore new mechanisms and new device structures that could enable feasible and realistic demonstrations of these nonlinear effects on an integrated photonic platform. In particular, we will investigate the higher-order nonlinear dynamics in a single MRR, as well as nonlinear dynamics of a chain of coupled MRRs. For the latter case, our hypothesis is that by increasing the length of a chain of coupled MRRs, we can decrease the threshold power required to achieve instability due to enhancement in the nonlinear interaction length. Also, the spatial complexity of coupled MRRs compared to a single resonator may alter the nature of the nonlinear interactions, allowing self-pulsation to be observed at longer material relaxation times.

Another objective of the thesis is to develop rigorous models for analyzing and investigating nonlinear dynamics of coupled MRRs. To date, simple models have been used to analyze the nonlinear behavior of single MRRs with instantaneous and non-instantaneous nonlinearities. To investigate the much richer nonlinear dynamics of coupled MRRs, we need to develop comprehensive models and analysis methods in the

time and frequency domains. These models are not only suitable for analyzing the stability of a finite chain of coupled MRRs, but can also be used to investigate the spatiotemporal behavior of optical propagation in an infinitely long chain of coupled MRRs.

1.2 Literature Survey

In the linear regime, MRRs have important applications in integrated photonics as spectral filters [23], switches [24], optical delay lines [25], label-free biosensors [26], and modulators [27]. In addition to these well-developed applications, comprehensive studies have been performed to model and analyze the static and dynamic behaviours of MRR devices [28-37]. The models used can be divided into two broad categories: energy-time coupling and power-space coupling models. In the energy-time coupling (EC) model, we treat an MRR as a lumped oscillator which supports only a single resonance mode [22]. On the other hand, the power-space coupling (PC) model treats an MRR as a traveling wave resonator with an infinite number of resonance modes [37]. The EC model is strictly valid only for weak coupling and at frequencies near a resonance mode, whereas the PC model is valid for all coupling values and at all frequencies. Both of these models can be extended to include optical nonlinearities in the MRR.

So far, several numerical and experimental studies have been performed on single MRRs with instantaneous and non-instantaneous optical nonlinearities [28-37]. Most of these works focused on third-order harmonic generation, wavelength conversion, frequency comb generation, entangled photon generation, soliton wave generation [38], ultrashort pulse generation [39], and optical bistability [40]. On the other hand, nonlinear

dynamical and instability effects such as self-pulsation, period doubling, and chaos have been investigated to a much lesser extent, due to the high optical intensities required to observe these phenomena.

These effects can have potential applications in optical communication and optical computation, such as clock generation, clock recovery, cryptography, Boolean logic gates, and optical memories [41-45].

The Ikeda instability mechanism could be used as a technique to generate Tera hertz (THz) waves. Although the duty cycle of generated waves by Ikeda instability is a constant value of 50%, the oscillation frequency of the generated signal can be increased by reducing the ring radius. In particular, for silicon MRRs, terahertz Ikeda oscillations can potentially be achieved for ring radius around 1μm.

Another possible application of the nonlinear dynamics of MRR is in the encryption-decryption scheme. By increasing the input power beyond the Ikeda instability region [16], the system behaves chaotically. The threshold for observing chaos in a single MRR is beyond the laser damage threshold but this mechanism happens in chain of coupled micoring resonators. In this region, for any input, the output is a sequence of pseudo random numbers that could be used as an encryption (private) key. It is worth to mention that a dynamic map of MRR has two-dimensional nature because of the existence of real and imaginary parts of an optical field. Due to the 2D nature of this map, this dynamic behavior is suitable for performing real time chaotic encryption on image or video stream. In this dissertation, we will focus on the nonlinear dynamic behaviours of single and coupled MRRs in the presence of Kerr nonlinearity, free carrier dispersion, and free

carrier absorption. We will neglect the thermo-optic effect because its relaxation time is much slower than the time scales of the nonlinear dynamic processes and the operating speeds of related applications which we are interested in studying.

A variety of nonlinear dynamic behaviours can occur in a nonlinear optical resonator such as in an MRR with Kerr nonlinearity. These include bistability, self-pulsation, Ikeda instability and chaos. Bistability occurs when two stable power (or intensity) levels can exist in an optical resonator for the same input optical power. This phenomenon can be used to realize all-optical switches, logic gates, and optical memory. Boolean logic gates based on optical bistability have been demonstrated in [46]. Bistability has also been used to implement an optical transistor in [47], for applications in amplification and switching. Compared to other instability phenomena such as self-pulsation and chaos, bistability occurs at a lower power threshold and for a wider range of phase detunings of the resonator. For this reason, it is much easier to observe bistability than other nonlinear dynamical phenomena.

Self-pulsation (SP) refers to the generation of a pulse train, or amplitude oscillations, in an optical resonator from an input continuous-wave (CW) light beam. An essential condition for achieving SP in a nonlinear MRR is that the relaxation time constant of the nonlinear medium must be much longer than the roundtrip time of the resonator. In general, the frequency of the self-oscillations highly depends on the linear phase detune of the resonator. If the medium relaxation time constant is much shorter than the roundtrip time of the MRR, oscillations known as Ikeda instability (or period doubling) can occur. Ikeda instability, which was first predicted in a cavity with instantaneous Kerr

nonlinearity [48], is similar to self-pulsation but the period of oscillations is exactly equal to twice of the cavity roundtrip time and does not depend on the input power or the linear phase detune [49]. Self-pulsation and Ikeda instability have been suggested to have potential applications for high-speed optical clock generation for coherent communication systems. At very high optical intensities, a regime of behaviour called chaos exists, where the intensity in the cavity fluctuates randomly with time [16]. One potential application of chaotic behaviour in a nonlinear MRR is for random sequence generation.

In 1983 Gibbs et. al. first demonstrated Ikeda instability in a hybrid electrical-optical bistable system [50]. In this hybrid system, the time delay feedback mechanism was realized with a microcontroller, photodetector, A/D and D/A converters. By further increasing the input CW optical power, the system was observed to transition from period doubling oscillations to chaotic behaviour. The authors also studied in detail the effect of the ratio of the nonlinear relaxation time constant to the feedback time delay on the characteristics of the self-oscillations. Nakatsuka et. al. later observed period doubling oscillations and chaos in a nonlinear optical fiber ring cavity [51]. It should also be mentioned that different research groups have reported observations of SP with longer periods of oscillation than period doubling in various hybrid and intrinsic nonlinear systems. Konthasinghe et. al. showed SP effect in a nonlinear Fabry-Perot cavity with an extended period of oscillation of half a microsecond [52]. The low frequency of oscillation is attributed to thermo-optic nonlinearity, which has long relaxation time constant. The development of microfabrication technology in recent years has enabled microcavities such as microring resonators and microdisks with very high quality factors

(Q factors) to be fabricated. The high optical intensities achieved in these microcavities can help substantially reduce the power thresholds required for observing nonlinear dynamical effects. Zhang et.al. observed SP in a high-Q silicon microdisk with 12 μW continuous input power [53]. However, the period of oscillations was relatively slow (1 μs), which was attributed to the competition between two nonlinear effects of opposite signs in the microdisk, namely, free carrier dispersion and the thermo-optic effect.

In addition to the experimental works mentioned above, there have also been several theoretical works studying the nonlinear dynamics of single and coupled MRRs. The energy-time coupling (EC) formalism is the main foundation of these works. M. Armilla studied self-pulsation in a single MRR with FCD. The existence of a critical FC lifetime for observing SP in a micro-resonator has been proved in [21, 22, 54] by linear stability analysis based on the EC model. With respect to coupled MRRs, B. Maes et. al. [35] analyzed the stability behavior of two and three coupled MRRs with instantaneous Kerr nonlinearity using the EC model and predicted SP behaviour over specific ranges of input powers.

The wide application of the EC formalism to study the nonlinear dynamics of MRRs is mainly due to the relative analytical simplicity of the model. However, since the EC formalism only models a single resonance mode of the cavity, it fails to predict some important nonlinear effects, especially at high optical intensities. On the other hand, the PC formalism explicitly accounts for the nonlinear delayed feedback in the system [37, 49, 55] and can model the interactions between adjacent resonance modes. As a result it provides a more accurate picture of all the nonlinear dynamics that occur in an MRR or in

a chain of coupled MRRs. In spite of this advantage, there have been very few studies of instability in MRRs based on the PC model. For example, high-order instability, which does not exist in the EC model, has not been investigated in an MRR using the PC model. Although Ikeda instability is known to exist in a single resonator, its existence in coupled microresonators has not been shown. This type of instability relies on the mixing of adjacent resonator modes and thus can only be described by the PC formalism. In addition, a detailed comparison between the EC and PC models in terms of the predicted nonlinear dynamics of single and coupled MRRs has not been performed. Such a comparison would help us understand the limitations of the EC model and gain deeper insights into the physics of the instability behaviors in these devices.

As previously stated, a major focus of this thesis is the nonlinear dynamics of coupled MRRs. A chain of coupled MRRs was originally proposed by A. Yariv as a medium for transporting optical signals similar to an optical waveguide [56]. The structure is thus known as a coupled-resonator optical waveguide (CROW). Propagation of an optical wave in a nonlinear CROW waveguide has been studied using the scattering matrix method [57]. The main drawback of this method, however, is the very large computation effort required for long CROW waveguides. Both the EC and PC models can be used to study nonlinear dynamics of short chains of coupled MRRs, but they are not suitable for analyzing very long CROW waveguides due to the large matrix systems involved. In this thesis, we will develop an alternative method for analyzing the spatiotemporal field patterns of optical propagation in a long CROW waveguide. The method is based on the Coupled Map Lattice (CML) theory [58], which has been used to describe the dynamic behaviours of extended systems in diverse fields such as electrical circuits [59] and

chemical reactions [60]. Here, we will apply the CML theory to study the problem of optical propagation in a long nonlinear CROW waveguide.

1.3 Theoretical Background

The main focus of this thesis is to investigate the nonlinear dynamics of MRRs. In this section, we will review the theoretical foundations of our work, including the analytical descriptions of a microring resonator and a brief review of the fundamental concepts of nonlinear optics and nonlinear dynamic systems.

1.3.1 Microring resonators

A common configuration of a MRR is shown in figure 1.2. The device consists of a straight waveguide called a bus waveguide and a circular waveguide which forms the microring resonator. The microring has a radius R and is evanescently coupled to the bus waveguide with the coupling strength given by a field coupling ratio κ_1. The roundtrip amplitude attenuation in the microring waveguide is denoted as a_{rt}. At wavelengths satisfying the condition $2\pi R = m\lambda/n_{eff}$, where n_{eff} is the effective index of the microring waveguide and m is an integer, constructive interference of light waves occurs in the microring corresponding to the resonance mode number m.

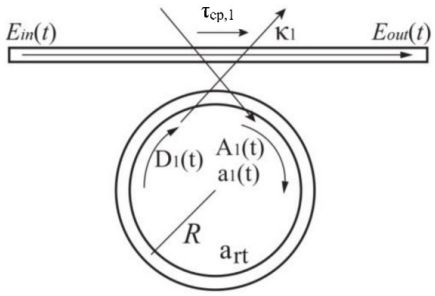

Figure 1.2, Schematic of Microring Resonator

The universal coupling matrix [61] determines the relation between the wave circulating in the microring (A_1 and D_1) and the input and output waves (E_{in} and E_{out}) propagating in the bus waveguide as follows,

$$\begin{bmatrix} A_{f,1} \\ E_{out} \end{bmatrix} = \begin{bmatrix} -j\kappa_1 & \sqrt{1-\kappa_1^2} \\ \sqrt{1-\kappa_1^2} & -j\kappa_1 \end{bmatrix} \begin{bmatrix} E_{in} \\ D_{f,1} \end{bmatrix} \tag{1.1.a}$$

$$D_{f,1} = a_{rt} e^{-j\Delta\varphi_{L,1}} A_{f,1} \tag{1.1.b}$$

In the above equation, a_{rt}, κ_1, and $\Delta\varphi_{L,1}$ are roundtrip loss, the field coupling coefficient and the linear phase detune, respectively. $A_{f,1}$ and $D_{f,1}$ are the steady-state solutions of $A_1(t)$ and $D_1(t)$, respectively. From the above equation, we can find the transfer function relating the field $A_{f,1}$ inside the microring and input field E_{in} as

$$\text{Transmission} = \frac{A_{f,1}}{E_{in}} = \frac{-j\kappa_1}{1 - a_{rt}\sqrt{1-\kappa_1^2}\, e^{-j\Delta\varphi_{L,1}}} \tag{1.2}$$

A typical spectral response of the power in the microring resonator is shown in figure 1.3.

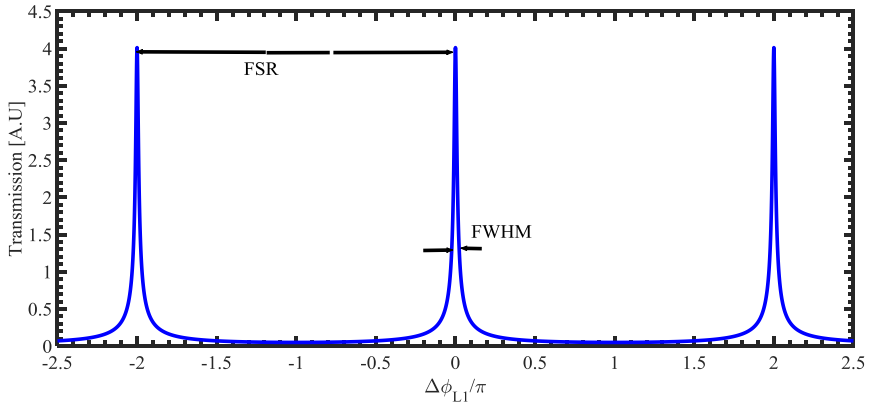

Figure 1.3, Power transmission ratio (P_{out}/P_{in}) vs linear phase detune of an MRR.

We can characterize the performance of an MRR by three parameters: the free spectral

range (FSR), the full width at half maximum (FWHM) (or the 3dB bandwidth of the resonance) and the quality factor Q.

The FSR is the spacing between two successive maxima or minima of the transmitted optical power of the MRR. The FSR can be computed from

$$FSR \approx \frac{\lambda^2}{n_g 2\pi R} \tag{1.3}$$

where λ and n_g are the resonant wavelength and the group index of the microring waveguide, respectively. The quality factor (Q-factor) of an MRR measures the sharpness of the resonance and is given by

$$Q = \frac{\lambda}{FWHM} \tag{1.4}$$

where λ is the resonant wavelength and FWHM is the 3-dB bandwidth in terms of wavelength.

1.3.2 Nonlinear Optics

Nonlinear optics is a branch of optics that studies how an optical wave behaves in a medium with nonlinear induced polarization. The dependence of the polarization P of a dielectric medium on the electric field E of the light wave can be expressed in terms of the Taylor series [62],

$$P = P_L + P_{NL} = \varepsilon_0\left(\chi^1 E + \chi^2 EE + \chi^3 EEE\right) \tag{1.5}$$

where P_L and P_{NL} are the linear and nonlinear polarizations, ε_0 is the vacuum permittivity, and χ^n is the n^{th}-order susceptibility of the medium. In centro-symmetric materials such

as silicon, fused silica and chalcogenide glass, the even power terms in equation (1.5) are absent. In this case, the most dominant nonlinear term is the third-order term, so these materials are said to have third order nonlinearity. Since we will be mainly interested in silicon and chalcogenide materials in this thesis, we will focus only on the third order nonlinearity, which is also known as Kerr nonlinearity. The real part of χ^3 gives rise to various nonlinear effects such as self-phase modulation (SPM), cross-phase modulation (XPM), and four-wave mixing (FWM) [62]. The imaginary part of χ^3 describes a nonlinear absorption process known as two-photon absorption (TPA). TPA occurs when the energy of the incident photon is larger than half the band gap energy of the material. The absorption of a pair of photons generates a free electron hole pair, which induces a refractive index change in the medium known as free carrier dispersion (FCD) and causes additional optical loss known as free carrier absorption (FCA). Different types of nonlinearities have different response times, and for the purpose of this thesis, we will categorize them as instantaneous and non-instantaneous nonlinearities. Instantaneous nonlinearities such as the Kerr effect and TPA have very fast response time in the order of a few femtoseconds. On the other hand, FC induced nonlinear effects (FCD and FCA) and thermo-opitc effect have much slower response times which are limited by the rates of FC recombination (ps to ns) or by thermal heat dissipation (μs to ms) [5]. These effects are thus characterized as non-instantaneous.

1.3.3 Nonlinear Dynamic Systems

The temporal behaviors of a nonlinear MRR can be analyzed by treating the device as a nonlinear dynamic system. In general, a given system is dynamic if its state spaces

evolve with time according to a transformation rule. Two types of transformation rules exist which determine the behavior of the dynamic system. Continuous-time systems are governed by equations that describe the time derivatives of the system variables in terms of their current and past values. In this case, the system variables vary continuously in time. For example, the equation of motion describing the path of the earth in the solar system is a continuous dynamical system. In discrete-time systems, the transformation rule is a set of equations which specify how the new values of the system variables are updated from the values at the current and discrete time points in the past.

A set of equations describing a continuous-time dynamical system can have the following form

$$\dot{x}(t) = f(x(t)). \tag{1.6}$$

In the above equation, x is a state containing the system variables and f is a given function of the system variables. A set of equations describing a discrete-time dynamical system can have the following form

$$x^{n_t+1} = F\left(x^{n_t}\right) \tag{1.7}$$

In the above equation, the function F updates the value of x at the next time step, x^{n_t+1}, based on the value at the current time step, x^{n_t}. The function F is also referred to as an iterated map which takes the system from one-time step to the next.

A nonlinear dynamical system is one whose function f or F is a nonlinear function of the state variable. In a nonlinear dynamical system, the output is not necessary a single state,

i.e., multiple outputs can result from a single input. For example, a dynamical system is bistable if it has two possible stable states for a given input. Also, a system may fluctuate periodically between two or more states. This phenomenon is known as self-pulsation. If there is no pattern for the fluctuations between the different states, the dynamical system is said to be in a chaotic state and the output of the system is very sensitive to the initial condition. The behaviors of a nonlinear dynamic system can be determined by applying linear stability analysis around a fixed point of the system. For a linearized dynamical system, the location of the poles in the s-plane (for continuous time) and Region of Convergence (ROC) (for discrete time) determines the dynamical behavior of the system. This procedure will be used throughout this thesis to investigate the nonlinear dynamics of MRR devices.

1.4 Research Objectives

The aim of this thesis is to investigate the nonlinear dynamics in single and coupled MRRs with instantaneous and non-instantaneous nonlinearities. The specific objectives of the research are as follows:

- We perform a comparison between the EC and PC formalisms for predicting instability in a single MRR with instantaneous Kerr nonlinearity. The comparative study will help us understand the differences between these two models and gain further insights into the physics of self-pulsation phenomena.
- We aim to formulate a PC model for analyzing instability in a single MRR with FC induced nonlinearity. We are particularly interested in exploring high-order instability with the aim of overcoming the FC lifetime limit for reaching self-pulsation in silicon MRRs.
- We extend the EC and PC formalisms to develop a transfer matrix method to

study instability in a chain of coupled MRRs with instantaneous and non-instantaneous nonlinearities. The aim is to exploit the long nonlinear interaction lengths in these structures to reduce the power thresholds required to reach self-pulsation and Ikeda instability. Currently, the power thresholds for reaching SP and Ikeda instability typically exceed the limit that can be handled by silicon integrated photonic devices. It is thus of practical interest to reduce the power requirement to more realistic levels.

- The transfer matrix method developed above is suitable only for short chains of coupled MRRs. To analyzing spatiotemporal dynamic instabilities in a long chain of coupled MRRs, such as in a nonlinear CROW waveguide, we aim to develop a hybrid EC-PC formalism based on the Coupled Map Lattice (CML) theory. The formalism will allow us to study the spatiotemporal field patterns in extended chains of coupled MRRs with instantaneous nonlinearity.
- In nonlinear MRR devices with FC induced nonlinearity, the FC lifetime is a critical parameter influencing the nonlinear dynamics of the device. In order to better understand the influence of free carriers on light propagation in a silicon waveguide, especially at moderate to high input optical powers, we aim to develop a model and numerically investigate the relaxation time constant of the transmitted optical power in a silicon waveguide due to various FC recombination mechanisms. We will perform power transmission experiments with silicon waveguides under pulse width modulation excitation to validate the simulation results and the model.

1.5 Thesis Organization

This thesis is organized into six chapters. In Chapter 2, we study in detail the nonlinear dynamics of a single MRR predicted by the EC and PC models. Using the PC model, we show for the first time that the high-order self-pulsation can occur in a silicon MRR due to Kerr and FC induced nonlinearities. In Chapter 3, we investigate the nonlinear dynamics of short chains of coupled MRRs using the EC and PC formalisms. We will

present a transfer matrix method which allows us to analyze the stability of short chains of nonlinear coupled MRRs. In Chapter 4, we derive a Coupled Map Lattice formulation to describe long and infinite chains of nonlinear coupled MRRs. The formulation enables us to we study nonlinear optical propagation in extended spatial networks comprising of coupled MRRs. In Chapter 5, we investigate the effect of various FC recombination mechanisms on the relaxation time of the optical power in a silicon waveguide through numerical studies and experimental measurements. Chapter 6 concludes the thesis with a summary of the research and our contributions, and provides suggestions for future work.

2 Nonlinear Dynamics in a Single Microring Resonator

Over the past two decades, integrated photonics has attracted a lot of attention for applications in optical information technology because of the deep miniaturization and high level of integration these devices can offer [63]. Among the different candidate materials for integrated photonic circuits, silicon has emerged as an important photonic material because of its compatibility with the CMOS technology and low cost of fabrication [63]. Various passive and active silicon integrated photonic components such as couplers, microring resonators, intensity and phase modulators, Raman lasers and photodiodes have been developed. For nonlinear optics applications, silicon can provide a large nonlinearity through the TPA and FCD effects. However, the response time of this nonlinearity is limited by the FC lifetime, which may not be fast enough for certain applications. An alternative photonic material which has low loss at the telecommunication wavelengths and large instantaneous Kerr effect is chalcogenide glass [64]. Both silicon and chalcogenide have high refractive indices, which enable strong light confinement in the waveguide core leading to enhanced nonlinear effects. For linear device operations, the strong optical nonlinearity can cause unwanted effects such as crosstalk between signals [65] and signal distortion [66]. On the other hand, these nonlinear effects have also been exploited for applications such as all-optical switching and optical logic gates [5, 18, 24, 67, 68].

Among various photonic components, those with an internal or external feedback mechanism can exhibit rich nonlinear dynamic behaviours such as bistability, self-

pulsation (SP), Ikeda instability (or period doubling), and even chaos [14-16, 21, 22, 50, 51]. These phenomena can potentially be exploited to build components for coherent and incoherent optical systems, such as thresholders, discriminators, high-frequency optical clocks and random sequence generators [69-71]. In addition, feedback leads to a large buildup of optical intensity inside the device through resonance, which enhances the optical nonlinearity and reduces the optical power requirement. Among various integrated photonic devices with built-in feedback mechanisms, microring resonators are simple to fabricate and have high Q factors and simple coupling scheme. For this reason, we will focus mainly on MRR devices in this thesis, although the analyses can also be extended to other types of optical resonators such as Fabry-Perot resonators and photonic crystal cavities.

In a nonlinear system with feedback, the ratio of the relaxation time constant of the nonlinearity to the feedback delay (e.g., roundtrip delay in an MRR) determines the different oscillation behaviours, as discussed in detail by Silberberg et.al. [48]. If the nonlinearity relaxation time constant is much longer than the feedback delay, SP oscillations occur. In this case, a high-intensity input CW signal will generate a train of optical pulses with a variable period of oscillation. In particular, the oscillation frequency highly depends on the relaxation time constant of the nonlinearity and the linear phase detune of the resonator [14, 21, 22]. In the opposite case where the relaxation time constant of the nonlinearity is much shorter than the feedback delay, Ikeda instability or 2^n-period doubling can occur. The oscillation period in this case is exactly equal to 2^n (n = 1, 2, 3,…) of the feedback delay and is independent of the input power, phase detune and other physical linear and nonlinear parameters of the structure [16,

50, 51]. This type of oscillations can be observed in a feedback system with instantaneous nonlinearity such as chalcogenide or fused silica MMR [15].

There has recently been a resurgence in research interest in self-pulsation and period doubling oscillations in nonlinear optical systems, with various theoretical and experimental studies reported by different research groups. Abrams et. al. demonstrated bistability and self-pulsation in an ultra-small volume silicon microdisk [72]. The observed threshold input power for Bistability (BI) and SP was 45μW and 120μW, respectively. Although the source of nonlinearity is due to free carriers, the fact that the SP frequency was only about 1MHz reveals that the oscillations were caused by the thermo-optic effect with the heat generated from free carrier absorption (FCA) [72]. Zhang et. al. demonstrated numerically and experimentally bistability and SP in a 10μm-radius silicon MRR. Again the observed SP was due to the thermo-optic effect with the oscillation frequency in the 8-11 MHz range for input powers of 65-121 mW [73]. Despite using a reverse-biased PIN diode in the MRR to reduce the FC lifetime to 12 ps, the authors were unsuccessful in achieving high-speed SP caused by FCD. They believed that such high-frequency SP was not observable because of the low extinction ratio of the MRR due to the short FC lifetime.

Chen, Armaroli, and Vaerenbergh analyzed in detail bistability and self-pulsation in an MRR with finite nonlinear relaxation time [14, 21, 22, 54]. They showed that an upper limit of the relaxation time exists for SP. However, since their analysis was based on the mean field method (also known as the EC method), they could not predict Ikeda instability in the device. As demonstrated by Ikeda in his original paper on the 2^n-period oscillation phenomenon [15], a time delay due to a feedback mechanism must be

introduced into the system in order for this type of oscillations to exist. It was Gibbs et. al. who first demonstrated period doubling in an electro-optical hybrid bistable device [50]. Subsequently, Nakatsuka et. al. also showed period doubling in a ring cavity with an optical fiber as the nonlinear medium [51]. However, there has not been any successful experimental demonstration of Ikeda oscillations on an integrated photonic platform, mainly because of the prohibitively high optical power required to observe such oscillations.

In this chapter, we will examine in detail the nonlinear dynamics in a single MRR in the presence of instantaneous and non-instantaneous nonlinearities. We will first perform a comparison between the EC model and the PC model in predicting instability in a nonlinear optical device with feedback, such as an MRR. We show that, for the case of non-instantaneous nonlinearity, the PC model also predicts an upper limit of the nonlinear relaxation time constant for SP to occur, but this value is higher (thus making the constraint less strict) than the value predicted by the EC model [21, 22]. By comparing the results of the two models, we provide an explanation why high-frequency instability such as period doubling and free carrier induced SP have not been observed in integrated optics, such as in a silicon MRR. We also provide clarification in section 2.2 on low extension ratio of SP effect in MRR provided by [73] for not observing of SP in MRR due to FCD is not accurate.

This chapter is organized as follows. In Section 2.1 we apply the EC and PC formalisms to study nonlinear dynamics of a single MRR with instantaneous Kerr nonlinearity. This system is characterized by the fact that the relaxation time of the nonlinearity is shorter

than the cavity roundtrip time. As a numerical example, we will consider an MRR made of chalcogenide glass, which has a large Kerr coefficient with ultrafast response time. In Section 2.2, we will investigate the nonlinear dynamics of a single MRR with non-instantaneous nonlinearity, which is characterized by a relaxation time that is longer than the cavity roundtrip time. An important device which exemplifies this system is a silicon MRR, in which the nonlinear effect is dominated by FCD. We will study the influence of the FC lifetime and FCA on the nonlinear dynamics of the device, with the aim of assessing the feasibility of achieving these behaviours in a practical device. In particular, we will show that high-order instability may provide a promising route to observing nonlinear dynamics in a silicon MRR, allowing these effects to be exploited for practical applications. We will conclude the chapter in Section 2.3 with a summary.

2.1 Nonlinear Dynamics in a Single MRR with Instantaneous Nonlinearity

Figure 2.1 shows a single MRR with radius R coupled to a straight waveguide with field coupling coefficient κ_1. The coupling strength can be adjusted by varying the dimensions of the microring and bus waveguides, as well as the gap separation between them [74]. We assume the microring waveguide is made of a high-index material with instantaneous nonlinearity, such as the Kerr effect in silicon or chalcogenide glass.

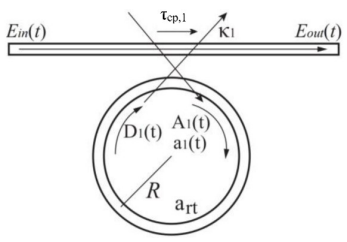

Figure 2.1, A Unidirectional Microring Resonator (MRR)

There are two main approaches to analyze the nonlinear dynamics of the MRR: the EC model and the PC model. In the EC model, we treat the MRR as a lumped RLC network which supports a single resonance mode. On the other hand, the PC model takes into account the distributed nature and the time delay of the traveling wave around the microring. In this case, the microring supports an infinite number of resonance modes. The differences in the resonance spectra of the power in an MRR obtained from the EC and PC model are shown in figure 2.2 for an MRR with roundtrip loss a_{rt} of 0.98, radius R of 100μm and coupling strength κ_1 of 0.4.

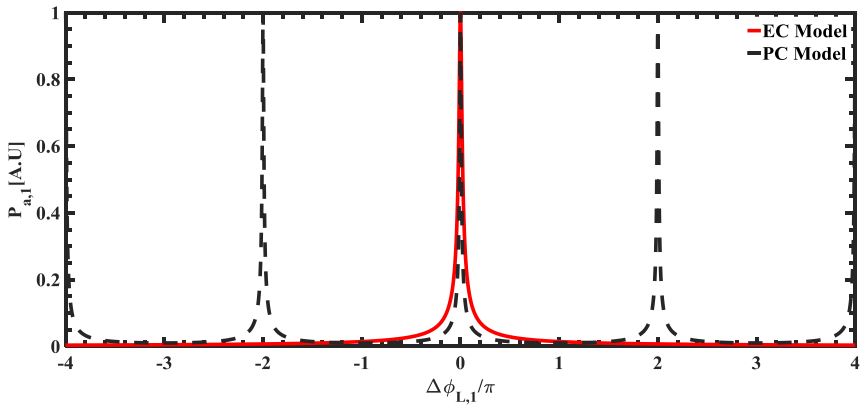

Figure 2.2, The stored power in the MRR vs linear phase detune

The figure shows the stored power $P_{a,1}$ in an MRR as a function of linear phase detune $\Delta\varphi_{L,1}$. The EC spectrum (shown by red solid line) has only one resonance mode and an infinitely wide FSR, while the PC spectrum (black dashed line) consists of an infinite comb of resonances equally spaced by a fixed FSR (assuming no waveguide dispersion). As a result, the EC model is valid for analysis involving only a narrow range of frequencies surrounding a resonance mode of interest, while the PC model has more general validity and can predict phenomena not accessible with the EC model. In this section, we will apply each method to analyze the nonlinear dynamics of an MRR with

instantaneous nonlinearity.

2.1.1 Energy-Time formalism of a Single Microring Resonator (EC model)

We consider the behavior of the MRR near a resonance frequency ω_1, which allows us to model the resonator by an RLC circuit [75]. We denote $\hat{a}_1(t)$ and $|\hat{a}_1(t)|^2$ as the wave amplitude and stored energy in the MRR, respectively. Instead of the field coupling coefficient κ_1, we define the energy coupling coefficient μ_1^2 as the rate of energy exchange between the bus waveguide and the resonator [74]. The energy coupling coefficient is related to the field coupling coefficient κ_1 as $\mu_1^2 = \frac{\kappa_1^2}{T_{rt}}$, where T_{rt} is the roundtrip time of the MRR [73]. The photon lifetime in the MRR, $\tau_{ph,1}$, is due to the energy loss through the coupling coefficient μ_1 and the intrinsic losses in the cavity (i.e., linear absorption and scattering loss):

$$\frac{1}{\tau_{ph,1}} = \alpha_0 v_g + \frac{\mu_1^2}{2} \tag{2.1}$$

In the above equation, α_0 is the linear loss coefficient and $v_g = C/n_g$ is the group velocity of light in the microring waveguide (C is the speed of light in free space and n_g is the group index). The rate of energy change in the MRR can be described in the time domain by [74],

$$\frac{d\hat{a}_1(t)}{dt} = \left(j\omega_1 - \frac{1}{\tau_{ph,1}} \right) \hat{a}_1(t) - j\mu_1 \sqrt{\hat{P}_{in}(t)}, \tag{2.2}$$

where $\hat{P}_{in}(t)$ and ω_1 are the square of input optical field applied to the bus waveguide and

resonance frequency of micoring resonator, respectively. Writing $\hat{a}_1(t)$ in terms of the slowly varying envelop $a_1(t)$ and a fast oscillating wave at frequency ω, $\hat{a}_1(t) = a_1(t)e^{-j\omega t}$, we substitute into equation (2.2) to get

$$\frac{da_1(t)}{dt} = \left(j\Delta\omega_1 - \frac{1}{\tau_{ph,1}} \right) a_1(t) - j\mu_1 \sqrt{P_{in}(t)}, \tag{2.3}$$

where $\Delta\omega_1 = \omega_1 - \omega$ and $P_{in}(t)$ are the frequency detuning from the resonance and input optical power, respectively . Equation (2.3) describes the linear dynamics of the slowly varying signal envelope $a_1(t)$.

We can introduce nonlinearity into the equation by including the resonance frequency shift caused by the Kerr effect. When the microring waveguide possesses instantaneous Kerr nonlinearity with Kerr coefficient n_2, the refractive index of the ring waveguide depends on the intensity of the optical field as $n(t) = n_0 + \Delta n_{NL}$, where n_0 is the linear effective index of the waveguide and $\Delta n_{NL} = n_2 |a_1(t)|^2 / A_{eff} T_{rt}$ is the nonlinear index change due to the Kerr effect. In the expression for Δn_{NL}, A_{eff} is the effective mode area of the waveguide and $T_{rt}=2\pi R/v_g$ is the roundtrip delay time. The term $|a_1(t)|^2/T_{rt}$ represents the power flowing through a cross-section of the microring waveguide. The nonlinear index change causes a resonant frequency shift of the MRR given by $\delta\omega_{NL} = -\omega_1 \Delta n_{NL}/n_g$. Including this nonlinear frequency shift in equation (2.3), we obtain the equation describing the nonlinear dynamics of the MRR as [74]

$$\frac{da_1(t)}{dt} = \left(j\left[\Delta\omega_1 - \omega_1 \gamma_{Kerr} |a_1(t)|^2\right] - \frac{1}{\tau_{ph,1}} \right) a_1(t) - j\mu_1 \sqrt{P_{in}(t)}, \tag{2.4}$$

where we have defined the instantaneous nonlinear coefficient γ_{Kerr} as $\gamma_{Kerr} = n_2(n_g A_{eff} T_{rt})^-$

[1]. To study the stability of the nonlinear MRR, we first find the stationary solution $a_{f,1}$ of the above equation by setting $\frac{da_{f,1}(t)}{dt} = 0$ and solving for $a_{f,1}$ to get

$$\left|a_{f,1}\right|^2 = \frac{\mu_1^2 P_{in}}{\left(\Delta\omega_1 - \omega_1\gamma_{Kerr}\left|a_{f,1}\right|^2\right)^2 + \frac{1}{\tau_{ph,1}^2}}. \qquad (2.5)$$

Next we apply a small perturbation $\varepsilon_{a,1}(t)$ to the stationary state to get $a_1(t) = a_{f,1} + \varepsilon_{a,1}(t)$. By substituting this perturbative solution into equation (2.4) and keeping only terms of first order in $\varepsilon_{a,1}$, we obtain the following characteristic equation:

$$\frac{d^2\varepsilon_{a,1}(t)}{dt^2} + \frac{2}{\tau_{ph,1}}\frac{d\varepsilon_{a,1}(t)}{dt} + \left(\left(\Delta\omega_1 - 2\gamma_{Kerr}\omega_1\left|a_{f,1}\right|^2\right)^2 + \frac{1}{\tau_{ph,1}^2} - \left(\gamma_{Kerr}\omega_1\left|a_{f,1}\right|^2\right)^2\right)\varepsilon_{a,1}(t) = 0 \qquad (2.6)$$

The roots of the above equation in the Laplace domain are the eigenvalues s_1 and s_2 which determine the dynamic behavior of the energy in the MRR:

$$s_{1,2} = -\frac{1}{\tau_{ph,1}} \pm j\sqrt{\left(-\Delta\omega_1 + \gamma_{Kerr}\omega_1\left|a_{f,1}\right|^2\right)\left(-\Delta\omega_1 + 3\gamma_{Kerr}\omega_1\left|a_{f,1}\right|^2\right)} \qquad (2.7)$$

In particular, the stationary point is stable if the real parts of both eigenvalues are negative. On the other hand, if one of the eigenvalues lies in the right-hand side of the s-plane, the energy in the MRR exhibits unstable behavior. In this case, if the eigenvalue is real, the energy has two bistable values. If the eigenvalue is complex, the MRR exhibits self-pulsation at a frequency determined by the imaginary part of the eigenvalue [21].

From equation (2.7) we find that the eigenvalues are complex but their real parts (given by $-1/\tau_{ph,1}$) are always negative if the frequency detune $\Delta\omega_1$ is outside the range $-3\gamma_{Kerr}\omega_1|a_{f,1}|^2 < \Delta\omega_1 < -\gamma_{Kerr}\omega_1|a_{f,1}|^2$. Thus, the system is always stable outside this

frequency range and never experiences instability. On the other hand, within this frequency range, the eigenvalues are real and one of them is positive, so that the MRR exhibits bistable behavior. Thus, according to the EC model, SP never occurs in an MRR with instantaneous Kerr nonlinearity.

2.1.2 Power-Space formalism of a Single MRR (PC method)

We consider again the MRR device in figure 2.1. We denote the field amplitude of the optical wave propagating in the microring waveguide as $A_1(t)$ and its power by $|A_1(t)|^2$. The power coupling coefficient κ_1^2 expresses the fraction of power coupled between the bus waveguide and the resonator waveguide. Referring to figure 2.1, we can relate the fields $A_1(t)$ and $D_1(t)$ in the MRR to the input and output fields $E_{in}(t)$ and $E_{out}(t)$ via the universal coupling matrix [61],

$$\begin{bmatrix} E_{out}(t) \\ A_1(t) \end{bmatrix} = \begin{bmatrix} \tau_{cp,1} & -j\kappa_1 \\ j\kappa_1^* & \tau_{cp,1}^* \end{bmatrix} \begin{bmatrix} E_{in}(t) \\ D_1(t) \end{bmatrix}. \tag{2.8}$$

For a lossless coupling junction, the field coupling coefficient κ_1 and transmission coefficient $\tau_{cp,1}$ satisfy the power conservation law [61],

$$\left|\tau_{cp,1}\right|^2 + \left|\kappa_1\right|^2 = 1 \tag{2.9}$$

The j factor in the matrix equation (2.8) expresses the fact that the coupled fields experience a $\pi/2$ phase shift. Also, one of the main assumptions of the universal coupling model is that the coupling junction doesn't have a physical length. Thus, there is no phase shift in the transmitted fields, and both the transmission and coupling coefficients are real constants [76].

Using the fact that the field $D_1(t)$ is a delayed version of the field $A_1(t)$ by exactly one roundtrip, we obtain the following relation between $A_1(t)$ and the input field $E_{in}(t)$:

$$A_1(t+T_{rt}) = \gamma e^{-j\Delta\varphi_{L,1}} A_1(t) - j\kappa_1 E_{in}(t+T_{rt}) \tag{2.10}$$

where a_{rt} is the amplitude attenuation per roundtrip, $\Delta\varphi_{L,1} = 2\pi RK_0$ is the linear roundtrip phase detune, K_0 is the wave number of the field inside the waveguide and $\gamma = a_{rt}\tau_{cp,1}$. Equation (2.10) describes the time evolution of the field as it circulates around the MRR.

For an MRR with Kerr nonlinearity, the nonlinear index change $\Delta n_{NL}(t)$ adds an intensity-dependent contribution to the roundtrip phase given by $\varphi_{NL,1}(t) = \xi_{Kerr}|A_1(t)|^2$, where the nonlinear phase coefficient is $\xi_{kerr} = K_0 v_g T_{rt} n_2 / A_{eff}$. Including this nonlinear phase in equation (2.10), we get

$$A_1(t+T_{rt}) = \gamma A_1(t) e^{-j(\Delta\varphi_{L,1}+\varphi_{NL,1}(t))} - j\kappa_1 E_{in}(t+T_{rt}). \tag{2.11}$$

The above equation describes how the field in the nonlinear MRR is updated after each roundtrip. It is called the iterated map of the nonlinear dynamic system.

To determine the stationary solution (or fixed point) of the iterated map, we set $A_1(t+T_{rt}) = A_1(t) = A_{f,1}$ in equation (2.11) and solve for $A_{f,1}$ to get

$$A_{f,1} = \frac{-j\kappa_1 E_{in}}{1-\gamma e^{-j\varphi_{f,1}}}, \tag{2.12}$$

where $\varphi_{f,1}$ is the total phase detune of the stationary state, $\varphi_{f,1} = \Delta\varphi_{L,1} + \xi_{Kerr}|A_{f,1}|^2$. To determine the stability of the stationary solution, we add a small perturbation $\varepsilon_{A,1}(t)$ to the field amplitude, $A_1(t) = A_{f,1} + \varepsilon_{A,1}(t)$, and substitute it into equation (2.11). By linearizing the exponential term and keeping only terms of first order in $\varepsilon_{A,1}$, we obtain

$$\varepsilon_{A,1}(t+T_{rt}) = \gamma e^{-j\varphi_{f,1}} \left[\left(1 - j\xi_{Kerr}\left|A_{f,1}\right|^2\right)\varepsilon_{A,1}(t) - j\xi_{Kerr} A_{f,1}^2 \varepsilon_{A,1}^*(t) \right] \tag{2.13}$$

The above equation with its complex conjugate part forms a dynamic system such as $\boldsymbol{\varepsilon}_{\mathbf{A,1}}(t+T_{rt})=J\boldsymbol{\varepsilon}_{\mathbf{A,1}}(t)$. The vector of $\boldsymbol{\varepsilon}_{\mathbf{A,1}}(t)$ consist of $\varepsilon_{A,1}(t)$ and C.C of $\varepsilon_{A,1}(t)$. The eigenvalues of J determine the nonlinear dynamics of the field inside the MRR:

$$z_{1,2}=x_0\pm\sqrt{x_0^2-\gamma^2};x_0=\gamma\,\mathrm{Re}\left(\left(1-j\xi_{\mathrm{ker}r}\left|A_{f,1}\right|^2\right)e^{-j\varphi_{f,1}}\right) \tag{2.14}$$

The stationary solution is stable if the magnitudes of both eigenvalues are less than 1. If the magnitude of either eigenvalue exceeds 1, the following instabilities can occur [77]:

I. If one of the eigenvalues is real and greater than 1, the field inside the MRR exhibits BS behavior.

II. If one of the eigenvalues is real and less than -1, Ikeda instability occurs. This type of instability is also known as period doubling and corresponds to an oscillatory solution around the stationary state with a period of twice the roundtrip delay time T_{rt}.

III. If the eigenvalues are complex with magnitude greater than 1, SP occurs with the period of oscillation given by $2\pi T_{rt}/\Phi$, where Φ is the phase angle of the eigenvalue.

Equation (2.14) suggests that the optical field has bistable solutions if $1+\gamma^2 > 2x_0$ and exhibits Ikeda instability if $1+\gamma^2 < -2x_0$.

Ikeda and SP instabilities can be considered as being caused by a spontaneous breaking of time symmetry due to nonlinearity. We can explain Ikeda instability in terms of spontaneous four-wave mixing of two adjacent modes of the MRR [78]. When an input signal E_q with frequency ω_q is tuned to approximately half way between two resonant modes ω_n and ω_m, at high enough intensity, two new frequency components E_n and E_m are spontaneously generated at the resonant frequencies ω_n and ω_m. These two frequency components beat with each other to form modulations in the cavity field with period

equal to $2T_{rt}$. On the other hand, SP is caused by energy exchange and beating between two linear coupled modes [36]. Thus, SP does not occur in first order systems such as a single MRR with instantaneous nonlinearity.

2.1.3 Numerical Results

In this section, we present numerical results obtained from the EC and PC stability analyses to compare the nonlinear dynamic behaviors predicted by the two models. We choose the example of an MRR made of chalcogenide glass (As_2Se_3), since this material has a large Kerr nonlinear coefficient ($n_2 = 11\times10^{-14}$ cm^2/W) with ultrafast response time and negligible two-photon absorption in the telecommunication window (L and C bands) [79]. The waveguide structure is a channel waveguide with As_2Se_3 as the core material (index = 2.743) with a height of 320nm and a width of 500nm. The waveguide lies on a SiO_2 substrate (index = 1.46) with air cladding (index = 1). We performed a full vectorial modal analysis on the waveguide to find the effective index, group index and effective area of the fundamental TE mode [80]. The optical field distribution of the fundamental transverse electric (TE_0) mode is shown in figure 2.3. At the 1.55 μm wavelength, the effective index n_{eff} and group index n_g of the waveguide are 2.37 and 3.36, respectively. The effective mode area is $A_{eff} = 0.1328\mu m^2$. Because the field distribution is symmetric regarding x direction, we only demonstrated half of the waveguide in this direction.

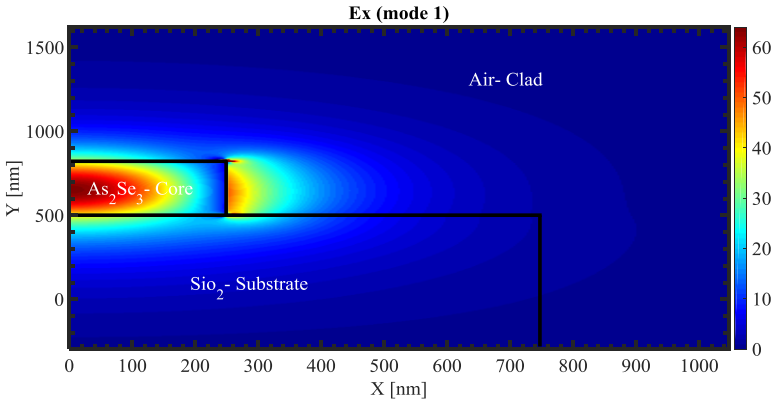

Figure 2.3, Optical Field distribution in the cross-section of Chalcogenide waveguide for fundamental TE_0 mode (Ex)

We choose the radius of the MRR to be R = 100μm and power coupling coefficient κ_1 = 0.4. The roundtrip amplitude attenuation factor is assumed to be a_{rt} = 0.98. We performed stability analysis of the MRR using both the EC and PC models. Figure 2.4(a) and (b) show the stability phase map plots of the device obtained from the two models. The stability phase map shows the regions of stable response (blue), bistable response (yellow) and Ikeda oscillations (brown) as functions of the linear phase detune ($\Delta\varphi_{L,1}$) and the power in the MRR (the stored power $P_{a,1}$). From the stored power in the microring, we calculated the input power P_{in} using equations (2.5) and (2.12) for the EC and PC models, respectively. These values are shown on the contour lines in the figures.

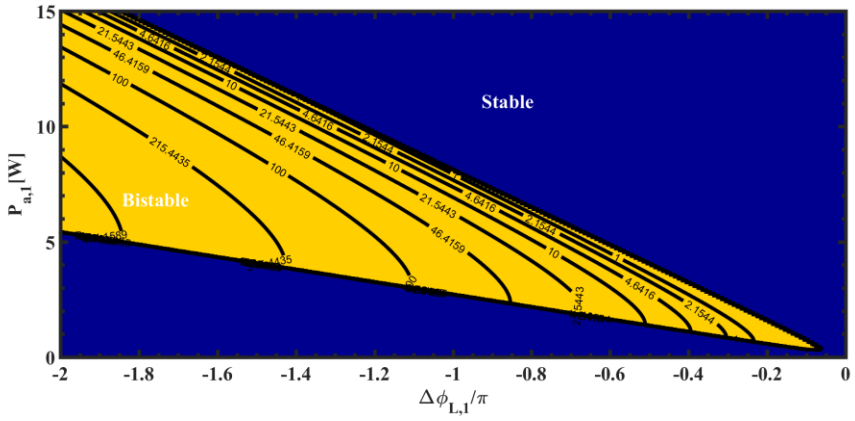

(a)

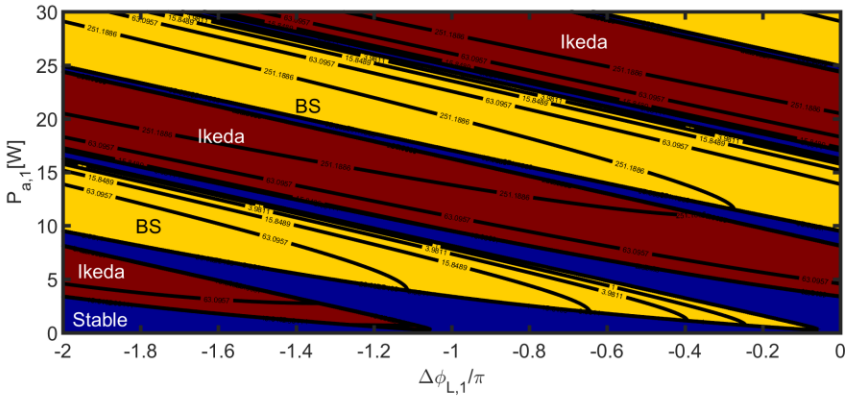

(b)

Figure 2.4, Phase map of stored power inside a single MRR vs linear phase detune for (a) EC model (b) PC model.

The stability phase maps obtained from the EC and PC models have three significant differences. The first and most significant difference is that the EC model predicts only bistable behavior. It fails to predict Ikeda instability. As explained in the previous sections, the EC model accounts for only a single resonance mode so that Ikeda instability, which relies on adjacent resonance modes being generated and beating with each other, cannot occur within the EC formalism. The second difference is that the PC stability map is periodic with respect to the linear phase detune so that multiple BI and Ikeda instability regions can exist for a fixed stored power. Finally, the EC model is not valid for frequencies far from the resonance or at high powers, which explains the discrepancy in the first bistable region predicted by the EC and PC models. These results show that the EC model is not suitable for analyzing the nonlinear dynamic behavior of MRRs at large linear phase detunes or high input powers.

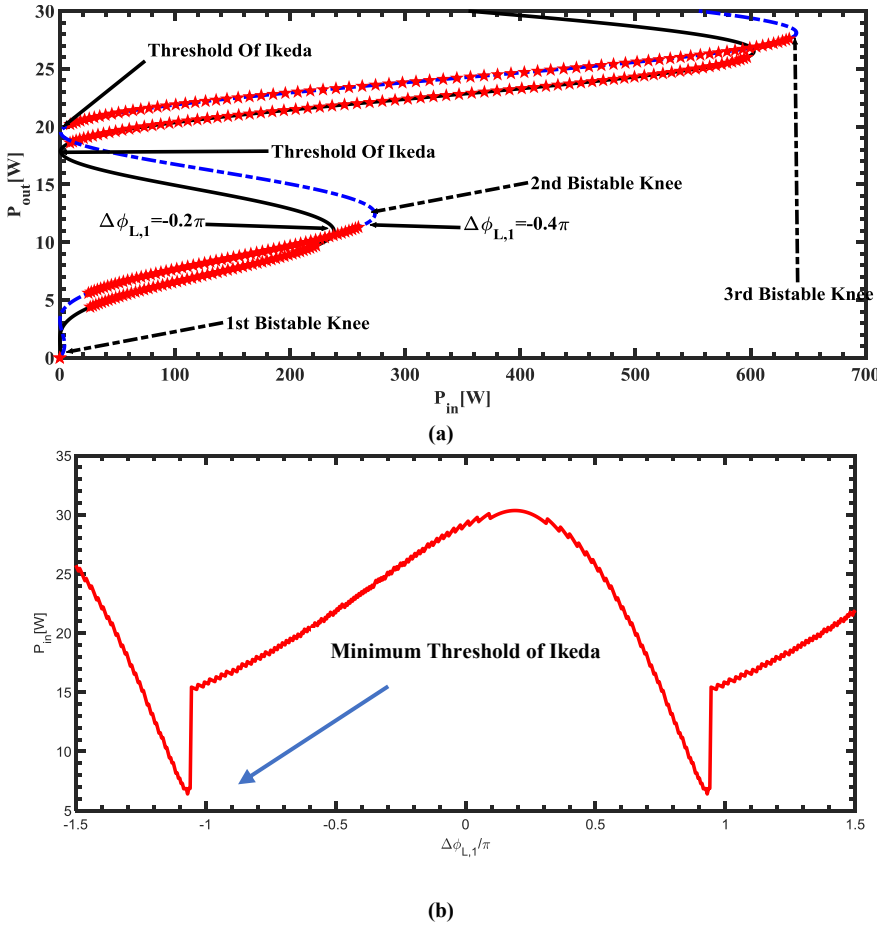

Figure 2.5, The stored power inside the MRR as a function of input power for linear phase detunes -0.2π (black solid line) and -0.4π (blue dashed line). (b) Plot of threshold power of Ikeda instability vs. linear phase detune.

To be able to achieve in practice the various nonlinear dynamic behaviors predicted in the stability map, the powers required to reach these behaviors must be within the practical limits that an integrated photonic MRR can handle. To examine this issue more closely, we plot in figure 2.5(a) the stored power in the MRR (i.e., the stationary solutions $|A_{f,1}|^2$) as a function of the input power for two different phase detune values, $\Delta\varphi_{L,1}$ = -0.2π (black solid line) and $\Delta\varphi_{L,1}$ = -0.4π (blue dashed line). The stationary solutions corresponding to Ikeda instability are shown by the stars. The plot shows that for a given input power, the stored power in the MRR can take on multiple values, with some of these values corresponding to stable solutions while others to bistable solutions or Ikeda

oscillations. The device is said to exhibit multi-stability. The plot also shows that to reach the first Ikeda region, the input power must be increased past the first "bistability knee" as indicated in the plot. Similarly, to reach the second Ikeda region, the input power must be increased past the second "bistability knee", and so on. The first "bistability knee" corresponds to an input power of 270 mW, while the second "bistability knee" corresponds to an input power of around 230 W (for $\Delta\varphi_{L,1} = -0.2\pi$). The threshold of 270 mW indicates that system enters the Bistable region of operation at relatively small power.

These optical powers are simply too large for integrated photonic devices to handle. For this reason, Ikeda instability has not been observed in an integrated optical resonator.

Comparison of the stability curves for $\Delta\varphi_{L,1} = -0.2\pi$ (solid line) and $\Delta\varphi_{L,1} = -0.4\pi$ (dashed line) shows that the powers required to reach the "bistability knees" highly depend on the linear phase detune. In general, increasing the linear phase detune from the resonance decreases the amount of optical power stored in the MRR. So, to achieve the same nonlinear effect, we must pump more power into the MRR. Thus we expect the threshold power for reaching bistability to increase with increasing linear phase detune. This trend is also observed in the phase maps in figure 2.4.

In figure 2.5(b) we plot the threshold input power required to reach Ikeda instability as a function of the linear phase detune. From the plot we find that we can reach Ikeda instability with a minimum input power of 6W. The stationary solution corresponding to this threshold value lies on the Ikeda instability branch above the second "bistability knee", as indicated in figure 2.5(a). Thus, in order to reach this Ikeda threshold, we must first increase the input power above 230 W past the second "bistability knee", which as

explained above is not practical. In Section 2.2.3, we will propose two alternative routes to reach higher-order instability without requiring prohibitively high input CW optical power. The plot in figure 2.5(b) also indicates that the minimum threshold power for reaching Ikeda instability occurs at linear phase detunes close to $\pm\pi$. For cavity phase detunes near π, the two adjacent modes of the cavity have the highest probability of being spontaneously generated through FWM to form period-doubling oscillations [78].

To verify the results of the stability analysis based on equations (2.7) and (2.13), we performed steady-state analysis of the MRR for a fixed linear phase detune using both the EC and PC formalisms. Figure 2.6 shows the stored power in the microring ($P_{a,1}$) as a function of the input power (P_{in}) for a fixed linear phase detune $\Delta\varphi_{L,1} = -0.2\pi$. The time-domain simulation results are in good agreement with the stability curve in figure 2.5 (for linear phase detune $\Delta\varphi_{L,1} = -0.2\pi$). Both the EC and PC simulations predict bistable behavior for the range of input powers from 72mW to about 725 mW. Beyond this range the device is in the stable regime again, until the input power exceeds 27W, at which point the PC model predicts the emergence of Ikeda instability. For input powers above 30 W, the field becomes chaotic.

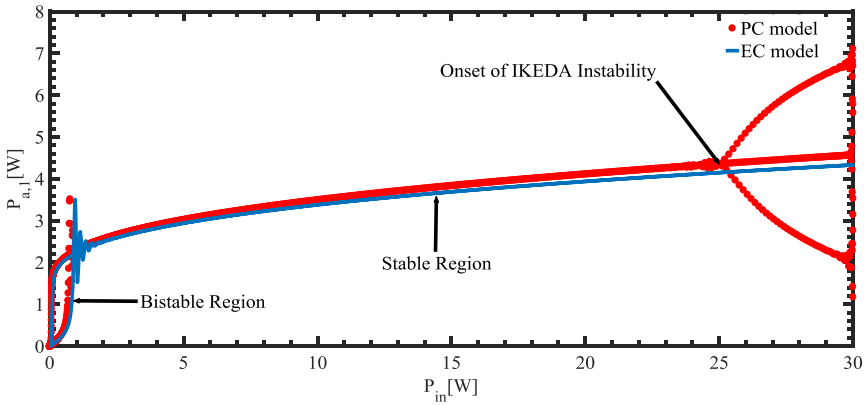

Figure 2.6, The stored optical power $P_{a,1}$ versus input power Pin for single MRR with linear phase detune -0.2π

As shown in figure 2.6, the field inside the MRR takes multiple values in the Ikeda instability region ($P_{in} > 27$ W). To verify that this corresponds to oscillation behavior, we performed time domain simulation of the device by solving equation (2.11) numerically using the finite difference method. In this approach, we discretized the circumference of the MRR into N_z equal arcs of length $\Delta z = 2\pi R/N_z$. The linear phase delay, nonlinear phase shift coefficient and linear loss in each arc are given by $\Delta\varphi_{L,1}/N_z$, ξ_{kerr}/N_z, and $\sqrt[N_z]{a_{rt}}$, respectively. With these modifications, the propagation of an optical signal in the MRR is calculated from the recursive equation

$$A_{n_z+1}^{n_t} = A_{n_z}^{n_t} \sqrt[N_z]{a_{rt}}\, e^{-j\left(\frac{\Delta\varphi_{L,1}+\xi_{Kerr}\left|A_{n_z}^{n_t}\right|^2}{Nz}\right)} \tag{2.15}$$

In the above equation, n_t and n_z are the index of the discrete time and arc segment, respectively. At the end of each roundtrip, $n_z = N_z$, we apply the boundary condition at the coupling junction,

$$A_1^{n_t} = -j\kappa_1 E_{in} + \tau_{cp,1} A_{N_z}^{n_t} \tag{2.16}$$

Figure 2.7(a) and (b) show the simulation results for input power $P_{in} = 15$ W and $P_{in} = 27$ W, respectively. The linear phase detune is $\Delta\varphi_{L,1} = -0.2\pi$ for both simulations. For $P_{in} = 15$ W, the power in the MRR is stable, which is also predicted by the PC stability curve in figure 2.6. However, for $P_{in} = 27$ W, the power in the MRR oscillates between two extremum values of 3 W and 5.8 W, with an oscillation period exactly equal to two roundtrips, as shown by the inset of figure 2.7(b). This period-doubling oscillation is predicted by the PC stability curve in figure 2.6.

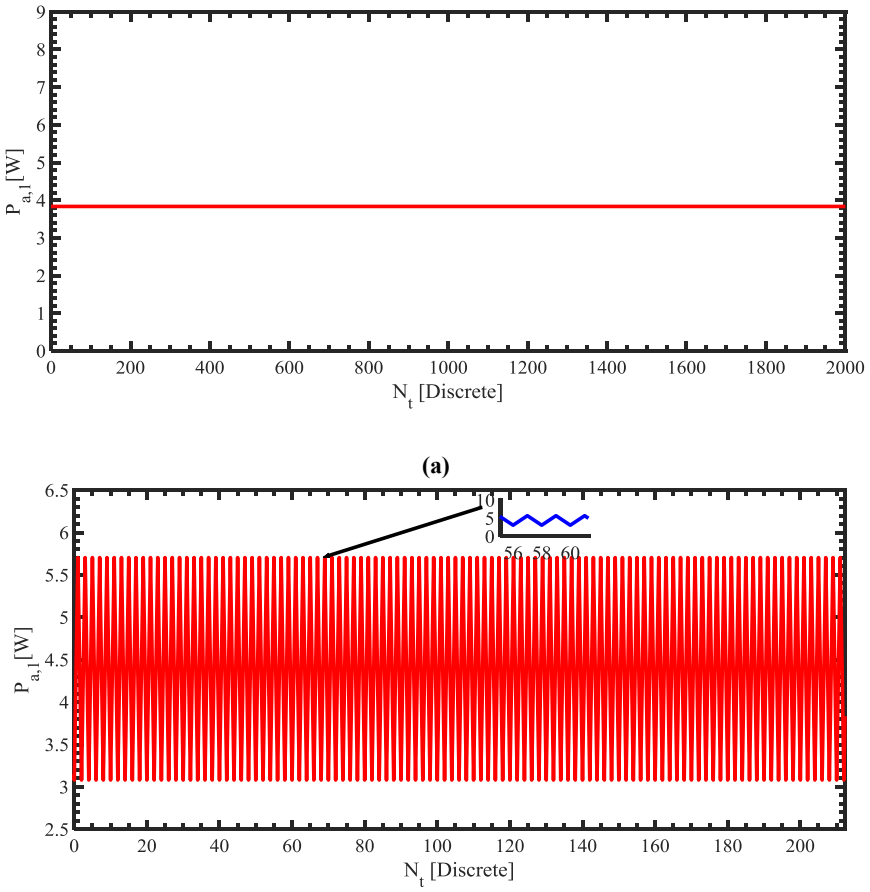

Figure 2.7, The stored power inside the microring Pa1 versus round trip indices for a single MRR with linear phase detune -0.2π (a) P_{in}=15W, (b) Pin=27W

A power of 27 W for observing of Ikeda instability is too high for an integrated photonic device as the chip would be damaged by the laser.

The laser damage threshold highly depends on the waveguide dimensions (W and H) and Laser operation mode (CW or pulse). For a Chalcogenide fiber with conventional diameter of 10 µm, it can handle optical power in the range of 5W [79].

It is possible to reduce this power, for example, by designing the waveguide to have stronger mode confinement so that the nonlinear interaction between photons is enhanced per roundtrip. Also, by using an MRR with a larger radius, it may also be possible to

reduce the threshold power due to the increased roundtrip interaction length as well as increased effective nonlinear coefficient ζ_{Kerr}. This is verified by the simulation results in figure 2.8, which shows the dependence of the threshold of Ikeda instability on the microring radius R. The propagation loss is set to a fixed value of 0.087 dB/100μm (corresponding to a roundtrip amplitude attenuation of 0.98 in an MRR with 100μm radius). Although the threshold power can be substantially reduced as R is increased, it is still not possible to reduce the required power for observing Ikeda oscillations in a single MRR with instantaneous Kerr nonlinearity to a level that can be tolerated by integrated optics devices (e.g., less than a few hundred watts).

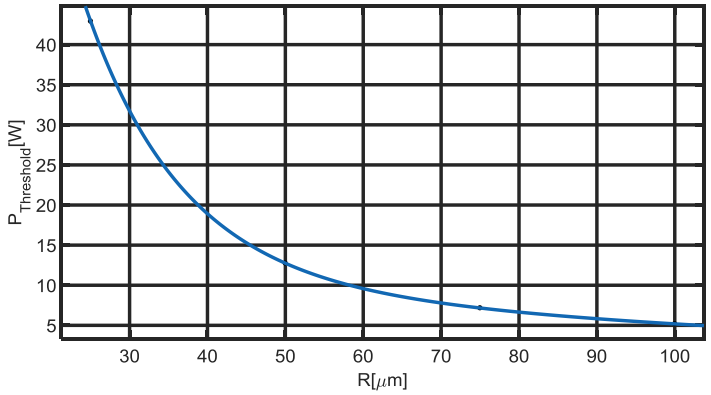

Figure 2.8, Dependence of the threshold power of Ikeda instability on the MRR radius

Although for the smaller radius MRR, we need more power to show Ikeda instability but this mechanism is promising for generation of the THZ periodic signal. For example, by the state of art design of MRR with radius of 1 μm and round-trip delay of 83 fs, one can generate optical signal with oscillation frequency of 10 THz. The oscillation frequency highly depends on the radius of MRR and we can generate arbitrary frequency components by varying the radius of MRR.

2.2 Nonlinear Dynamics in a Single MRR with Non-Instantaneous Nonlinearity

In the previous section, we showed that a single MRR with instantaneous Kerr nonlinearity can only exhibit oscillations of the Ikeda type, and the threshold power to achieve this instability is too large for integrated photonic devices. The challenge with this type of devices is that the Kerr effect in most dielectric optical materials is very weak. On the other hand, in a semiconductor such as silicon operating at the telecommunication wavelengths, significant two-photon absorption takes place which generates a large free carrier density. These free carriers in turn give rise to optical nonlinearity through the free carrier dispersion and absorption effects. Depending on the input power level and free carrier lifetime, free carrier induced nonlinearity could be two orders of magnitude larger than the Kerr effect. This strong FC induced optical nonlinearity can potentially be exploited to achieve optical instabilities in an MRR at low powers. On the other hand, the time response of the nonlinear medium is limited by the FC lifetime and the free carriers also cause excess loss due to FCA. These effects have a strong influence on the nonlinear dynamics of the device. In this section, we will study the nonlinear dynamics of an MRR with non-instantaneous nonlinearity. The material chosen for the device is silicon, which is widely used in integrated optics [73]. We will perform stability analysis of a silicon MRR in the presence of FCD and FCA using both the EC and PC models and compare their results.

2.2.1 Energy-Time formalism of a Single MRR (EC method)

We can modify the EC description of a single nonlinear MRR (equation (2.4)) to include

nonlinearity caused by FCs generated by TPA in the resonator. This is accomplished by including a resonant frequency shift due to the nonlinear index change in the MRR caused by the FCs. Let $N_1(t)$ be the time-dependent FC density generated in the microring, the nonlinear index change due to FCD is $\Delta n_{NL} = \sigma_{FCD} N_1(t)$, where σ_{FCD} is the free carrier dispersion volume. Since the resonant frequency shift due to FCD is given by $\delta\omega_{NL} = -\omega_1 \Delta n_{NL}/n_g$, we can modify equation (2.4) describing the time evolution of the energy in the MRR as follows [14]:

$$\frac{da_1(t)}{dt} = \left(j\left(\Delta\omega_1 - \frac{\omega_1}{n_g}\sigma_{FCD} N_1(t) \right) - \frac{1}{\tau_{ph,1}} \right) a_1(t) - j\mu_1 \sqrt{P_{in}(t)} \qquad (2.17.a)$$

The generation of the FC density in the MRR by TPA can be modeled by the rate equation

$$\frac{dN_1(t)}{dt} = \frac{\beta_{TPA}}{2\hbar\omega_1} \left(\frac{|a_1(t)|^2}{A_{eff} T_{rt}} \right)^2 - \frac{N_1(t)}{\tau_{fc}} \qquad (2.17.b)$$

where β_{TPA} is the TPA coefficient [$m.W^{-1}$], $\hbar\omega_1$ is the photon energy and τ_{fc} is the FC lifetime due to various recombination processes. Note that in equation (2.17.a) we have neglected the resonant frequency shift due to Kerr effect because it is much smaller than the FCD-induced shift in a silicon MRR at moderate input optical powers. In addition, we have also neglected loss in the resonator due to FCA.

To determine the behaviour of the MRR at a stationary state, we perform stability analysis around the stationary solutions ($a_{f,1}$, $N_{f,1}$) by adding small perturbations: $a_1(t) = a_{f,1} + \varepsilon_{a,1}(t)$ and $N_1(t) = N_{f,1} + \varepsilon_{n,1}(t)$. The fixed points of equation 2.17, P_{in} and $N_{f,1}$, are as

follows:

$$\sqrt{P_{in}} = \frac{\left(\left(\Delta\omega_l - \frac{\omega_l}{n_g}\sigma_{FCD}N_{f,l}\right) + \frac{j}{\tau_{ph,l}}\right)a_{f,l}}{\mu_l} \tag{2.18.a}$$

$$N_{f,l} = \frac{\beta_{TPA}}{2\hbar\omega_l}\left(\frac{\left|a_{f,l}\right|^2}{A_{eff}T_{rt}}\right)^2\tau_{fc} \tag{2.18.b}$$

The above coupled equations suggest that finding P_{in} and $N_{f,l}$ from a given value of $a_{f,l}$ is much easier than solving for a fixed value of $a_{f,l}$ from a given P_{in}. Substituting the perturbed solutions into equations (2.17) and keeping only the first-order perturbation terms, we obtain the following characteristic equations:

$$\frac{d\varepsilon_{a,l}(t)}{dt} = \left(j\Delta\omega_{NL,l} - \frac{1}{\tau_{ph,l}}\right)\varepsilon_{a,l}(t) - j\frac{\omega_l}{n_{eff}}\sigma_{FCD}a_{f,l}\varepsilon_{n,l}(t) \tag{2.19.a}$$

$$\frac{d\varepsilon_{n,l}(t)}{dt} = \frac{\beta_{TPA}}{\hbar\omega_l}\left(\frac{\left|a_{f,l}\right|}{A_{eff}T_{rt}}\right)^2\left(a^*_{f,l}\varepsilon_{a,l}(t) + a_{f,l}\varepsilon^*_{a,l}(t)\right) - \frac{\varepsilon_{n,l}(t)}{\tau_{fc}} \tag{2.19.b}$$

$$\Delta\omega_{NL,l} = \Delta\omega_l - \frac{\beta_{TPA}}{2\hbar\omega_l}\frac{\omega_l}{n_g}\sigma_{FCD}\tau_{fc}\frac{\left|a_{f,l}\right|^4}{\left(A_{eff}T_{rt}\right)^2} \tag{2.19.c}$$

Equation (2.19.a), its complex conjugate, and equation (2.19.b) form a dynamic system, $d\varepsilon/dt = J\varepsilon$, where $\boldsymbol{\varepsilon} = [\varepsilon_{a,l}(t), \varepsilon^*_{a,l}(t), \varepsilon_{n,l}(t)]^T$ and the Jacobian matrix **J** is given by

$$\mathbf{J}=\begin{bmatrix} j\Delta\omega_{NL,1}-\dfrac{1}{\tau_{ph,1}} & 0 & -j\dfrac{\omega_1}{n_g}\sigma_{FCD}a_{f,1} \\ 0 & -j\Delta\omega_{NL,1}-\dfrac{1}{\tau_{ph,1}} & j\dfrac{\omega_1}{n_g}\sigma_{FCD}a_{f,1}^{*} \\ \dfrac{2\beta_{TPA}}{2\hbar\omega_1}\dfrac{|a_{f,1}|^2}{(A_{eff}T_{rt})^2}a_{f,1}^{*} & \dfrac{2\beta_{TPA}}{2\hbar\omega_1}\dfrac{|a_{f,1}|^2}{(A_{eff}T_{rt})^2}a_{f,1} & -\dfrac{1}{\tau_{fc}} \end{bmatrix} \tag{2.20}$$

We can determine the stability of the MRR dynamic system by applying the Ruth-Hurwitz stability criterion to the eigenvalues of the Jacobian matrix [77]. The eigenvalues are given by the roots of the cubic polynomial which are determined by solving |J-sI|=0, as follows,

$$\begin{aligned} &s^3+\left(\frac{1}{\tau_{fc}}+\frac{2}{\tau_{ph,1}}\right)s^2+\left(\Delta\omega_{NL,1}^2+\frac{1}{\tau_{ph,1}^2}+\frac{2}{\tau_{fc}\tau_{ph,1}}\right)s \\ &\ldots+\left(\frac{1}{\tau_{fc}}\left(\Delta\omega_{NL,1}^2+\frac{1}{\tau_{ph,1}^2}\right)+4\frac{\beta_{TPA}}{2\hbar\omega_1}\frac{|a_{f,1}|^4}{(A_{eff}T_{rt})^2}\omega_1\frac{\sigma_{FCD}}{n_g}\Delta\omega_{NL,1}\right)=0 \end{aligned} \tag{2.21}$$

If none of the eigenvalues have a positive real part, the system is stable; otherwise it is unstable. For the unstable case, the energy inside the MRR exhibits bistable behavior if the eigenvalues are real and SP if the eigenvalues are complex (nonzero imaginary parts). According to the Ruth-Hurwitz stability criterion, we can determine the stability behavior of the system based on the coefficients of the characteristic polynomial equation (2.21). Since all the coefficients of the polynomial except for the zeroth-order term are always positive, the zeroth-order term alone will determine the stability of the system. For unstable solutions, the zeroth-order term defines the nature of the instability, such as bistable or SP. Specifically, for bistable behavior, the following condition must be

satisfied:

$$\left(\frac{1}{\tau_{fc}}\left(\Delta\omega_{NL,1}^2+\frac{1}{\tau_{ph,1}^2}\right)+\frac{2\beta_{TPA}}{\hbar\omega_1}\left(\frac{\left|a_{f,1}\right|^2}{A_{eff}T_{rt}}\right)^2\omega_1\frac{\sigma_{FCD}}{n_g}\Delta\omega_{NL,1}\right)\le 0 \tag{2.22}$$

The above inequality shows that the condition for bistability to occur depends on the intensity of the stored energy inside the MRR and the linear phase detune. It is also worth mentioning that bistable behavior is nearly independent of the FC lifetime because of $1/\tau_{fc}$ and $\Delta\omega_{NL,1}$ terms in equation 2.22.

On the other hand, the condition for SP to occur is more complicated and the FC lifetime plays a significant role in this phenomenon. The following requirement should be satisfied to have SP behavior in a single MRR with non-instantaneous nonlinearity:

$$\begin{aligned}&\left(\Delta\omega_{NL,1}^2+\frac{1}{\tau_{ph,1}^2}+\frac{2}{\tau_{fc}\tau_{ph,1}}\right)-\\&\left(\left(\Delta\omega_{NL,1}^2+\frac{1}{\tau_{ph,1}^2}\right)+4\frac{\tau_{fc}\beta_{TPA}}{2\hbar\omega_1}\left(\frac{\left|a_{f,1}\right|^2}{A_{eff}T_{rt}}\right)^2\omega_1\frac{\sigma_{FCD}}{n_g}\Delta\omega_{NL,1}\right)\le 0\end{aligned} \tag{2.23}$$

We can determine the threshold energy inside the MRR and the critical FC lifetime for SP to occur by enforcing the equality condition in equation (2.22):

$$\begin{aligned}&\left(\frac{2}{\tau_{ph,1}}+\frac{1}{\tau_{fc}}\right)\left(\Delta\omega_{NL,1}^2+\frac{1}{\tau_{ph,1}^2}+\frac{2}{\tau_{fc}\tau_{ph,1}}\right)-\\&\left(\frac{1}{\tau_{fc}}\left(\Delta\omega_{NL,1}^2+\frac{1}{\tau_{ph,1}^2}\right)+4\frac{\beta_{TPA}}{2\hbar\omega_1}\frac{\left|a_{f,1}\right|^4}{\left(A_{eff}T_{rt}\right)^2}\omega_1\frac{\sigma_{FCD}}{n_g}\Delta\omega_{NL,1}\right)=0\end{aligned} \tag{2.24}$$

By writing $\Delta\omega_{NL,1} = \Delta\omega_1 + \tau_{fc}\frac{\beta_{TPA}}{2\hbar n_g}\left(\frac{|a_{f,1}|^2}{A_{eff}T_{rt}}\right)^2$, we can simplify equation (2.24) as

$$\begin{aligned}&|a_{f,1}|^4\left(\frac{2\tau_{fc}^2}{\tau_{ph,1}}-4\tau_{fc}\right)+|a_{f,1}|^2\left(\frac{4\tau_{fc}\Delta\omega_1}{\tau_{ph,1}}-4\Delta\omega_1\right)+\\&\frac{2}{\tau_{ph,1}}\left(\Delta\omega_1^2+\frac{1}{\tau_{ph,1}^2}\right)+\frac{2}{\tau_{fc}\tau_{ph,1}}\left(\frac{2}{\tau_{ph,1}}+\frac{1}{\tau_{fc}}\right)=0\end{aligned} \tag{2.25}$$

The roots of the above quadratic equation ($|a_{f,1}|_-^2$ and $|a_{f,1}|_+^2$) determine the upper and lower limits of the stored energy for SP to occur. The critical FC lifetime, which is the value τ_{fc} at which SP ceases to exist, occurs when these two limits merge together, $|a_{f,1}|_-^2 = |a_{f,1}|_+^2$. Since the two roots $|a_{f,1}|_-^2$ and $|a_{f,1}|_+^2$ become equal when the determinant of equation (2.25) is zero, we use this condition to obtain the equation for the critical FC lifetime:

$$\left(\frac{\tau_{fc}\Delta\omega_1}{\tau_{ph,1}}-\Delta\omega_1\right)^2-\left(\frac{\tau_{fc}^2}{\tau_{ph,1}}-2\tau_{fc}\right)\left(\frac{1}{\tau_{ph,1}}\left(\Delta\omega_1^2+\frac{1}{\tau_{ph,1}^2}\right)+\frac{1}{\tau_{fc}\tau_{ph,1}}\left(\frac{2}{\tau_{ph,1}}+\frac{1}{\tau_{fc}}\right)\right)=0 \tag{2.26}$$

The above equation is rearranged to obtain a cubic equation for the critical carrier lifetime τ_{fc}:

$$-\frac{2}{\tau_{ph,1}}\left(1+\frac{1}{\tau_{ph,1}^2}\right)\tau_{fc}^3-\tau_{fc}^2+\frac{2}{\tau_{ph,1}}\tau_{fc}+\left(\Delta\omega_1\tau_{ph,1}^2+\frac{1}{\tau_{ph,1}}\right)=0 \tag{2.27}$$

We apply the above analysis to study the nonlinear dynamics of a silicon MRR with the parameters listed in Table 2.1. The MRR is a strip waveguide with dimensions of 320[nm]

$\times 500^{nm}$ and air cladding. The nonlinear parameters of silicon are obtained from [81, 82]. The effective index, group index and effective area of the silicon strip waveguide are calculated for the 1.55 μm wavelength using a full vectorial mode solver. Figure 2.9 shows the stability phase map obtained for the MRR at a fixed phase detune of 0.1π. The map shows the regions of stable (blue), bistable (yellow) and SP (azure) behaviors as a function of the power inside the MRR and the normalized FC lifetime $\tau_n = \tau_{fc}/T_{rt}$ (where T_{rt} is the roundtrip time of the MRR). From the map, we obtain the normalized critical FC lifetime for SP to occur to be $\tau_c = 152\ T_{rt}$. This value is in good agreement with the analytical result $\tau_c = 151.65$ computed using equation (2.27). This value corresponds to a FC lifetime of 1.2 ns, which is in the same range of the FC lifetime in most silicon waveguides [81]. In the SP region of the stability phase map, the values of the dotted contour lines represent the normalized frequencies of the SP oscillation (defined as $f_{sp} \times T_{rt}$). It is evident that the oscillation frequency depends highly on the FC lifetime and the power in the MRR.

Table 2.1, Parameters of silicon MRR

Parameter	Value	Unit
n_{eff}	2.616	-
n_g	4.119	-
τ_{fc}	Variable	ns
a_{rt}	.98	-
R	100	μm
β_{TPA}	0.75×10^{-11}	$m.W^{-1}$
A_{eff}	0.1328×10^{-12}	μm^2
σ_{FCD}	5.3×10^{-27}	m^3
$\tau_{ph,1}$	190	ps
κ_1	0.4	-
$\Delta\varphi_{L,1}$	-0.1π	Radian

In Figure 2.10 we plot the normalized SP frequency as a function of the power in the MRR for a fixed FC lifetime value τ_{fc} = 1.3ns and linear phase detune of 0.1π.

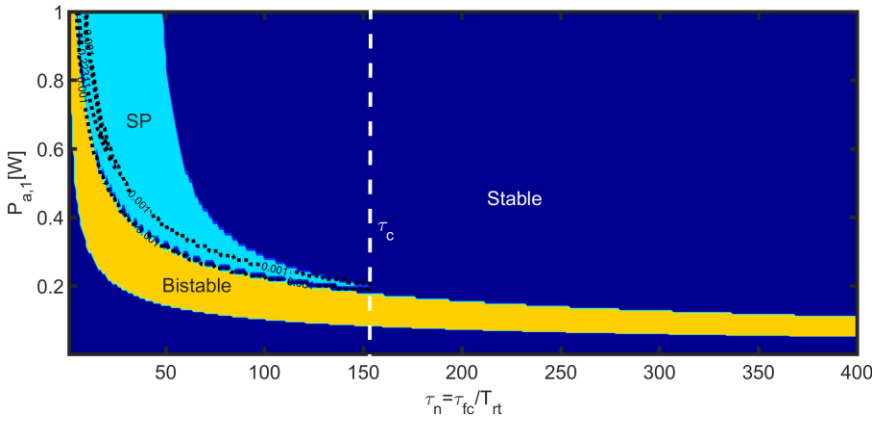

Figure 2.9, Stability phase map of single MRR with linear phase detune 0.1π

The plot shows that the threshold power for SP to occur is about 17mW, which is well within the practical power range that a silicon MRR can handle. We observe that the SP frequency increases as the power is increased beyond the threshold, suggesting that the frequency oscillation can be tuned by varying the input power to the MRR. The normalized oscillation frequency is in the range of 0.011 to 0.016, which corresponds to a frequency range from 1.16 GHz to 1.85 GHz for a 100μm radius MRR.

As figure 2.9 shows, the carrier lifetime is a constraint and can be counted as a reason for not experimentally observation of this effect in MRR.

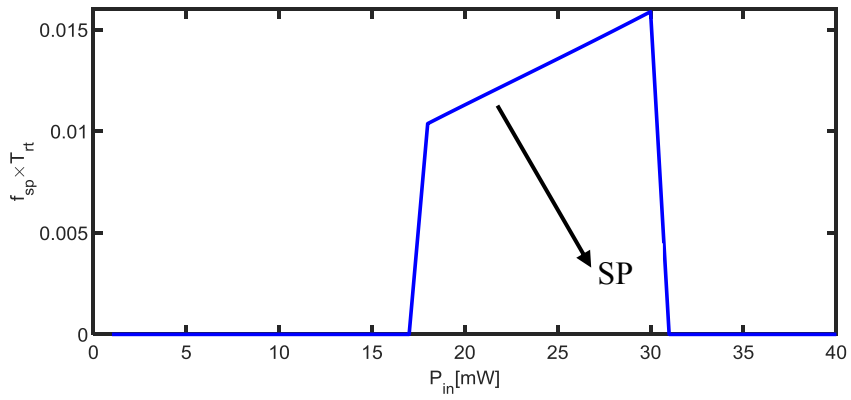

Figure 2.10, The normalized SP frequency as a function of input power for $\Delta\varphi_{L,1}=0.1\pi$ and τ_{fc} = 1. 2ns

To verify the stability analysis based on first-order perturbation, we also performed the time-domain simulations of the MRR by solving equation (2.17) using the finite difference method. We simulated the device with normalized FC lifetime τ_{fc}/T_{rt} = 140 (τ_{fc}=1.23ns), linear phase detune $\Delta\varphi_{L,1}$ = -0.1π, and two different stored power levels: $P_{a,1}$ = 45.4 mW and $P_{a,1}$ = 205mW. Eigenvalue stability analysis shows that the device exhibits stable behavior at the lower power and SP behavior at the higher power, with an oscillation frequency of 1.6249 GHz. The input powers required to reach these stored power levels in the MRR are 23.7 mW and 8.5 mW, respectively.

In the time-domain simulations, we applied the input power to the MRR and computed the stored power in the resonator as a function of time until steady state was reached. The results are shown in figure 2.11(a) for the low input power and 2.11(b) for the high input power. We observe in figure 2.11(a) that after an initial transient period, the power in the MRR becomes stable at around 40 mW, which is close to the value predicted by the eigenvalue analysis. On the other hand, figure 2.11(b) shows that at steady state, the power in the MRR oscillates around a mean value of 150 mW with a frequency of 1.852 GHz. This SP frequency is also close to the value predicted by the eigenvalue

analysis, thus validating the first-order perturbation method for predicting the nonlinear dynamic behavior of the MRR in the presence of non-instantaneous nonlinearity.

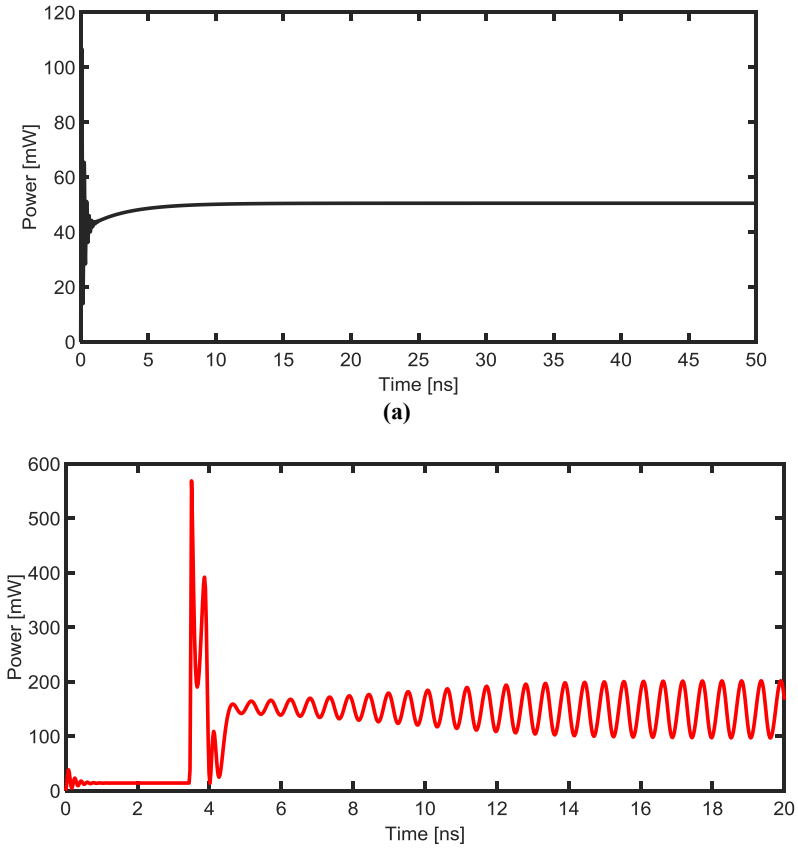

Figure 2.11, The Stored power in a single MRR Vs. Time for input power of (a) 23.7mW and (b) 8.5mW.

Physically, SP in the MRR arises from the periodic interaction between the cavity mode and the nonlinear response of the medium. Silberberg et. al. has studied in detail the influence of the relaxation time of the nonlinearity on the SP mechanism in an optical cavity [48]. If the nonlinearity relaxation time constant is shorter than the roundtrip delay (as in the case of instantaneous nonlinearity), the system exhibits Ikeda instability (or period doubling) and SP cannot occur [48]. On the other hand, if the nonlinear time constant is longer than the cavity roundtrip time, SP will occur instead of period doubling oscillations. For our example of the silicon MRR with a 100 μm radius, the roundtrip

time delay is 8.5 ps whereas the FC lifetime is more than 1ns [81]. We thus expect SP to occur but not Ikeda oscillations, and this is confirmed by the results of our stability analysis (e.g. the phase map in figure 2.9).

As the stability analysis and numerical simulations suggest, the power required to reach SP in the silicon MRR highly depends on the FC lifetime and the linear phase detune. The FC lifetime in silicon is about 1ns, which is in the same range of the maximum critical lifetime τ_c predicted in figure 2.9. Thus it is not generally difficult to observe SP in a silicon waveguide with FC induced nonlinearity. However, our stability analysis in this section is based on the EC model, which may not capture the complete nonlinear dynamics of the MRR. In particular, the model does not account for the effects of adjacent cavity modes. These effects can only be studied with the use of the PC model, which we will develop in the next section.

2.2.2 Power-Space formalism of a Single MRR (PC method)

As predicted by the EC model, free carrier dispersion induces BS and SP in a single MRR. In this section, we show how we can modify the PC model (equation (2.11)) to investigate nonlinear dynamic behaviours of an MRR with non-instantaneous nonlinearity. In particular, we show that the device dynamics is governed by a system of coupled delay-differential equations, instead of a system of coupled differential equations in the EC model (equations (2.17)). The PC model allows us to investigate high-order instability induced by FCD and explore parameter space not available in the EC model.

In a silicon MRR, FCD and FCA cause a nonlinear phase shift and a nonlinear loss, respectively, which can be included in the PC model (equation (2.11)) as follows.

Neglecting Kerr effect in the material, we attribute the nonlinear index change in the MRR due to free carriers generated from TPA, $\Delta n_{NL,1}(t) = n_{core}\sigma_{FCD}N_1(t)/n_{eff}$. This index change causes a roundtrip phase detune equal to $\Delta\varphi_{NL,1}(t) = \Delta n_{NL,1}(t)K_0 2\pi R = (n_{core}\sigma_{FCD}/n_{eff})\, K_0 2\pi R\, N_1(t)$. Additionally, free carrier absorption causes nonlinear loss in the MRR [22] given by $\alpha_{NL}(t) = e^{-\frac{n_{core}\sigma_{FCA}}{n_{eff}}N_1(t)} = e^{-\eta|\varphi_{NL,1}(t)|}$, where σ_{FCA} is the FCA cross-sectional area and η is $\frac{\alpha_{NL}}{\Delta\varphi_{NL,1}} = \frac{\sigma_{FCA}}{\sigma_{FCD}K_0}$. The FC-induced nonlinear phase shift and nonlinear loss are incorporated into equation (2.11) for updating the field in the MRR after each roundtrip time T_{rt} as follows:

$$A_1(t+T_{rt}) = \gamma A_1(t)e^{-j\left(\Delta\varphi_{L,1}+(1-j\eta)\varphi_{NL,1}(t)\right)} - j\kappa_1\sqrt{P_{in}(t)} \qquad (2.28.a)$$

Where γ is $\tau_{cp1\times}a_{rt}$. Since the nonlinear roundtrip phase depends on the FC density, it also satisfies the rate equation

$$\frac{d\varphi_{NL,1}(t)}{dt} + \frac{\varphi_{NL,1}(t)}{\tau_{fc}} = \frac{\beta_{TPA}n_{core}\sigma_{FCD}\pi R}{n_{eff}\hbar c A_{eff}^2}|A_1(t)|^4 \qquad (2.28.b)$$

Equations (2.28.a) and (2.28.b) form a system of nonlinear delay-and-differential equations describing the nonlinear dynamics in a single MRR with FC-induced non-instantaneous nonlinearity. We can obtain the stationary states of the above nonlinear system by setting $A_1(t+T_{rt}) = A_1(t) = A_{f,1}$ and $d\varphi_{NL,1}(t)/dt = 0$. The stationary state could be found as follows:

$$A_{f,1} = \frac{-j\kappa_1\sqrt{P_{in}}}{1-\gamma e^{-(j+\eta)\varphi_{f,1}}} \qquad (2.29)$$

where the stationary roundtrip phase $\varphi_{f,1}$ is given by $\Delta\varphi_{L,1}+\tau_{fc}\xi_{FC}|A_{f,1}|^4$, with the parameter ξ_{FC} defined as $\xi_{FC} = \frac{\beta_{TPA} n_{core} \sigma_{FCD} \pi R}{n_{eff} \hbar C A_{eff}^2}$. From the stationary solution for the field inside the MRR, we can determine the input power applied to the bus waveguide from

$$\frac{P_{a,1}}{P_{in}} = \frac{g^2}{1 + F \sin^2\left(\frac{\varphi_{f,1}}{2}\right)} \tag{2.30}$$

where $g = \kappa_1(1-a_{rt}\alpha_{NL})^{-1}$ and $F = 4a_{rt}\alpha_{NL}(1- a_{rt}\alpha_{NL})^{-2}$. The parameters F and g represent the contrast factor and the gain in the MRR at resonance, respectively.

To study the stability of a stationary solution $A_{f,1}$, we again apply the stability analysis based on first-order perturbation. Adding a small perturbation of $\varepsilon_{A,1}(t)$ and $\varepsilon_{\varphi NL,1}(t)$ to the field amplitude and nonlinear phase shift, we get $A_1(t)=A_{f,1}+\varepsilon_{A,1}(t)$ and $\varphi_{NL,1}(t)=\varphi_{f,1}+\varepsilon_{\varphi NL,1}(t)$. By substituting these perturbed values into equations (2.28) and keeping only first-order perturbation terms, we have

$$\varepsilon_{A,1}(t+T_{rt}) = \gamma\alpha_{NL} e^{-j\varphi_{f,1}}\left[\varepsilon_{A,1}(t) + (\eta - j)A_{f,1}\varepsilon_{\varphi_{NL,1}}(t)\right] \tag{2.31.a}$$

$$\frac{d\varepsilon_{\varphi_{NL,1}}(t)}{dt} + \frac{\varepsilon_{\varphi_{NL,1}}(t)}{\tau_{fc}} = 2\xi_{FC}\left|A_{f,1}\right|^2\left[A_{f,1}\varepsilon^*_{A,1}(t) + A^*_{f,1}\varepsilon_{A,1}(t)\right] \tag{2.31.b}$$

Replacing the ansatz $\varepsilon_{A,1}(t)=A_0e^{st}$ and $\varepsilon_{\varphi NL,1}(t)=\varphi_0e^{st}$ into equations (2.31), we obtain the following characteristic equation in the Laplace domain (or z-domain if we set $z=e^{sTrt}$):

$$\begin{aligned}&(e^{sT_{rt}} + \gamma^2\alpha_{NL}^2 e^{-sT_{rt}} - 2\gamma\alpha_{NL}\cos\varphi_{f,1})(s\tau_{fc}+1) = \\ &4\gamma\alpha_{NL}\varphi_{NL,1}(\eta\cos\varphi_{f,1} - \sin\varphi_{f,1} - \eta\tau_{cp,1}a_{rt}\alpha_{NL}e^{-sT_{rt}})\end{aligned} \tag{2.32}$$

Solutions of s with a negative real part correspond to stable fields in the MRR. On the

other hand, if the real part of s is positive, the field exhibits unstable behavior. In this case, SP occurs if s is complex (has a non-zero imaginary part) and bistability occurs if s is real. In Section 2.2.3, we will first investigate the nonlinear dynamics of the MRR in the absence of FCA, which greatly simplifies equation (2.32). The deleterious effect of nonlinear loss due to FCA on the device dynamics will be studied in Section 2.2.4.

2.2.3 Nonlinear Dynamics in the Absence of FCA

We begin by determining the conditions for bistability and SP to occur in the microring resonator when FCA is absent. The boundaries of the bistability regions can be found from the condition that the root s is zero. In the absence of FCA, we have $\alpha_{NL}=1$ and $\eta = 0$. In this case, setting s=0 in equation (2.32) gives

$$\cos\varphi_{f,1} - 2\varphi_{NL,1}\sin\varphi_{f,1} = B_1 \tag{2.33}$$

where $B_1=(1+\gamma^2)/2\gamma$. Solution of equation (2.33) gives the threshold values of $\varphi_{NL,1}$ at which bistability begins to occur. Note that these threshold values do not depend on the FC lifetime. For high-Q microring resonators, $B_1\approx1$, in which case equation (2.33) reduces to $\tan\frac{\varphi_{f,1}}{2} = -2\varphi_{NL,1}$. This equation shows that for a given linear phase detune $\Delta\varphi_{L,1}$, a pair of roots for $\varphi_{NL,1}$ exists for each 2π increment of $\varphi_{f,1}$. Each pair of roots defines the boundaries (or thresholds) of the bistable region for that branch of the stability curve.

For the SP regions, the thresholds occur at the Hopf bifurcation points, which correspond to imaginary solutions of s. Setting $s=j\omega$ in equation (2.33) and separating the real and imaginary parts, we obtain the expressions

$$\cos\varphi_{f,1} = B_1\cos\Omega + B_2\sin\Omega/\Omega\tau_n \tag{2.34.a}$$

$$2\varphi_{NL,1}\sin\varphi_{f,1} = B_2(\Omega\tau_n + 1/\Omega\tau_n)\sin\Omega \tag{2.34.b}$$

where $\tau_n=\tau/T_{rt}$, $\Omega=\omega T_{rt}$, and $B_2=1-\gamma^2/2\gamma$. The above equations are solved to give the threshold values of $\varphi_{NL,1}$ at which SP begins to occur and the normalized oscillation frequency Ω. The solutions of the coupled equations (2.34) can be sought by writing

$$\varphi_{f,1} = \varphi_{F1}(\Omega) = \cos^{-1}\left(B_1\cos\Omega + \frac{B_2\sin\Omega}{\Omega\tau_n}\right) + 2m\pi \tag{2.35.a}$$

$$\varphi_{f,1} = \varphi_{F2}(\Omega) = \Delta\varphi_{L,1} + \varphi_{NL,1} = \Delta\varphi_{L,1} + (\Omega\tau_n + 1/\Omega\tau_n)\frac{B_2\sin\Omega}{2\sin\varphi_{f1,1}} \tag{2.35.b}$$

where m is an integer indicating the branch order. Figure. 2.12 shows the plots of $\varphi_{f1,1}$ and $\varphi_{f2,1}$ vs. Ω for an MRR with γ = 0.97 (finesse $\mathcal{F}\approx100$), linear phase detune $\Delta\varphi_{L,1}$= -0.1π, and two different values of the normalized FC lifetime, τ_n = 200 and τ_n = 2000.

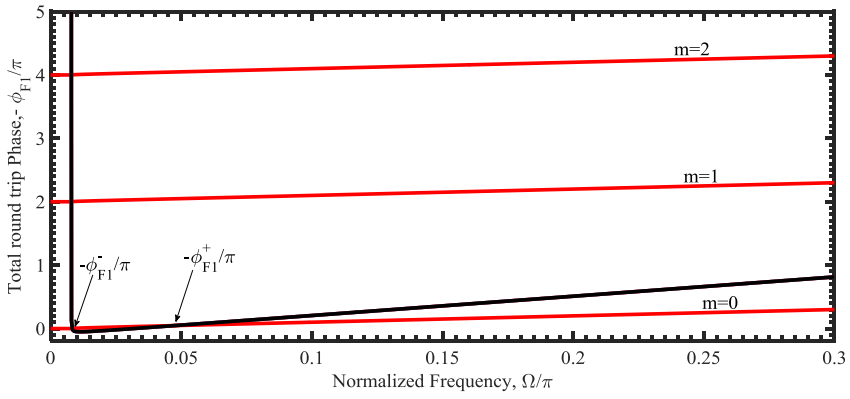

(a)

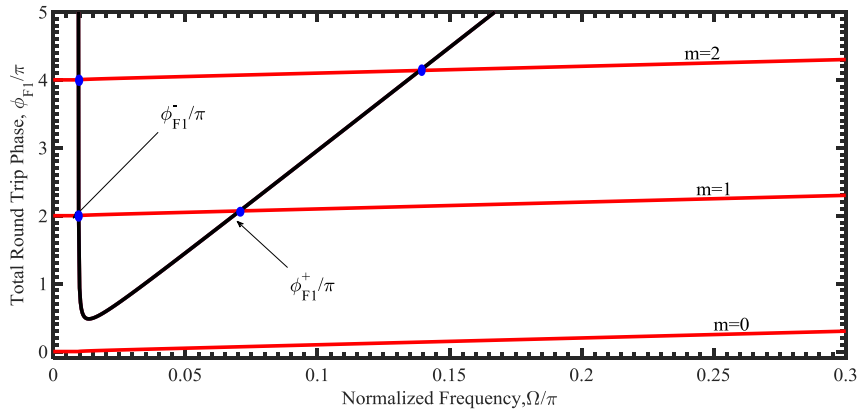

(b)

Figure 2.12, The $\varphi_{f,1}$ vs. the normalized oscillation frequency Ω showing solutions of the SP thresholds for different branch orders m. The MRR parameters are γ= 0.97, $\Delta\varphi_{L,1}$= 0.1π, (a) τ_n= 200 and (b)τ_n=2000

For each branch order m, a pair of solutions for φ_{F1} exists which defines the lower and upper bounds $\{\varphi_{NL,1}^{(\pm)}\}$ of the SP region. These solutions can be approximated by replacing the sine and cosine functions in equation (2.35) with their small argument approximations. Letting $\varphi_F = \varphi_{F0} + 2m\pi$, we then get

$$\varphi_{F0}^2 \approx B_1\Omega^2 - B_3 \tag{2.36.a}$$

$$\varphi_{F0} + 2m\pi \approx \Delta\varphi_{L,1} + (\Omega\tau_n)\frac{B_2\Omega}{2\varphi_{F0}} \tag{2.36.b}$$

where $B_3=(1-\gamma)^2/\gamma$. The above equations can be combined to give a quadratic equation in φ_{F0}, whose solution yields the following threshold values for $\varphi_{NL,1}$:

$$\varphi_{NL,1}^{(\pm)} = \frac{(\Theta-1)\Delta\varphi_{L,m} \pm \sqrt{\Phi_{L,m}^2 + B_3\Theta(2-\Theta)}}{2-\Theta} \tag{2.37}$$

where $\Delta\varphi_{L,m} = \Delta\varphi_{L,1} - 2m\pi$ and $\Theta = \tau_n B_2 / B_1$. When the discriminant under the square root sign is negative, the threshold values of φ_{NL1} do not exist, implying that SP does not occur. Using this condition, we find that for a fixed linear phase detune, SP only occurs if the normalized FC lifetime is less than a critical value τ_c given by

$$\tau_c = (B_1/B_2)\left(1+\sqrt{1+\Phi_{L,m}^2/B_3}\right) \tag{2.38}$$

In figure 2.13 we plot the SP threshold values $\{\varphi_{NL,1}^{(\pm)}\}$ as functions of the normalized FC lifetime τ_n for several values of the linear phase detune $\Delta\varphi_{L,1}$. Figure 2.13 (a) shows the regions of SP on the first branch (m = 0) while figure 2.13(b) shows the SP regions on the second branch (m = 1).

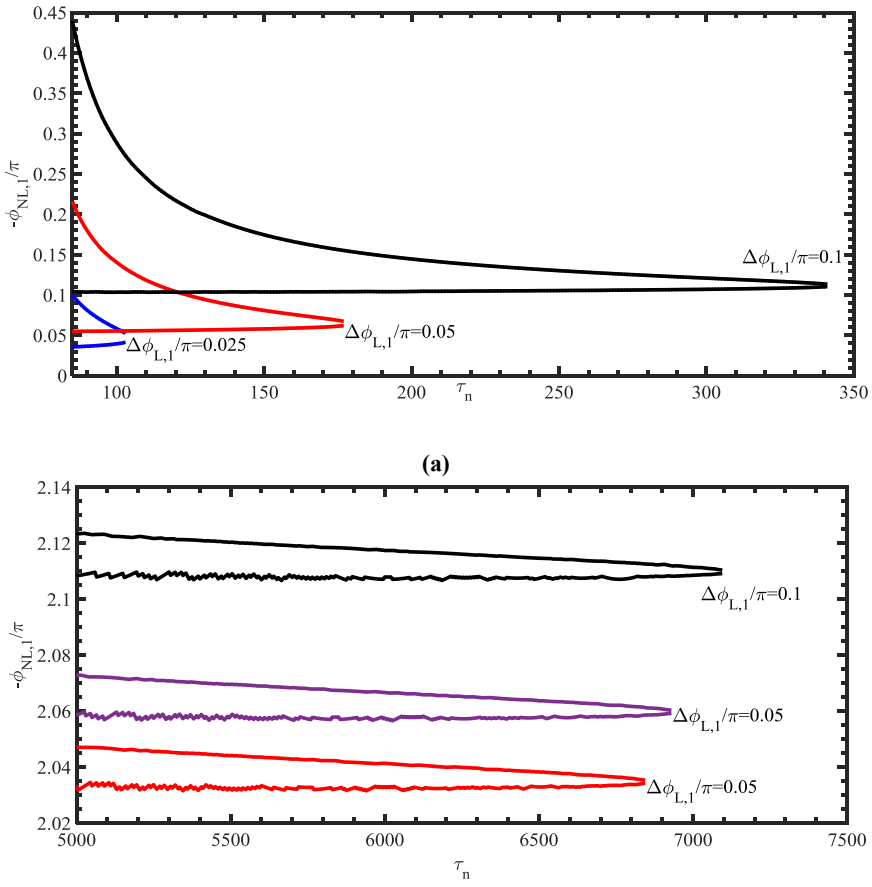

Figure 2.13, The onset of SP $\{\varphi_{NL,1}\pm\}$ vs. the normalized FC lifetime τ_n for several values of the linear phase detune: (a) the 1st branch (m = 0) and (b) the 2nd branches (m = 1)

In both plots we observe that for a fixed linear phase detune, there exists a maximum normalized FC lifetime value for which SP can occur. The critical τ_c values on the first branch are the same as those predicted using the EC stability analysis in the previous

section. On the second branch, there is also a maximum value for τ_n ($\tau_c \sim 6800$) for which SP can occur, but this value is much larger than the critical values on the first branch, by as much as an order of magnitude for linear phase detunes up to -0.1π. As an example, considering that a silicon MRR with a radius of 10μm has a roundtrip time $T_{rt} \sim$ 0.8ps, the above result predicts that SP can occur on the second branch for FC lifetime as long as 6ns, which is longer than the carrier lifetime in a typical silicon waveguide ($\tau_{fc} \sim$1 ns). On the other hand, the critical τ_c values on the first branch correspond to FC lifetimes in the range of 100ps - 360ps for linear phase detune values up to -0.1π. These values are much shorter than typical 1 ns FC lifetimes in silicon waveguides so that SP cannot occur on the first branch. This example illustrates the advantage of exploiting high-order instability to achieve FC-induced SP in semiconductor microcavities.

By comparing the results of critical lifetime of SP of 10μm and 100μm, we learn that observation of SP in the first branch of Bistability is more probable in the microring with higher radius.

In figure 2.14. (a) we plot the threshold values $\{\varphi_{NL,1}^{(\pm)}\}$ for both regions of bistability and SP as functions of the linear phase detune $\Delta\varphi_{L,1}$ for a fixed value $\tau_n = 1000$. The regions of bistability and SP on the first branch are shown in figure 2.14(a) while those on the second branch are shown in figure 2.14 (b). We observe that on the first branch, SP occurs only in a narrow region for linear phase detune $\Delta\varphi_{L,1} < -0.3\pi$ while the SP region is much larger on the second branch and there is no minimum value for the linear phase detune. We also look at the range of oscillation frequencies that can be achieved by plotting in figure 2.14 (c) the normalized frequency of oscillation Ω at the SP threshold values $\varphi_{NL,1}^{(\pm)}$ for both the first and second branches. We observe that a much larger

range of oscillation frequencies can be achieved on the second branch compared to the first branch. In addition, the frequency can be varied by changing the linear phase detune. For example, for linear phase detune $\Delta\varphi_{L,1} = -0.4\pi$, the oscillation frequencies at the lower and upper SP thresholds of the second branch are 0.01 and 0.16, respectively. These values correspond to an oscillation frequency range of 1.6GHz – 25GHz for a 10-μm radius silicon MRR. We note that the upper frequency limit is 6.5 times larger than the corresponding upper value that can be achieved on the first branch. Thus, not only is it easier to observe FC-induced SP on the second branch, the frequency of oscillation is also higher and tunable over a wider range than on the first branch. The above results show that the FC lifetime has a lesser influence on higher-order instability of the MRR than instability on the lowest branch. The reason for this may be explained by the fact that instability on higher-order branches is typically characterized by oscillations at much higher frequencies than the FC relaxation rate, so that the FC lifetime plays a less important role in the nonlinear dynamics of the resonator.

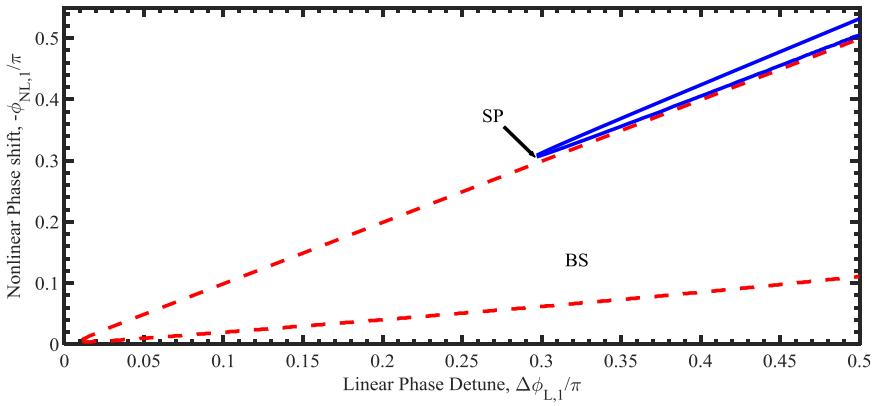

(a)

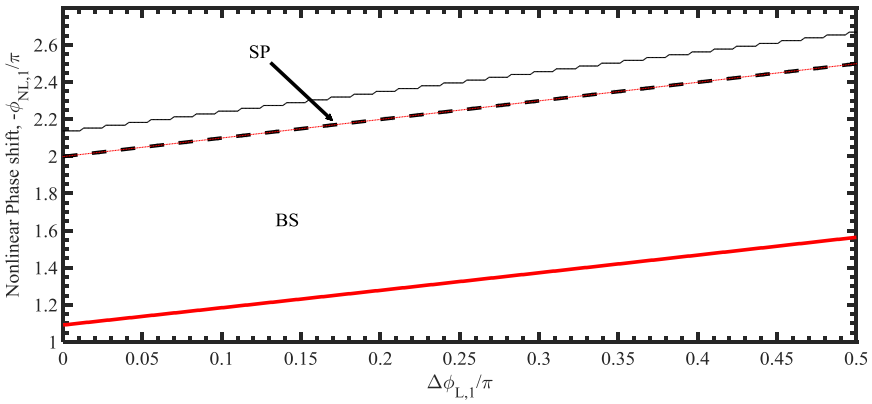

(b)

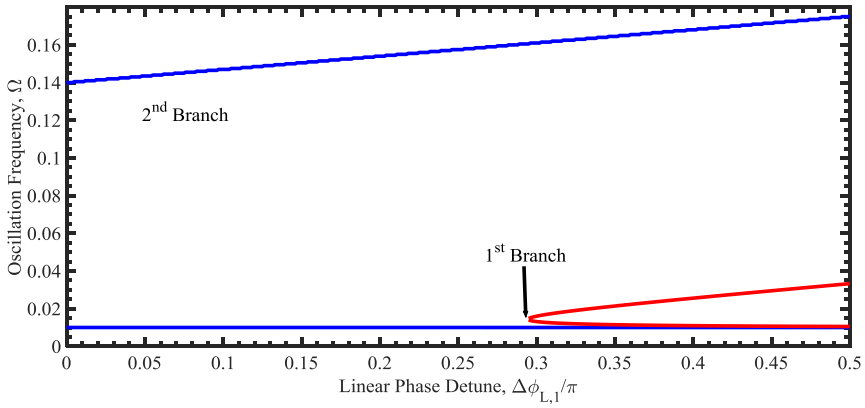

(c)

Figure 2.14, the threshold values {$\varphi_{NL,1\pm}$} vs. linear phase detune for τ_n = 1000, presenting BS and SP regions in (a) the 1st (m = 0) and (b) the 2nd branches (m = 1). (c) The normalized oscillation frequency Ω at the upper and lower SP thresholds {$\varphi_{NL,1\pm}$}

2.2.4 FC Induced Nonlinear Dynamics in an MRR with FCA

In the presence of free carrier absorption, equation (2.35) for the SP thresholds are modified as follows:

$$\cos\varphi_{f,1} = C_1\cos\Omega + (C_2 - 2\eta\gamma\alpha_{NL}\varphi_{NL,1})\sin\Omega/\Omega\tau_n \tag{2.39.a}$$

$$C_2(\Omega\tau_n + 1/\Omega\tau_n)\sin\Omega - 2\eta\gamma a_{NL}\varphi_{NL,1}(\cos\Omega + \sin\Omega/\Omega\tau_n) = 2\varphi_{NL,1}(\sin\varphi_{f,1} + \eta\cos\varphi_{f,1}) \tag{2.39.b}$$

where $C_1 = [1+(\gamma\alpha_{NL})^2]/2\gamma\alpha_{NL}$ and $C_2 = [1-(\gamma\alpha_{NL})^2]/2\gamma\alpha_{NL}$. Figures 2.15 (a) and (b)

show the SP regions on the first branch and second branch, respectively, for an MRR with $\gamma = 0.97$. The FC ratio is set at $\eta = 2\%$, which is typical for silicon near the 1.55μm wavelength. Compared to figure 2.14(a) and (b) (where $\eta = 0$), we observe that the effect of FCA is to reduce the range of FC lifetimes (i.e., the τ_c values) on both branches for which SP can occur. However, the τ_c value on the second branch is insensitive to the linear phase detuning whereas it decreases rapidly with smaller phase detunes on the first branch. We note that in general, it is more advantageous to operate the resonator at smaller phase detunes because the power in the microring is enhanced near a resonance, which leads to smaller input power requirement.

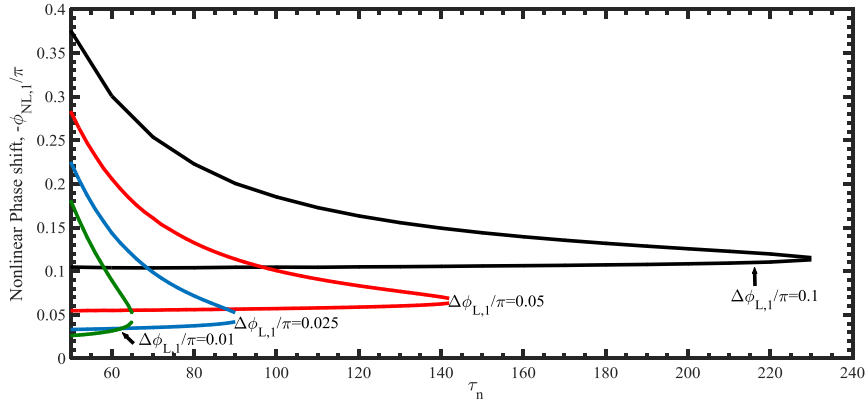

(a)

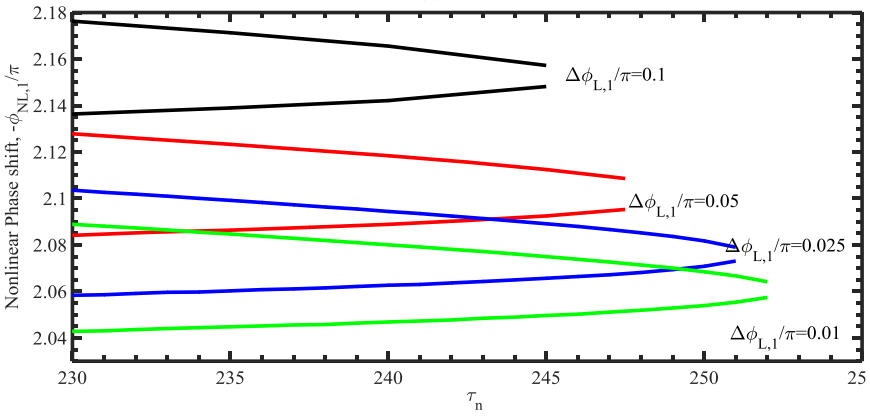

(b)

Figure 2.15, The SP thresholds vs. the normalized FC lifetime τ_n with FC parameter η= 2% and for several values of the linear phase detune: (a) the 1st (m = 0) and (b) the 2nd branches

The FC parameter η has a strong influence on the SP thresholds for both the first and second branches. In general, the SP region becomes larger as the η value decreases, which implies smaller FCA effect. Figure 2.16 (a) shows the dependence of the critical FC lifetime τ_c on the linear phase detune $\Delta\varphi_{L,1}$ for different values of η for both the first and second branches. The cavity loss factor is fixed at $\gamma = 0.97$. The plot indicates that η has a strong influence on τ_c, especially on the second branch. We also observe that on the first branch, τ_c increases with increasing linear phase detune whereas it is insensitive to $\Delta\varphi_{L,1}$ on the second branch. For small values of $\Delta\varphi_{L,1}$, the critical FC lifetime on the second branch is larger than the corresponding value on the first branch, implying that FC lifetime has a lesser influence on instability on the second branch than the first. Figure 2.16(b) shows the dependence of τ_c on the cavity loss factor γ for different values of η. The linear phase detune is fixed at $\Delta\varphi_{L,1} = -0.1\pi$. For both branches, τ_c increases as the total loss in the cavity is reduced (higher γ values). It is also seen that for larger cavity losses (smaller γ values), the FC lifetime has less influence on the SP threshold on the second branch compared to the first. Thus, it can be concluded from the results in this section that SP on the second branch is generally less susceptible to linear loss (γ) and FCA (η) compared to the first branch.

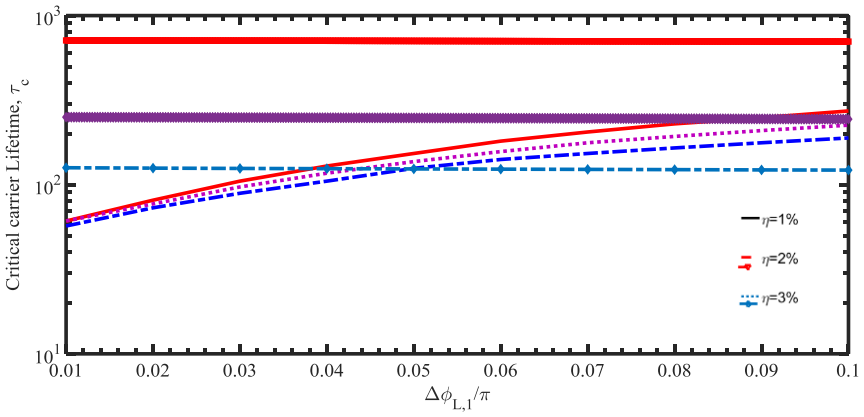

(a)

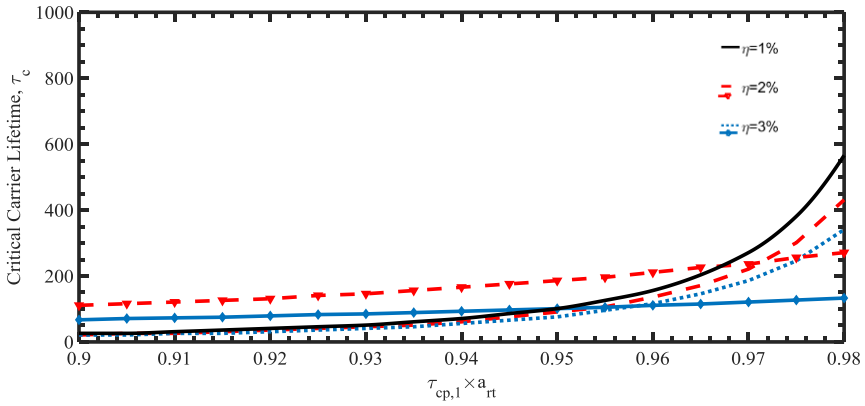

(b)

Figure 2.16, The normalized critical FC lifetime τ_c to have SP vs. the linear phase detune for different values of the FC parameter η. The cavity loss factor is fixed at γ= 0.97. (b) Plot of the normalized critical FC lifetime τ_c vs. the cavity loss

2.2.5 Routes to Self-pulsation on the second branch

We now discuss the possible routes to reach SP on the upper branch of the stability curve. To give a concrete example, we consider a silicon MRR with radius R = 200μm, effective index n_{eff} = 2.5, group index n_g = 4.9, coupling coefficient κ_1 = 0.35 and cavity loss factor γ = 0.92. For silicon near the 1.55μm wavelength, the FC refraction volume and absorption cross-section are $\sigma_{FCD} = -4.5\times10^{-21}$ cm^3 and $\sigma_{FCA} = 0.8\times10^{-17}$ cm^2 [83], which gives $\eta \sim 2\%$. Figure 2.17(a) shows the stationary solution $\varphi_{NL,1}$ as a function of the input power P_{in} for linear phase detune $\Delta\varphi_{L,1} = 0$ and τ_{fc} = 2ns. The regions of bistability and SP are also indicated on the curve. It can be seen that SP occurs only on the second branch; however, in order to reach this instability region, one would have to overcome the first bistability knee by increasing the input power to over 5.5W, which is impractical for the silicon microring device. The maximum power could be handled by an SOI waveguide highly depends on the waveguide dimension and optical waveform (CW or Pulse). A calculation shows that a conventional waveguide with dimension of $220^{nm} \times 500^{nm}$ can tolerate CW power up to 1.5Watt before permanent damage happens [8]

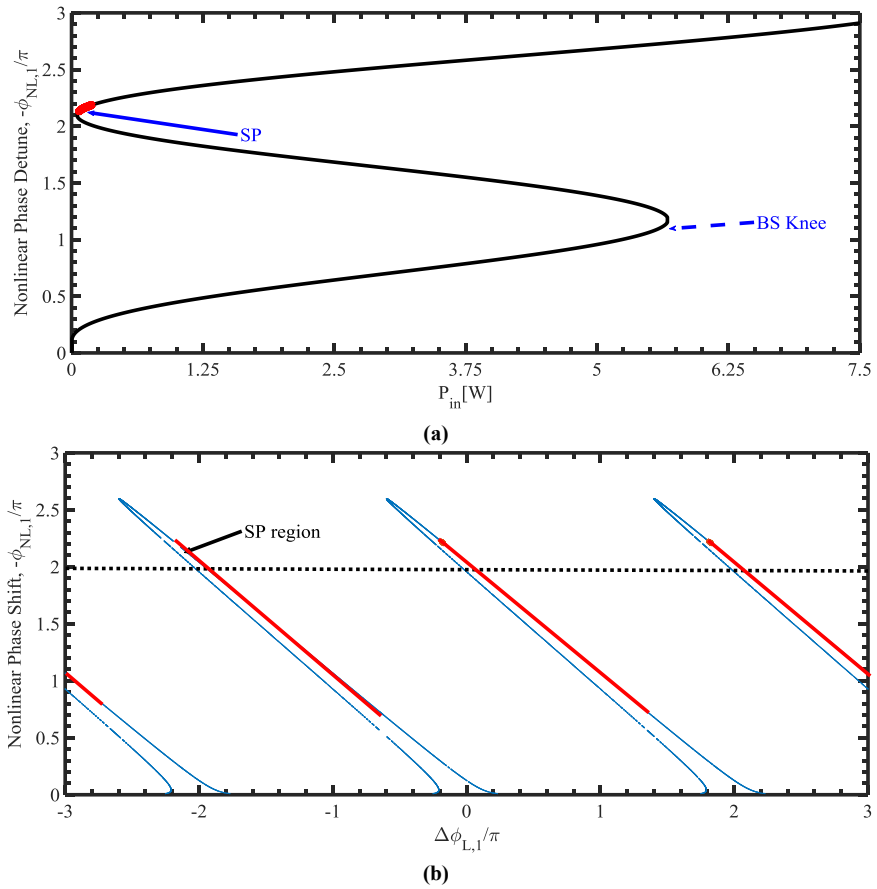

Figure 2.17, (a) Plot of the stationary solutions of $\varphi_{NL,1}$ vs. input power for $\Delta\varphi_{L,1} = .1\pi$ and $\tau_{fc} = 2$ns. (b) Plot of the stationary solutions of $\varphi_{NL,1}$ vs. linear phase detune $\Delta\varphi_{L,1}$ for $\tau_n = 100$ and Pin = 100mW.

We propose here a route to reach SP on the second branch which does not require prohibitively high input CW power. The method is based on tuning the linear phase to reach the instability region. Figure 2.17(b) shows the plot of the stationary solution $\varphi_{NL,1}$ as a function of the linear phase detune $\Delta\varphi_{L,1}$ for a fixed input power P_{in} = 100mW. The SP regions are also indicated on the curve. It can be seen that SP on the second branch can be reached by initially detuning the linear phase by slightly more than 2π, then decreasing the phase detune until it reaches near zero. As the linear phase is decreased, the nonlinear phase shift will follow the upper branch of the curve to reach the SP region on the second branch. Note that the input power is still maintained at a fixed level of 100mW, which is much smaller than the value required to overcome the bistability knee

in figure 2.17(a). In general, for a fixed FC parameter η, the input power required to reach SP on the second branch can be reduced by increasing the microring radius, which has the effect of decreasing the normalized FC lifetime τ_n.

To verify the phase tuning method, we performed time-domain simulation of the MRR with a fixed CW input of 100mW and initial linear phase detune $\Delta\varphi_{L,1} = 2\pi$. After the power in the microring has reached steady state (inset (i) of figure 2.18(a)), we began to decrease $\Delta\varphi_{L,1}$ to zero at rate of about $-\pi/4$ rad/μs. Figure 2.18(a) shows the time trace of the power in the microring when $\Delta\varphi_{L,1}$ has reached zero.

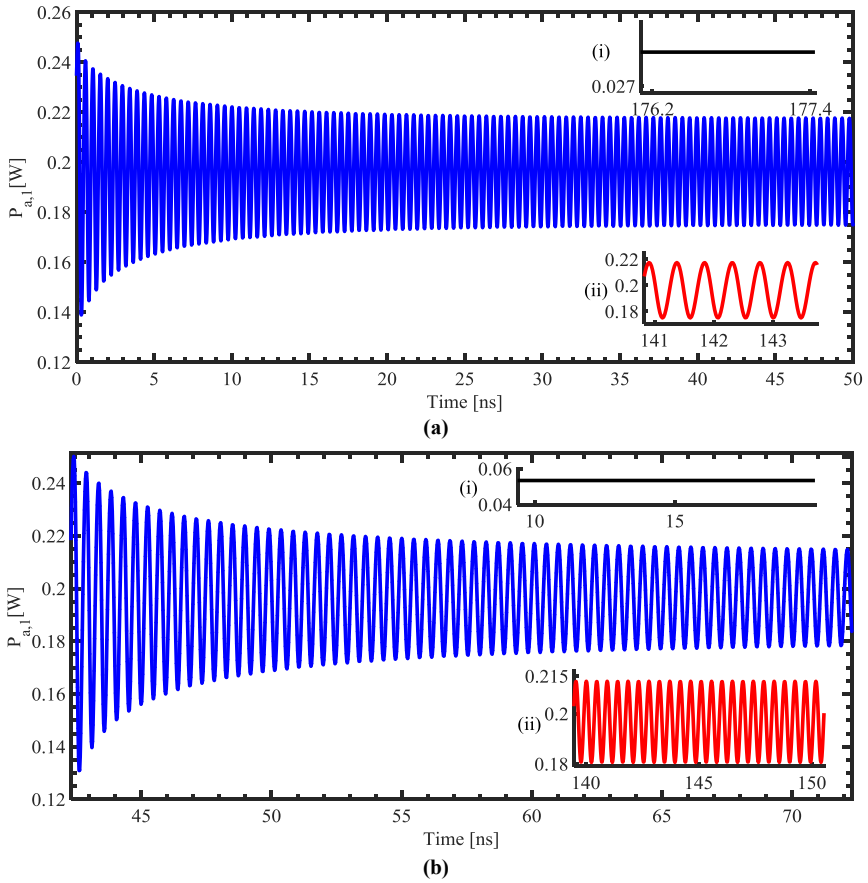

Figure 2.18, Time trace of the power in the microring exhibiting SP behavior on the second branch reached by (a) linear phase tuning and (b) ultrafast pulse excitation. In each plot, inset (i) shows the initial steady state before excitation and inset (ii) shows a zoomed-in view of the oscillations after excitation.

We observe that after a short transient time, the power reaches a state of stable

oscillation, with a period of 2.2 GHz. From our stability analysis, we obtained a SP period of 2.1 GHz at this stationary point, which is close to the value obtained from the time-domain simulation. It is also possible to reach the second branch of the stability curve by applying an ultrafast control pulse to the resonator with a sufficiently high peak power to overcome the bistability knee. For demonstration and comparison with the linear phase tuning method, we also performed time-domain simulation to verify that SP can be reached by ultrafast pulse excitation. We initially applied 100mW of CW power to the microring with zero linear phase detune. After the device reached steady state (inset (i) of figure 2.18(b)), we applied an optical pulse with 123.15 ps pulse width and 4W peak power. The pulse energy delivered to the device is 490 pJ, which is small enough that there should be no damage to the silicon microring. The time trace of the power in the microring after the application of the pulse is shown in figure 2.18(b). We observe that the power also reaches stable oscillation after an initial transient period. The SP frequency is 2.1 GHz, which agrees with the result obtained from the linear phase tuning method, indicating that optical pulse excitation is also an effective route to reach higher-order instability.

2.3 Summary

In this chapter we studied in detail the nonlinear dynamics of a single MRR with instantaneous (Kerr) and non-instantaneous (FCD) nonlinearity. We utilized, as numerical examples, chalcogenide glass for the former device and silicon for the latter. For each device, we used both the EC and PC formalisms to study the different nonlinear dynamical behaviours, including bistability (or multistability), self-pulsation and Ikeda

instability. We showed that the EC model cannot predict Ikeda instability in an MRR with instantaneous Kerr nonlinearity. Using the PC model, we also investigated higher-order instability in an MRR with TPA-generated FCD and showed that SP on the second-order branch of the stability curve offers several advantages, including higher critical FC lifetime, higher oscillation frequencies, wider linear phase detune range, and insensitivity of the critical FC lifetime to linear phase detune. Finally, we proposed two alternative methods for reaching the second-order SP in a silicon MRR without requiring prohibitively high CW powers, namely, linear phase sweeping and ultrafast pulse excitation. The validity of these methods was also verified by rigorous time-domain simulations.

3 Nonlinear Dynamics in Coupled Microring Resonators

In the previous chapter we studied the nonlinear dynamics of a single MRR with instantaneous and non-instantaneous nonlinearities. We found that there are several practical challenges to achieving SP in a nonlinear MRR, including prohibitively high CW threshold power, requirement of fast nonlinear relaxation time, and the deleterious effect of nonlinear loss. In this chapter, we introduce spatial complexity to the nonlinear system with the aim of exploring the feasibility of relaxing many of these practical constraints. In particular, by forming a system of coupled microring resonators (CMRRs), the rich spectral characteristics and nonlinear interactions between cavities can open up a wide range of dynamic behaviors that are more easily accessed. We will extend the EC and PC stability analyses employed in Chapter 2 to analyze the nonlinear dynamics of CMRRs with instantaneous and non-instantaneous nonlinearities. We will again consider the Kerr effect in chalcogenide glass as an example of instantaneous nonlinearity, and FC effects in silicon as an example of non-instantaneous nonlinearity.

Nonlinear dynamics such as BS, SP and chaos in CMRRs with various types of nonlinearities have been investigated using the EC formalism. For example, Zhu et. al. analyzed and demonstrated nonlinear dynamics such as bistability and chaos in a silicon CMRR with thermo-optic origin [84]. Armaroli et. al. also investigated BS and SP due to Kerr effect in three coupled microcavities [85] and Grigoriev et. al. also analyzed self-pulsation in couple microcavities with Kerr nonlinearity [86]. In this chapter, we will

develop a general EC formalism that can be used to analyze the nonlinear dynamics of a chain of N_z coupled MRRs.

On the other hand, the PC formalism has not been used to analyze the nonlinear dynamics of CMRRs. As we discussed in the previous chapter, although the EC model allows for simpler analysis, its validity is limited to low powers and small linear phase detunes from a resonance. Since the PC model has more general validity, it allows us to study the nonlinear behaviours of CMRRs under a broader range of conditions. For this purpose, we will develop a general PC formalism based on the transfer matrix method that can be used to analyze the stability of a chain of N_z coupled MRRs with instantaneous nonlinearity.

This chapter is organized as follows. In section 3.1 we develop the EC and PC formalisms for analyzing the nonlinear dynamics in a CMRR system consisting of two microrings (i.e., a double CMRR) with instantaneous Kerr nonlinearity. Double CMRRs with non-instantaneous nonlinearity will be investigated in section 3.2. For each case, numerical examples based on the chalcogenide and silicon materials will be presented and compared with the nonlinear dynamics of single MRRs. In section 3.3, we will extend the analysis of double CMRRs to a chain of CMRRs of finite length N_z. In particular, we will develop matrix formalisms based on the EC and PC models to investigate the nonlinear dynamics of spatially extended CMRR structures, also known as CROWs (coupled resonator optical waveguides). The chapter is concluded in section 3.4 with a summary.

3.1 Instability in a Double CMRR with Instantaneous Nonlinearity

Figure 3.1 shows a schematic of a CMRR system consisting of two coupled microrings.

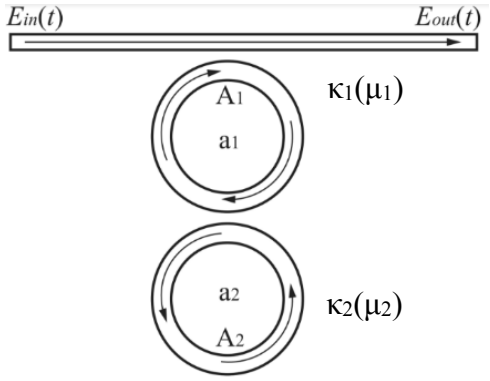

Figure 3.1, Schematic of a double Coupled Microring Resonators (CMRR) structure

We denote the field coupling coefficient between the straight bus waveguide and microring 1 as κ_1 and between the two microrings as κ_2. From these field coupling coefficients, we can also obtain the corresponding energy coupling coefficients as $\mu_1=\kappa_1\times T_{rt}^{-0.5}$ and $\mu_2=\kappa_2\times T_{rt}^{-1}$ [74]. We denote the field circulating in microring 1 as A_1 and in microring 2 as A_2, normalized such that $|A_i|^2$ represents the power in microring i. The corresponding energy stored in microring i is also given by $|a_i|^2 = |A_i|^2 T_{rt}$. The power applied to the input of the bus waveguide is $|E_{in}(t)|^2$ and the transmitted power at the output is denoted by $|E_{out}(t)|^2$. We analyze the stability of the device using the EC model in Section 3.1.1 and the PC model in Section 3.1.2. Energy-Time Coupling model (EC method)

We modify the EC equation for a single MRR with instantaneous Kerr nonlinearity (equation (2.4)) to account for the coupling μ_2 between the two microrings in the CMRR. The equations describing the rates of energy change in microrings 1 and 2 become:

$$\frac{da_1(t)}{dt} = \left(j\left[\Delta\omega_1 - \omega_1\gamma_{Kerr}\left|a_1(t)\right|^2\right] - \frac{1}{\tau_{ph,1}} \right) a_1(t) - j\mu_2 a_2(t) - j\mu_1\sqrt{P_{in}(t)} \tag{3.1.a}$$

$$\frac{da_2(t)}{dt} = \left(j\left[\Delta\omega_2 - \omega_2\gamma_{Kerr}\left|a_2(t)\right|^2\right] - \frac{1}{\tau_{ph,2}} \right) a_2(t) - j\mu_2 a_1(t) \tag{3.1.b}$$

In the above equations, ω_i and $\Delta\omega_i$ (i = 1, 2) are the resonant frequency and the linear frequency detune, respectively, of microring I, and $\gamma_{Kerr} = n_2(n_g A_{eff} T_{rt})^{-1}$ is the effective Kerr coefficient. The cavity lifetimes $\tau_{ph,1}$ and $\tau_{ph,2}$ of microrings 1 and 2 are related to the linear loss α_0 and the coupling coefficients as follows [74]:

$$\tau_{ph,1} = \left(\frac{\mu_1^2}{2} + \frac{1}{\alpha_0 v_g} + \frac{\mu_2}{2} \right)^{-1} \tag{3.2.a}$$

$$\tau_{ph,2} = \left(\frac{\mu_2}{2} + \frac{1}{\alpha_0 v_g} \right)^{-1} \tag{3.2.b}$$

Equations (3.1.a) and (3.1.b) form a coupled nonlinear dynamical system. The stationary solutions can be obtained by setting the time derivatives $da_{f,1}/dt = 0$ and $da_{f,2}/dt = 0$ and solving for $a_{f,1}$ and $a_{f,2}$ to get

$$a_{f,1} = \frac{1}{\mu_2}\left(\left[\Delta\omega_2 - \omega_2\gamma_{Kerr}\left|a_{f,2}\right|^2\right] + \frac{j}{\tau_{ph,2}} \right) a_{f,2} \tag{3.3.a}$$

$$\sqrt{P_{in}} = \frac{1}{\mu_1}\left(\left[\Delta\omega_1 - \omega_1\gamma_{Kerr}\left|a_{f,1}\right|^2\right] + \frac{j}{\tau_{ph,1}} \right) a_{f,1} - \frac{\mu_2}{\mu_1} a_{f,2} \tag{3.3.b}$$

To determine the stability of the system around the stationary point, we add a small

perturbation to the stationary solutions: $a_1(t) = a_{f,1} + \varepsilon_{a,1}(t)$ and $a_2(t) = a_{f,2} + \varepsilon_{a,2}(t)$. Substituting these expressions into equations (3.1.a) and (3.1.b), we get

$$\begin{aligned}\frac{d\left(a_{f,1}+\varepsilon_{a,1}(t)\right)}{dt} = &\left(j\left[\Delta\omega_1 - \omega_1\gamma_{Kerr}\left(\left|a_{f,1}\right|^2 + a_{f,1}^{*}\varepsilon_{a,1}(t) + a_{f,1}\varepsilon_{a,1}^{*}(t)\right)\right] - \frac{1}{\tau_{ph,1}}\right)\left(a_{f,1}+\varepsilon_{a,1}(t)\right) \\ &- j\mu_2\left(a_{f,2}+\varepsilon_{a,2}(t)\right) - j\mu_1\sqrt{P_{in}(t)}\end{aligned} \tag{3.4.a}$$

$$\begin{aligned}\frac{d\left(a_{f,2}+\varepsilon_{a,2}(t)\right)}{dt} = &\left(j\left[\Delta\omega_2 - \omega_2\gamma_{Kerr}\left(\left|a_{f,2}\right|^2 + a_{f,2}^{*}\varepsilon_{a,2}(t) + a_{f,2}\varepsilon_{a,2}^{*}(t)\right)\right] - \frac{1}{\tau_{ph,2}}\right)\left(a_{f,2}+\varepsilon_{a,2}(t)\right) \\ &- j\mu_2\left(a_{f,1}+\varepsilon_{a,1}(t)\right)\end{aligned} \tag{3.4.b}$$

Keeping only the first-order perturbation terms, we obtain the following coupled linear equations describing the dynamics of the perturbations:

$$\frac{d\varepsilon_{a,1}(t)}{dt} = \left(j\left[\Delta\omega_1 - 2\omega_1\gamma_{Kerr}\left|a_{f,1}\right|^2\right] - \frac{1}{\tau_{ph,1}}\right)\varepsilon_{a,1}(t) - j\omega_1\gamma_{Kerr}a_{f,1}^2\varepsilon_{a,1}^{*}(t) - j\mu_2\varepsilon_{a,2}(t) \tag{3.5.a}$$

$$\frac{d\varepsilon_{a,2}(t)}{dt} = \left(j\left[\Delta\omega_2 - 2\omega_2\gamma_{Kerr}\left|a_{f,2}\right|^2\right] - \frac{1}{\tau_{ph,2}}\right)\varepsilon_{a,2}(t) - j\omega_2\gamma_{Kerr}a_{f,2}^2\varepsilon_{a,2}^{*}(t) - j\mu_2\varepsilon_{a,1}(t) \tag{3.5.b}$$

Equations (3.5) and their complex conjugates form the dynamic system, $d\boldsymbol{\varepsilon}/dt = \mathbf{J}\boldsymbol{\varepsilon}$, with $\boldsymbol{\varepsilon} = \left[\varepsilon_{a,1}, \varepsilon_{a,1}^{*}, \varepsilon_{b,1}, \varepsilon_{b,1}^{*}\right]^T$ and the Jacobian matrix

$$\mathbf{J} = \begin{bmatrix} x_1 & y_1 & -j\mu_2 & 0 \\ y_1^{*} & x_1^{*} & 0 & j\mu_2 \\ -j\mu_2 & 0 & x_2 & y_2 \\ 0 & j\mu_2 & y_2^{*} & x_2^{*} \end{bmatrix} \tag{3.6}$$

with x_i and y_i given by

$$x_i = j\left[\Delta\omega_i - 2\omega_i\gamma_{Kerr}\left|a_{f,i}\right|^2\right] - \frac{1}{\tau_{ph,i}}; \tag{3.7.a}$$

$$y_i = -j\omega_i\gamma_{Kerr}a_{f,i}^2 \tag{3.7.b}$$

The eigenvalues of the above Jacobian matrix determine the dynamic behaviour of the system. Since the eigenvalues are the roots of a fourth-order polynomial, solutions cannot be obtained analytically but must be found by an iterative numerical method. This also means that we cannot analytically determine the thresholds for the different instability regions. Instead, we will provide a numerical analysis in Section 3.1.3.

3.1.1 Power-Space Coupling model (PC method)

We first consider the CMRR device in figure 3.1 in the absence of nonlinearity. By writing the equations relating the fields propagating inside microrings 1 and 2 and the input field, we obtain the following coupled delay equations:

$$A_1(t+T_{rt}) = a_{rt}\tau_{cp,1}\tau_{cp,2}A_1(t)e^{-j\Delta\varphi_{L,1}} - j\kappa_2 a_{rt}\tau_{cp,1}A_2(t)e^{-j\frac{\Delta\varphi_{L,1}+\Delta\varphi_{L,2}}{2}} - j\kappa_1 E_{in}(t+T_{rt}) \tag{3.8.a}$$

$$A_2(t+T_{rt}) = -j\kappa_2 a_{rt}A_1(t)e^{-j\frac{\Delta\varphi_{L,1}+\Delta\varphi_{L,2}}{2}} + a_{rt}\tau_{cp,2}A_2(t)e^{-j\Delta\varphi_{L,2}} \tag{3.8.b}$$

In the above equation, $\tau_{cp,1} = (1-\kappa_1^2)^{1/2}$ and $\tau_{cp,2} = (1-\kappa_2^2)^{1/2}$ are the field transmission coefficients of the coupling junctions, and $\Delta\varphi_{L,1} = \Delta\varphi_{L,2} = 2\pi R n_g K_0$ is the linear roundtrip phase of the microrings. In the presence of instantaneous Kerr nonlinearity, the roundtrip phase in each microring acquires an addition nonlinear term given by $\varphi_{NL,i} = 2\pi R n_2 |A_i(t)|^2 K_0$. Equations (3.8.a) and (3.8.b) are thus modified as

$$A_1(t+T_{rt}) = a_{rt}\tau_{cp,1}\tau_{cp,2}A_1(t)e^{-j(\Delta\varphi_{L,1}+\varphi_{NL,1}(t))} - j\kappa_2 a_{rt}\tau_{cp,1}A_2(t)e^{-j\frac{\Delta\varphi_{L,1}+\varphi_{NL,1}(t)+\Delta\varphi_{L,2}+\varphi_{NL,2}(t)}{2}} - j\kappa_1 E_{in}(t+T_{rt}) \quad (3.9.a)$$

$$A_2(t+T_{rt}) = -j\kappa_2 a_{rt}A_1(t)e^{-j\frac{\Delta\varphi_{L,1}+\varphi_{NL,1}(t)+\Delta\varphi_{L,2}+\varphi_{NL,2}(t)}{2}} + a_{rt}\tau_{cp,2}A_2(t)e^{-j(\Delta\varphi_{L,2}+\varphi_{NL,2}(t))} \quad (3.9.b)$$

The above equations form a system of coupled nonlinear delay equations describing the nonlinear dynamics of the CMRR. The stationary states of the system are obtained by setting $A_1(t+T_{rt}) = A_1(t) = A_{f,1}$ and $A_2(t+T_{rt}) = A_2(t) = A_{f,2}$ and solving for $A_{f,1}$ and $A_{f,2}$ to get

$$A_{f,1} = \frac{A_{f,2}\left(1 - a_{rt}\tau_{cp,2}e^{-j\varphi_{f,2}}\right)}{-j\kappa_2 a_{rt}e^{-j\frac{\varphi_{f,1}+\varphi_{f,2}}{2}}} \quad (3.10.a)$$

$$E_{in} = \frac{A_{f,1}\left(1 - a_{rt}\tau_{cp,1}\tau_{cp,2}e^{-j\varphi_{f,1}}\right) + j\kappa_2\tau_{cp,2}A_{f,2}e^{-j\frac{\varphi_{f,1}+\varphi_{f,2}}{2}}}{-j\kappa_1} \quad (3.10.b)$$

In the above equations, $\varphi_{f,i} = \Delta\varphi_{L,i} + \xi_{Kerr}|A_{f,i}|^2$ is the total phase shift corresponding to the stationary field $A_{f,i}$. To determine the stability of the CMRR around a stationary state, we write the fields in the microrings as $A_1(t) = A_{f,1} + \varepsilon_{A,1}(t)$ and $A_2(t) = A_{f,2} + \varepsilon_{A,2}(t)$, where $\varepsilon_{A,1}(t)$ and $\varepsilon_{A,2}(t)$ represent small perturbations. By substituting these expressions into equations (3.9.a) and (3.9.b) and linearizing around the stationary point, we obtain

$$\begin{aligned}\varepsilon_{A,1}(t+T_{rt}) &= a_{rt}\tau_{cp,1}\tau_{cp,2}e^{-j\varphi_{f,1}}\left(\left(1 - j\xi_{kerr}\left|A_{f,1}\right|^2\right)\varepsilon_{a,1} - j\xi_{kerr}A_{f,1}^2\varepsilon_{a,1}^*\right) \\ &- j\kappa_2 a_{rt}\tau_{cp,1}e^{-j\frac{\varphi_{f,1}+\varphi_{f,2}}{2}}\left(1 - j\frac{\xi_{kerr}}{2}\left|A_{f,2}\right|^2\right)\varepsilon_{a,2} \\ &- j\kappa_2 a_{rt}\tau_{cp,1}e^{-j\frac{\varphi_{f,1}+\varphi_{f,2}}{2}} \times -j\xi_{kerr}\frac{A_{f,1}A_{f,2}\varepsilon_{a,1}^* + A_{2,f}A_{f,1}^*\varepsilon_{a,1} + A_{f,2}^2\varepsilon_{a,2}^*}{2}\end{aligned} \quad (3.11.a)$$

$$\varepsilon_{A,2}(t+T_{rt}) = a_{rt}\tau_{cp,2}e^{-j\varphi_{f,2}}\left(\left(1-j\xi_{kerr}\left|A_{f,2}\right|^2\right)\varepsilon_{a,2} - j\xi_{kerr}A_{f,2}^2\varepsilon_{a,2}^*\right)$$
$$- j\kappa_2 a_{rt}e^{-j\frac{\varphi_{f,1}+\varphi_{f,2}}{2}}\left(1-j\frac{\xi_{kerr}}{2}\left|A_{f,1}\right|^2\right)\varepsilon_{a,1} \qquad (3.11.b)$$
$$- j\kappa_2 a_{rt}e^{-j\frac{\varphi_{f,1}+\varphi_{f,2}}{2}} \times\left(-j\xi_{kerr}\frac{A_{f,1}^2\varepsilon_{a,1}^* + A_{f,1}A_{f,2}^*\varepsilon_{a,2} + A_{f,1}A_{f,2}\varepsilon_{a,2}^*}{2}\right)$$

The above equations and their complex conjugates form a linear time-delay system, which can be expressed in matrix form as

$$\begin{bmatrix}\varepsilon_{A,1}(t+T_{rt})\\ \varepsilon_{A,1}^*(t+T_{rt})\\ \varepsilon_{A,2}(t+T_{rt})\\ \varepsilon_{A,2}^*(t+T_{rt})\end{bmatrix} = \mathbf{J}\begin{bmatrix}\varepsilon_{A,1}(t)\\ \varepsilon_{A,1}^*(t)\\ \varepsilon_{A,2}(t)\\ \varepsilon_{A,2}^*(t)\end{bmatrix} \qquad (3.12)$$

where **J** is the Jacobian matrix of the system. Solutions of the above linear system have the form $\boldsymbol{\varepsilon}(t + T_{rt}) = z\,\boldsymbol{\varepsilon}(t)$, where $z = e^{sTrt}$ is an eigenvalue of the Jacobian matrix **J**. Thus, the locations of the eigenvalues in the z-plane determine the stability behavior of the CMRR. More specifically, if all the eigenvalues have magnitude less than unity, the optical fields inside the CMRR are stable. Otherwise, the system exhibits instabilities such as BS, SP, and Ikeda. In section 2.1.2 we discussed in detail the dynamic behaviors corresponding to the different locations of the eigenvalues in the z-space.

3.1.2 Simulation Results and Discussion

To compare the nonlinear dynamics of a double CMRR predicted by the EC and PC models, we use the example of a CMRR device with chalcogenide glass as the core waveguide material because of its high Kerr coefficient and the absence of FC effects [79]. The dimensions and the linear and nonlinear material parameters of the

chalcogenide waveguide are the same as in section 2.1.3. The microrings have radius $R_1 = R_2 = 100$ μm. Since the EC model is valid only for weak couplings, we choose a small coupling coefficient of $\kappa_1^2 = \kappa_2^2 = 1\%$ for both the ring-to-bus coupling and ring-to-ring coupling.

Figures 3.2(a) and (b) show the stability phase maps of the device obtained from the EC and PC models, respectively. The maps show the regions of stable behavior (blue), BS (yellow), SP (azure) and Ikeda instability (brown) as functions of the linear phase detune ($\Delta\varphi_{L,1} = \Delta\varphi_{L,2}$) and the power in microring 2 ($P_{a,2}$). The corresponding input power P_{in} and the power in microring 1 ($P_{a,1}$) can be computed from $P_{a,2}$ using equations (3.10.a) and (3.10.b), respectively. Comparison between the EC and PC stability phase maps shows that the PC model predicts much richer nonlinear dynamics in the CMRR than the EC model. The most obvious difference is that the PC phase map exhibits multiple BS regions. In addition, the EC model fails to predict Ikeda instability (period doubling) and high-order instability because it models only one resonance mode for each MRR. On the other hand, the PC model shows that Ikeda instability can occur in a CMRR. To our knowledge, this is the first time period doubling oscillation is predicted to also occur in a system of coupled resonators.

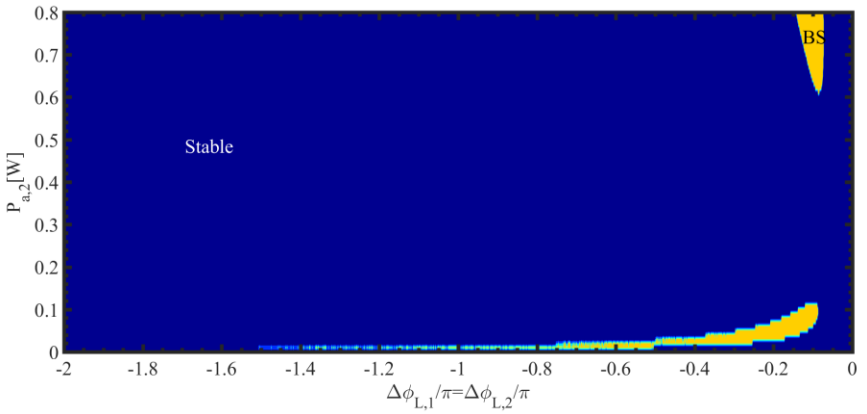

(a)

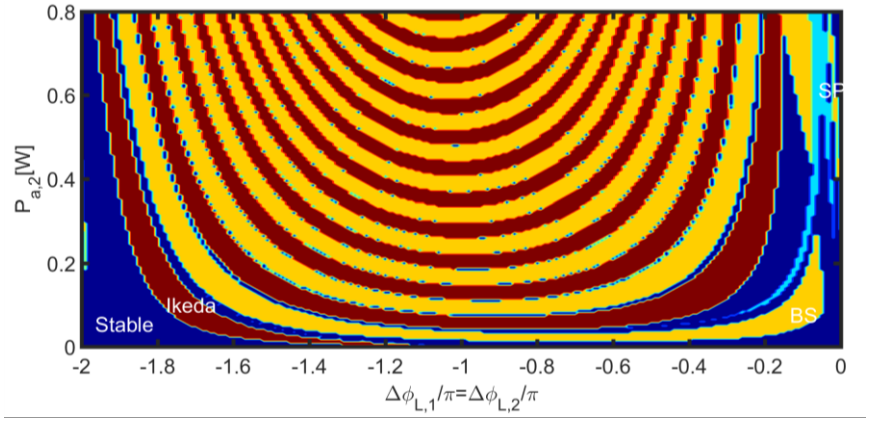

(b)

Figure 3.2,The Stability phase map as a function of the stored power inside a weakly coupled CMRR and linear phase detune for (a) EC and (b) PC models

It is of interest to compare the threshold power for observing Ikeda instability in a single MRR and a double CMRR. Figure 3.3 plots the Ikeda threshold power as a function of the linear phase detune for each device. We see that the threshold power is generally higher for the CMRR than the single MRR. This may be explained in terms of the linear resonance spectrum of the CMRR. Figure 3.4 shows the resonance spectra of the powers in both microrings 1 and 2 of the CMRR. We observe that the mode in each resonator experiences splitting due to coupling between the two resonators. This resonance splitting has the effect of lowering the peak stored power in each microring, which degrades the

efficiency of the four-wave mixing process of adjacent cavity modes that is responsible for the period-doubling oscillations. We also note from figure 3.3 that the threshold powers required to observe Ikeda instability in the CMRR are in the order of a few Watts, which is too high for practical chalcogenide devices. Another interesting observation from the phase maps in figure 3.2 that both the EC and PC models predict that SP can also occur in the CMRR. This is a significant difference compared to a single MRR with instantaneous nonlinearity, where both the EC and PC model show that SP cannot occur [14].

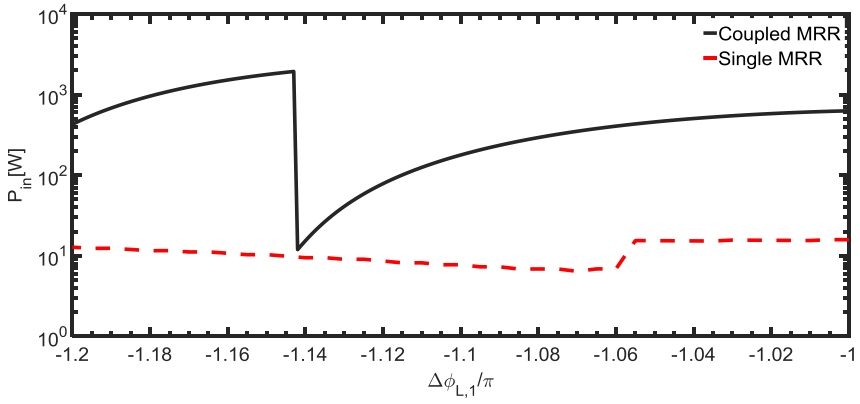

Figure 3.3, The threshold power of Ikeda instability vs linear phase detune for a single MRR and a double CMRR

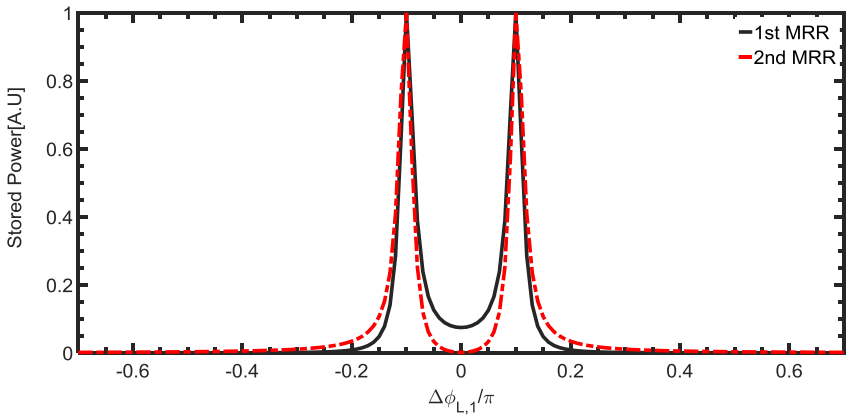

Figure 3.4, Resonance spectra of the powers in microrings 1 and 2 of the CMRR

In the CMRR, SP arises from the beating between the resonance modes of the two microrings [36], as opposed to Ikeda instability, which arises from the beating between two adjacent resonance modes of the same cavity. It is also interesting to compare the threshold power for observing SP with that required for Ikeda instability. Figure 3.5 shows the plot of the SP threshold power as a function of the linear phase detune. We see that SP can be observed with a power level as low as 130 mW (at linear phase detune around -0.46π), which can be handled by practical chalcogenide devices.

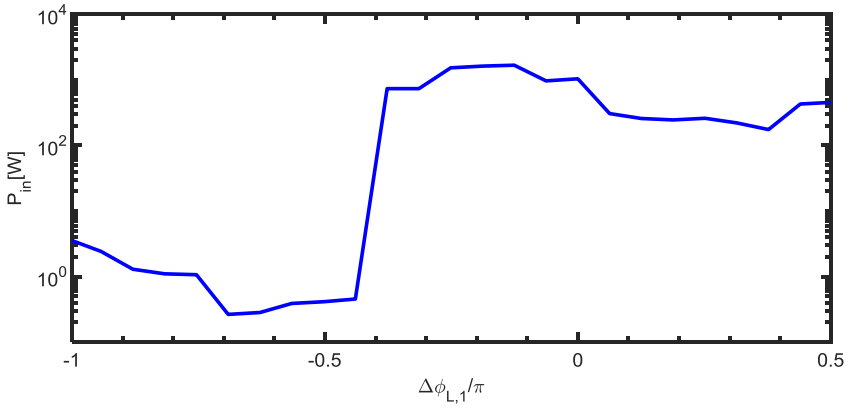

Figure 3.5, The Threshold power of SP vs. Linear phase detune

3.2 Instability in CMRRs with Non-Instantaneous Nonlinearity

In this section we extend the EC model to study the nonlinear dynamic behavior of a double CMRR with non-instantaneous nonlinearity. We are interested in CMRRs made of silicon due to its wide spread use in integrated photonics [87] and its strong FC induced nonlinearity. However, since the nonlinearity depends on the FC density, it has a finite relaxation time determined by the FC lifetime in the silicon waveguide.

For a system of two couple MRRs as depicted in figure 3.1, we can modify the EC equations (3.1.a) and (3.1.b) to include the nonlinear resonant frequency shift in each

MRR due to FCD as follows:

$$\frac{da_1(t)}{dt} = \left(j\left(\Delta\omega_1 - \frac{\omega_1}{n_g}\sigma_{FCD}N_1(t) \right) - \frac{1}{\tau_{ph,1}} \right) a_1(t) - j\mu_1\sqrt{P_{in}(t)} - j\mu_2 a_2(t) \tag{3.13.a}$$

$$\frac{da_2(t)}{dt} = \left(j\left(\Delta\omega_2 - \frac{\omega_2}{n_g}\sigma_{FCD}N_2(t) \right) - \frac{1}{\tau_{ph,2}} \right) a_2(t) - j\mu_2 a_1(t) \tag{3.13.b}$$

The FC densities $N_1(t)$ and $N_2(t)$ in microrings 1 and 2 satisfy the rate equations:

$$\frac{dN_1(t)}{dt} = \frac{\beta_{TPA}}{2\hbar\omega_1}\left(\frac{|a_1(t)|^2}{A_{eff}T_{rt}} \right)^2 - \frac{N_1(t)}{\tau_{fc}} \tag{3.13.c}$$

$$\frac{dN_2(t)}{dt} = \frac{\beta_{TPA}}{2\hbar\omega_1}\left(\frac{|a_2(t)|^2}{A_{eff}T_{rt}} \right)^2 - \frac{N_2(t)}{\tau_{fc}} \tag{3.13.d}$$

Equations (3.13) form a nonlinear dynamic system. To perform stability analysis of the system, we introduce small perturbations to the variables, $a_1(t) = a_{f,1} + \varepsilon_{a,1}(t)$, $a_2(t) = a_{f,2} + \varepsilon_{a,2}(t)$, $N_1(t) = N_{f,1} + \varepsilon_{N,1}(t)$, $N_2(t) = N_{f,2} + \varepsilon_{N,2}(t)$. The quantities $a_{f,1}$, $a_{f,2}$, $N_{f,1}$ and $N_{f,2}$ are steady state solutions of equations (3.13),

$$a_{1,f} = \frac{\left(\left(\Delta\omega_2 - \frac{\omega_2}{n_g}\sigma_{FCD}N_{f,2} \right) + \frac{j}{\tau_{ph,2}} \right)}{\mu_2} a_{f,2} \tag{3.14.a}$$

$$P_{in} = \left| \frac{\left(\left(\Delta\omega_1 - \frac{\omega_1}{n_g}\sigma_{FCD}N_{f,1} \right) + \frac{j}{\tau_{ph,1}} \right) a_{f,1} - \mu_2 a_{f,2}}{\mu_1} \right|^2 \tag{3.14.b}$$

$$N_{f,1} = \frac{\beta_{TPA}}{2\hbar\omega_1}\left(\frac{\left|a_{f,1}\right|^2}{A_{eff}T_{rt}}\right)^2 \tau_{fc} \tag{3.14.c}$$

$$N_{f,2} = \frac{\beta_{TPA}}{2\hbar\omega_1}\left(\frac{\left|a_{f,2}\right|^2}{A_{eff}T_{rt}}\right)^2 \tau_{fc} \tag{3.14.d}$$

Substituting these expressions into equations (3.13) and separating the steady state solutions from the linearized perturbation terms, we get

$$\frac{d\varepsilon_{a,1}(t)}{dt} = \left(j\left(\Delta\omega_1 - \frac{\omega_1}{n_g}\sigma_{FCD}N_{f,1}\right) - \frac{1}{\tau_{ph,1}}\right)\varepsilon_{a,1}(t) - j\frac{\omega_1}{n_g}\sigma_{FCD}a_{f,1}\varepsilon_{N,1}(t) - j\mu_2\varepsilon_{a,2}(t) \tag{3.15.a}$$

$$\frac{d\varepsilon_{a,2}(t)}{dt} = \left(j\left(\Delta\omega_2 - \frac{\omega_2}{n_g}\sigma_{FCD}N_{f,2}\right) - \frac{1}{\tau_{ph,2}}\right)\varepsilon_{a,2}(t) - j\frac{\omega_2}{n_g}\sigma_{FCD}a_{f,2}\varepsilon_{N,2}(t) - j\mu_2\varepsilon_{a,1}(t) \tag{3.15.b}$$

$$\frac{d\varepsilon_{N,1}(t)}{dt} = \frac{\beta_{TPA}}{2\hbar\omega_1}\left(\frac{2\left|a_{f,1}\right|^2\left(a_{f,1}^*\varepsilon_{a,1}(t) + a_{f,1}\varepsilon_{a,1}^*(t)\right)}{\left(A_{eff}T_{rt}\right)^2}\right) - \frac{\varepsilon_{N,1}(t)}{\tau_{fc}} \tag{3.15.c}$$

$$\frac{d\varepsilon_{N,2}(t)}{dt} = \frac{\beta_{TPA}}{2\hbar\omega_2}\left(\frac{2\left|a_{f,2}\right|^2\left(a_{f,2}^*\varepsilon_{a,2}(t) + a_{f,2}\varepsilon_{a,2}^*(t)\right)}{\left(A_{eff}T_{rt}\right)^2}\right) - \frac{\varepsilon_{N,2}(t)}{\tau_{fc}} \tag{3.15.d}$$

The above equations can be put in matrix form as

$$\frac{d}{dt}\begin{bmatrix}\varepsilon_{a,1}\\ \varepsilon_{a,1}^*\\ \varepsilon_{a,2}\\ \varepsilon_{a,2}^*\\ \varepsilon_{N,1}\\ \varepsilon_{N,2}^*\end{bmatrix} = \mathbf{J}\begin{bmatrix}\varepsilon_{a,1}\\ \varepsilon_{a,1}^*\\ \varepsilon_{a,2}\\ \varepsilon_{a,2}^*\\ \varepsilon_{N,1}\\ \varepsilon_{N,2}^*\end{bmatrix} \tag{3.16}$$

where **J** is the Jacobian matrix of the system. As before, the eigenvalues of the Jacobian determine the dynamic behavior of the stored energies and the FC densities in the CMRR.

We apply the above analysis to a silicon CMRR with the parameters shown in Table 2.1. The power coupling coefficients are chosen to be κ_1^2 = 16% and κ_2^2 = 1%, which correspond to energy coupling coefficients $\mu_1 = 1.3619\times10^5$ [$Hz^{0.5}$] and $\mu_2 = 1.1592\times10^{10}$ [Hz]. We assume the FC lifetime in the silicon waveguide to be τ_{fc} = 1 ns. Figure 3.6 shows the stability phase map of the CMRR as a function of the linear phase detune and the power in microring 2 ($P_{a,2}$). The regions of stable behavior, BS and SP are represented by the colors blue, yellow and azure, respectively. We observe that there are two separate BS regions, implying that multi-stability occurs in the device due to the existence of two resonance modes in the system. To study the influence of the FC lifetime on the SP behavior of the CMRR, we show in figure 3.7 the stability phase map as a function of the normalized FC lifetime (τ_{fc}/ T_{rt}) and the stored power in microring 2 for a specific phase detune of 0.1π.

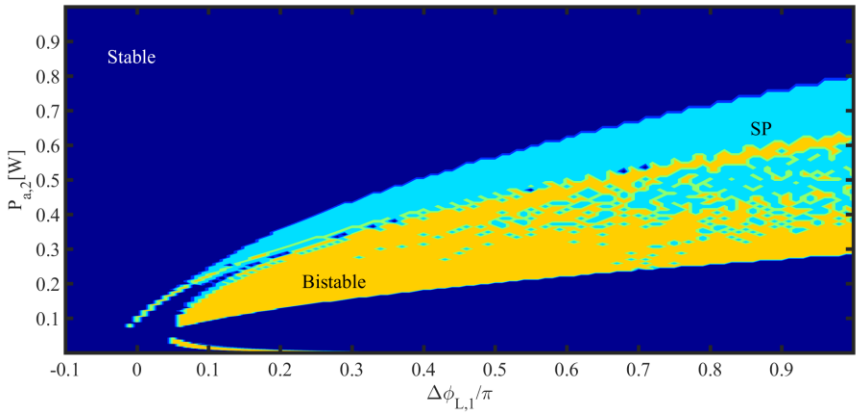

Figure 3.6, Stability phase map of Silicon CMRR with τ_{fc} of 1 ns as a function of linear phase detune and stored power in 2nd MRR

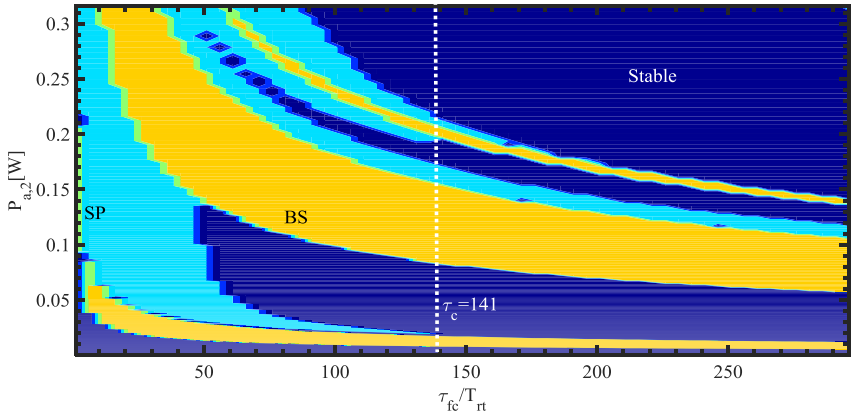

Figure 3.7, Stability map for linear phase detune .1π as a function of stored power in microring 2 and the normalized free carrier lifetime

We observe that similar to SP in a single MRR, there exists an upper limit to the FC lifetime for which SP in the CMRR can take place. For example, for the first-order instability (lowest branch in the stability map) the critical FC lifetime value is $141T_{rt}$ (1.15 ns for 100 μm MRR), as indicated in figure 3.7.

In figure 3.8 we plot the critical FC lifetime as a function of the linear phase detune. Also shown for comparison is the critical FC lifetime for observing SP in a single silicon MRR. We observe that the critical FC lifetime for the CMRR is reduced by about 164ps compared to that of the single MRR, implying that the nonlinear relaxation time places a more restrict constraint on SP in the CMRR. In addition, we observe that SP can also occur at higher powers and larger FC lifetime values. These instabilities are absent in a single MRR and can be attributed to the mutual interactions of the two resonance modes in the CMRR.

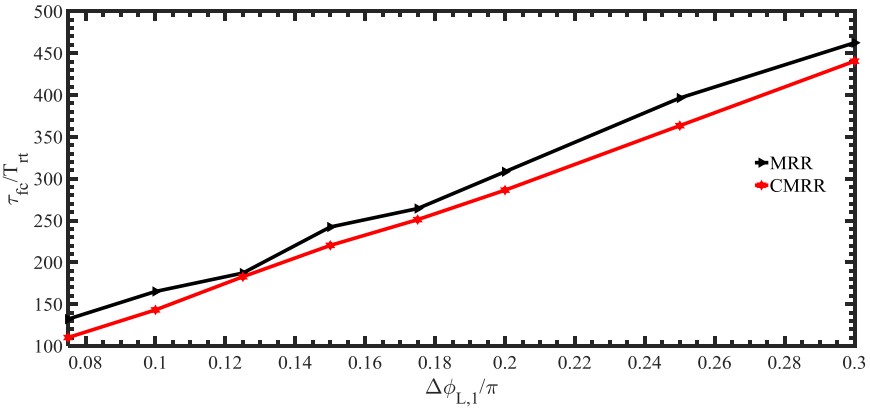

Figure 3.8, Critical FC lifetime vs. linear phase detune for SP in a single MRR and a double CMRR

Figure 3.9 compares the input threshold powers required to reach SP in a single MRR and a double CMRR as a function of the linear phase detune for the critical FC lifetime reported in figure 3.8. It is seen that the CMRR has a higher threshold power, which is due to the fact that the power is distributed over two resonators so that the nonlinear interactions are weaker for the same input power as in a single MRR. Also, the threshold power generally decreases at larger linear phase detunes because of increasing the critical carrier lifetime.

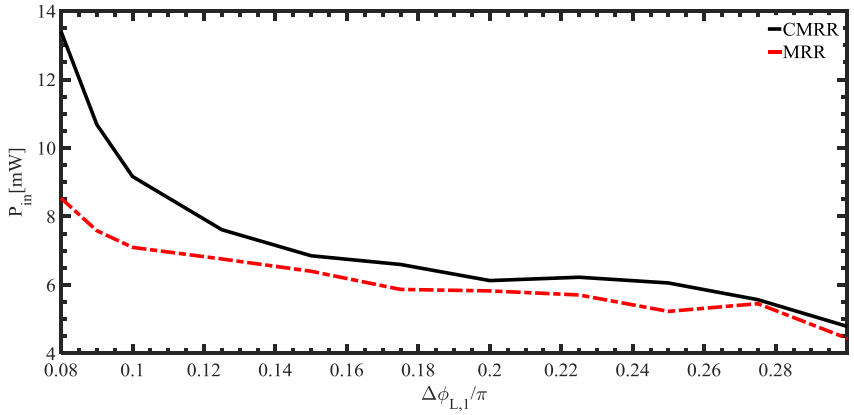

Figure 3.9, Input threshold power for SP vs linear phase detune for single MRR and double CMRR

Finally we compare in figure 3.10 the SP period as a function of the linear phase detune for a single MRR and a double CMRR. The FC lifetime is set at the critical lifetime

value reported in figure 3.8 for each linear phase detune. We see that compared to the singel MRR, the SP period in the CMRR can be varied over a wider range, from 5.3 GHz to 21 GHz, by tuning the linear phase.

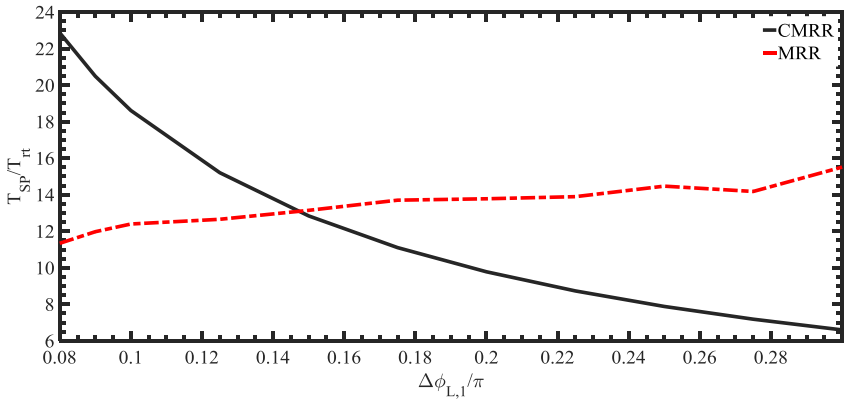

Figure 3.10, SP period vs the linear phase detunes for single MRR and double CMRR

This large variation in the period of oscillation may be associated with the nonlinear beating between splitted frequency components generated by coupling between the microrings. From the above analysis, we conclude that a double CMRR requires higher input power to observe SP than a single MRR and slightly more constrained by the FC lifetime, it does allow for a larger range of oscillation frequencies to be achieved.

3.3 Matrix formalism for CMRRs with Instantaneous Nonlinearity

In section 3.1, we showed that a double CMRR with instantaneous Kerr nonlinearity, SP can occur due to the beating of the resonance modes of the two microrings [36, 86]. By further increasing the number of resonators to form a chain of coupled MRRs, we may expect to observe more complex nonlinear dynamic behaviours. In addition to the emergence of new nonlinear dynamics, it may also be possible to achieve a reduction in the threshold power for observing SP in a chain of CMRRs due to the increased nonlinear

interaction length.

A chain of CMRRs is also called a Coupled Ring Oscillator Waveguide (CROW), which was originally proposed by A. Yariv in 1999 for achieving slow light propagation and dispersion engineering in the linear regime [56]. In this section, we will develop general transfer matrix formalisms based on the EC and PC models for analyzing the dynamic behaviors of the propagating fields in a CROW structure with instantaneous Kerr nonlinearity. These formalisms will allow us to study the instability of spatially extended networks with finite lengths, which will be compared to the nonlinear dynamics of infinite extended networks in chapter 4.

In developing a general matrix formalism for the nonlinear dynamics of a CROW structure of length N_z (N_z being the number of resonators in the chain), we found that it is convenient to first obtain the matrix equation for a unit cell consisting of three coupled MRRs, as shown in figure 3.11. The result is then generalized for a CROW waveguide of arbitrary length N_z.

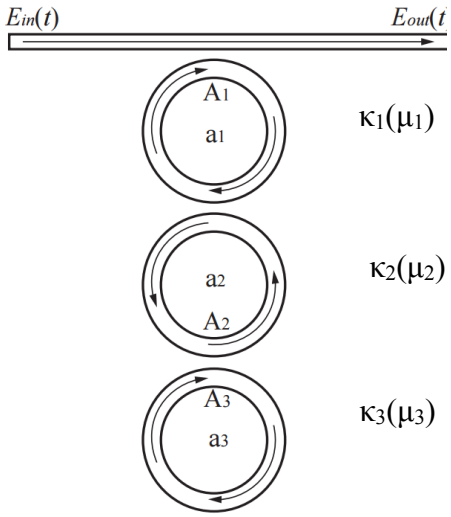

Figure 3.11, Structure of three coupled MRRs

In the chain of three CMRRs in figure 3.11, we denote κ_i (μ_i) as the field (energy) coupling coefficient between microring i and i – 1 (i = 0 being the bus waveguide). The optical wave inside microring i is represented by a_i in the EC model and A_i in the PC model, which are normalized such that $|a_i|^2$ and $|A_i|^2$ give the energy and power, respectively, in the microring.

3.3.1 The EC model

The equations for the time evolution of the waves in the three CMRRs in the presence of Kerr nonlinearity can be written in matrix form as follows:

$$\frac{d\mathbf{a}(t)}{dt} = \left(\mathbf{M}_{E\_L} + \mathbf{M}_{E\_NL}\right)\mathbf{a}(t) + \mathbf{S}(t) \tag{3.17}$$

where $\mathbf{a}(t)$ is the wave amplitude array, $\mathbf{M}_{E\_L}$ is the linear coupling matrix, $\mathbf{M}_{E\_NL}$ is the nonlinear coupling matrix and $\mathbf{S}$ represents the input excitation. These variables are written explicitly as follows:

$$\mathbf{a}(t) = \left[a_1(t) \quad a_2(t) \quad a_3(t)\right]^T \tag{3.18.a}$$

$$\mathbf{M}_{E\_L} = \mathrm{diag}\begin{bmatrix} j\Delta\omega_{L,1} - \dfrac{1}{\tau_{ph,1}} \\ j\Delta\omega_{L,2} - \dfrac{1}{\tau_{ph,2}} \\ j\Delta\omega_{L,3} - \dfrac{1}{\tau_{ph,3}} \end{bmatrix} \tag{3.18.b}$$

$$\mathbf{M}_{E\_NL} = -j\gamma_{kerr}[\omega]\mathrm{diag}\left[|a(t)|^2\right] \tag{3.18.c}$$

$$\mathbf{S}(t) = \left[-j\mu_1\sqrt{P_{in}(t)} \quad 0 \quad 0\right]^T \tag{3.18.d}$$

Kerr coefficient strength is $\gamma_{Kerr} = n_2(n_g A_{eff} T_{rt})^{-1}$. Equation (3.17) describes the nonlinear dynamics of a CROW structure consisting of three CMRRs. The system can be easily generalized to a CROW of length N_z by observing the patterns exhibited by the matrices in (3.18).

For the general CROW structure, we obtain the stationary solution $\mathbf{a_f}$ by setting the time derivative d$\mathbf{a}$/dt to zero, which yields the matrix equation

$$\left[\mathbf{M}_{E\_L} + \mathbf{M}_{E\_NL}\right]\mathbf{a}_f = -\mathbf{S} \tag{3.19}$$

Next we perturb the solution around the stationary point, $\mathbf{a}(t) = \mathbf{a_f} + \boldsymbol{\varepsilon_a}(t)$, where $\boldsymbol{\varepsilon} = [\varepsilon_{a,1}, \varepsilon_{a,2}, \varepsilon_{a,3}]^T$. Substituting into equation (3.17) and keeping only the first-order perturbation terms, we get

$$\frac{d\boldsymbol{\varepsilon}_a(t)}{dt} = \left(\mathbf{M}_{E\_L} + 2\mathbf{M}_{E\_NL}\right)\boldsymbol{\varepsilon}_a(t) - j\gamma_{kerr}[\omega]\mathbf{a}_f^2\boldsymbol{\varepsilon}_a^*(t) \tag{3.20}$$

The Jacobian matrix of the above linear system has the form

$$\mathbf{J} = \begin{bmatrix} \mathbf{M}_{E_L} + \mathbf{M}_{E_{NL}} & -j\gamma_{kerr}[\omega]\mathbf{a}_f^2 \\ j\gamma_{kerr}[\omega]\mathbf{a}_f^{*2} & \mathbf{M}_{E_L}^* + \mathbf{M}_{E_{NL}}^* \end{bmatrix} \tag{3.21}$$

The eigenvalues of the Jacobian matrix determine the stability behaviour of the nonlinear CROW structure.

3.3.2 The PC Model

For a CROW structure with three CMRRs, the fields inside the microrings are updated after each roundtrip by the following matrix equation:

$$\mathbf{A}(t+T_{rt}) = \mathbf{H}\mathbf{A}(t) + \mathbf{S}(t) \tag{3.22}$$

In the above equation, the microring field array **A**, the applied field array **S** and the coupling matrix **H** are given by

$$\mathbf{A}(t) = \begin{bmatrix} A_1(t) & A_2(t) & A_3(t) \end{bmatrix}^T \tag{3.23.a}$$

$$\mathbf{S}(t) = \begin{bmatrix} -j\kappa_1 E_{in}(t) & 0 & 0 \end{bmatrix}^T \tag{3.23.b}$$

$$\mathbf{H} = a_{rt} \begin{bmatrix} \tau_{cp,1}\tau_{cp,2} e^{-j\varphi_{f,1}} & -j\kappa_2 \tau_{cp,1} e^{-j\frac{\varphi_{f,1}+\varphi_{f,2}}{2}} & 0 \\ -j\kappa_2 \tau_{cp,3} e^{-j\frac{\varphi_{f,1}+\varphi_{f,2}}{2}} & \tau_{cp,2}\tau_{cp,3} e^{-j\varphi_{f,2}} & -j\kappa_3 \tau_{cp,3} e^{-j\varphi_{f,3}} \\ 0 & -j\kappa_3 \tau_{cp,2} e^{-j\varphi_{f,2}} & \tau_{cp,3}\tau_{cp,3} e^{-j\varphi_{f,3}} \end{bmatrix} \tag{3.23.c}$$

In the above matrix equation, τ_{cp1}, $\varphi_{f,1}$ are transmission coefficient and steady state phase shift in 1st MRR. This induced phase shift consists of linear and nonlinear parts.

We can further decompose **H** into a coupling matrix $\mathbf{K}_{coupling}$ and a phase detune **Λ** in the form $\mathbf{H} = \mathbf{\Lambda}\mathbf{K}_{coupling}\mathbf{\Lambda}$, where $\mathbf{K}_{coupling}$ and **Λ** are defined as follows:

$$\mathbf{\Lambda} = \mathrm{Diag}\begin{bmatrix} e^{-j\frac{\varphi_{f,1}}{2}} \\ e^{-j\frac{\varphi_{f,2}}{2}} \\ e^{-j\frac{\varphi_{f,3}}{2}} \end{bmatrix} \tag{3.24.a}$$

$$\mathbf{K}_{Coupling} = a_{rt} \begin{bmatrix} \tau_{cp,1}\tau_{cp,2} & -j\kappa_2 \tau_{cp,1} & 0 \\ -j\kappa_2 \tau_{cp,3} & \tau_{cp,2}\tau_{cp,3} & -j\kappa_3 \tau_{cp,3} \\ 0 & -j\kappa_3 \tau_{cp,2} & \tau_{cp,3}^2 \end{bmatrix} \tag{3.24.b}$$

In order to express **H** in the form $\mathbf{H} = \mathbf{\Lambda K}_{coupling}\mathbf{\Lambda}$, we note that the phase delay between the second and the third MRR (or vice versa) in the matrix **H** in equation (3.23.c) is $\varphi_{f,3}$ (or $\varphi_{f,2}$) while the same element in the matrix $\mathbf{\Lambda K}_{coupling}\mathbf{\Lambda}$ is $\frac{1}{2}(\varphi_{f,2}+\varphi_{f,3})$. We thus rewrite the phase detunes $\varphi_{f,3}$ and $\varphi_{f,2}$ as

$$\varphi_{f,3} = \frac{\varphi_{f,3}+\varphi_{f,2}}{2} + \frac{\varphi_{f,3}-\varphi_{f,2}}{2} = \frac{\varphi_{f,3}+\varphi_{f,2}}{2} + \frac{\Delta\Theta_3}{2} \tag{3.25.a}$$

$$\varphi_{f,2} = \frac{\varphi_{f,3}+\varphi_{f,2}}{2} - \frac{\varphi_{f,3}-\varphi_{f,2}}{2} = \frac{\varphi_{f,3}+\varphi_{f,2}}{2} - \frac{\Delta\Theta_3}{2} = \frac{\varphi_{f,3}+\varphi_{f,2}}{2} + \frac{\Delta\Theta_2}{2} \tag{3.25.b}$$

Where $\Delta\Theta_2$ ($\Delta\Theta_3$) is the phase shift difference between 2nd (3rd) and 3rd(2nd) MRR. Because the nonlinear phase detune $\Delta\varphi_{NL,1}$ has a perturbative nature, we can ignore the nonlinear phase contribution in $\Delta\Theta_3$ to keep the formalism as simple as possible. Hence $\Delta\Theta_3$ consists of the linear phase detune of the 2nd and the 3rd MRRs. Based on the above definition we can write $\Delta\Theta_3=\Delta\varphi_{L,2}-\Delta\varphi_{L,3}$ and $\Delta\Theta_2=\Delta\varphi_{L,3}-\Delta\varphi_{L,2}$.

We could incorporate $\Delta\Theta_3$ into the $K_{coupling}$ matrix due to the linear nature of this term to form a new coupling matrix $K'_{coupling}$. Except for the elements (2, 3) and (3, 2) of $K'_{coupling}$, all the elements of $K_{coupling}$ and $K'_{coupling}$ are identical. The elements (2, 3) and (3, 2) of $K'_{coupling}$ have additional phase shifts of $-\frac{1}{2}\Delta\Theta_3$ and $-\frac{1}{2}\Delta\Theta_2$ ($=\frac{1}{2}\Delta\Theta_3$). By generalizing this modification to a CROW structure of length N_z, we found that this pattern is repeated between the $2i^{th}$ and $2i+1^{th}$ MRRs. We thus modify the different elements of the new coupling matrix $K'_{coupling}$ as follows:

$$K'_{coupling}(m,n) = K_{Coupling}(m,n)e^{-j\frac{\Delta\Theta_m}{2}} \quad \therefore \left\{(2i,2i+1)\text{or}(2i+1,2i)\big|_{i=1,2,3,\ldots}\right\} \tag{3.26}$$

The equation governing the field propagation in a nonlinear CROW waveguide is then

$A(t+T)= \mathbf{\Lambda K'}_{coupling}\mathbf{\Lambda}\, A(t)+S(t)$

The stationary solution A_f of the nonlinear system (3.22) is obtained by solving $(\mathbf{I} - \mathbf{H})\mathbf{A_f} = \mathbf{S}$. Applying perturbation to the stationary solution, $\mathbf{A}(t) = \mathbf{A_f} + \boldsymbol{\varepsilon_A}(t)$, and substituting it into equation (3.22), we obtain the following equation describing the evolution of the perturbation:

$$\boldsymbol{\varepsilon}_A(t+T_{rt}) = \left(\mathbf{H} - \frac{1}{2}j\xi_{kerr}\mathbf{P}_1\mathbf{A}_f^*\right)\boldsymbol{\varepsilon}_A(t) - \frac{1}{2}j\xi_{kerr}\mathbf{P}_2\mathbf{A}_f\boldsymbol{\varepsilon}_A^*(t) \tag{3.27}$$

where $\mathbf{P}_1 = \mathbf{\Lambda}(\mathbf{L}\mathbf{A}_f^*)\mathbf{\Lambda}$, $\mathbf{P}_2 = \mathbf{\Lambda}(\mathbf{L}\mathbf{A}_f)\mathbf{\Lambda}$, and $\mathbf{L}$ is a diagonal matrix given by

$$\mathbf{L} = \text{diag}(\mathbf{K'}_{coupling}\times\mathbf{A}_f) + \mathbf{K'}_{coupling}\times\mathbf{A}_f.$$

The dynamics of the perturbation are determined by the eigenvalues of the Jacobian matrix of equation (3.27), which is given by

$$\mathbf{J} = \begin{bmatrix} \mathbf{H} - \frac{1}{2}j\xi_{kerr}\mathbf{P}_1\mathbf{A}_f^* & -\frac{j}{2}\xi_{kerr}\mathbf{P}_2\mathbf{A}_f \\ \frac{j}{2}\left(\xi_{kerr}\mathbf{P}_2\mathbf{A}_f\right)^* & \left(\mathbf{H} - \frac{1}{2}j\xi_{kerr}\mathbf{P}_1\mathbf{A}_f^*\right)^* \end{bmatrix} \tag{3.28}$$

We apply the above matrix analysis to investigate the nonlinear dynamics in a chain of chalcogenide CMRRs of length N_z with instantaneous Kerr nonlinearity. The properties of CROW waveguide is listed in table 2.

Table 3.1, Parameters of the CROW waveguide

Parameter	Value	Dimension
Core material	Chalcogenide glass	N/A
Coupling coefficient	0.1	N/A
Waveguide cross-section dimension	320×500	nm×nm
Round trip loss	0.98	N/A
Kerr coefficient	11×10^{-18}	$m^2.W^{-1}$
Ring radius	100	μm

Figure 3.12 shows the plot of the threshold power for observing SP as a function of the length of the CMRR. Also shown in the plot is the linear phase detune where the SP occurs. We observe that as the CMRR length is increased, the threshold power decreases due to an increase in the nonlinear interaction length. However, for CMRR length greater than 4, the threshold power levels out and begins to increase slightly with N_z, which is attributed to decreased nonlinear interaction. Although the traveled path of the optical wave is getting longer by increasing the length of CROW waveguide, but the stored power in each ring exponentially decays in the direction of CROW waveguide which reduces the probability of nonlinear interaction between photons in the longer waveguide.

The plot shows that the minimum threshold power is achieved with a CMRR of length 4. This threshold power is around 35 mW, which is about three times lower than the threshold power in a coupled MRR. This example illustrates the advantage of a spatially extended CMRR chain over a single MRR for achieving instability.

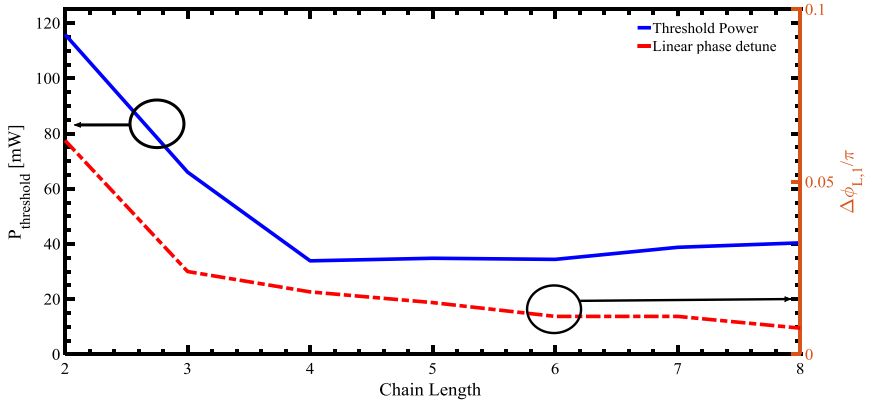

Figure 3.12, Threshold power for SP in a CMRR chain vs. the chain length

We also investigate the influence of the CMRR length on the threshold for Ikeda instability. The plot of Ikeda threshold vs. N_z is shown in figure 3.13. Here, we observe that the threshold power for reaching Ikeda instability also decreases with increasing CMRR length, as a result of increased nonlinear interaction length. However, the threshold power is in the range of Watts, which is too high for practical integrated photonic devices. Thus it is not feasible to observe Ikeda instability in a chain of CMRRs with instantaneous Kerr nonlinearity.

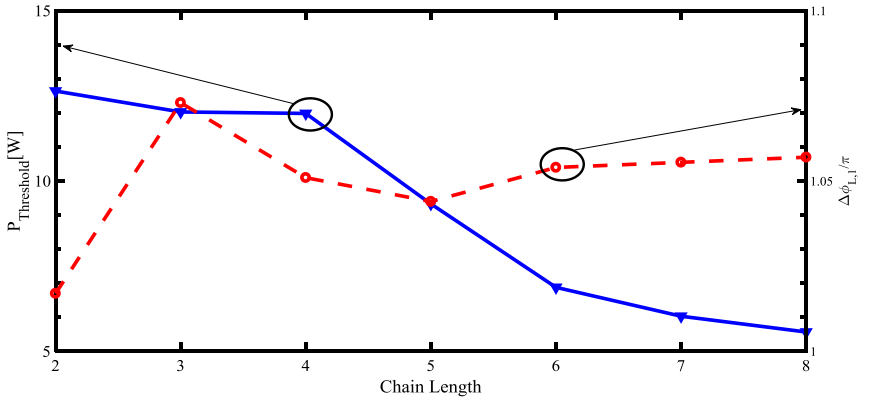

Figure 3.13, Ikeda Instability threshold power in a CMRR chain as a function of the chain length

3.4 Summary

In this chapter, we derived systems of nonlinear coupled equations to study the dynamic behaviors of double CMRR structures with instantaneous and non-instantaneous nonlinearities based on the EC and PC models. Both models predict that SP can occur in a double CMRR with instantaneous Kerr nonlinearity, a phenomenon which cannot occur in a single MRR. This instability is attributed to the nonlinear mixing of the resonance modes of the two cavities. In addition, using the PC formalism, we show for the first time that Ikeda instability can occur in a double CMRR.

For a double CMRR with FC induced nonlinearity, we showed that multistability occurs due to the presence of two resonance modes in the structure. Also, unlike in a single MRR, two types of SP can occur in a double CMRR. On the first branch SP has the same critical FC lifetime as in a single MRR, but higher order SPs (SPs on the upper branches) are independent of the carrier lifetime. Also due to resonance splitting, the range of linear phase detune over which SP can occur is much wider than in a single MRR.

We also extended our analysis of double CMRRs to CMRR chains of length N_z. To facilitate the analysis, we developed general matrix formalisms based on the EC and PC models for describing the nonlinear dynamics of the CMRR chains with instantaneous nonlinearity. Our numerical studies showed that by increasing the CMRR length, the threshold powers for observing SP and Ikeda instability can be reduced, although the Ikeda threshold power is still impractically high for integrated photonic devices.

4 Coupled Map Lattice (CML) description of long chain CROW with Instantaneous Nonlinearity

In the previous chapter, we developed the EC and PC matrix formalisms, which are appropriate for analyzing the stability of short chains of nonlinear CMRRs. For long chains of CMRRs, the matrix approach can become very computationally intensive, making it less suitable for studying the dynamics of nonlinear propagation of light in such structures. Also, while the matrix formalism is widely used for analyzing the dispersion characteristics of light propagation in an infinite CROW, it cannot be used to describe light propagation in an infinitely long nonlinear CROW.

In this chapter, we develop an alternative method for analyzing the temporal behaviours of long chains of nonlinear CMRRs based on the Coupled Map Lattice (CML) theory. More specifically, using a hybrid EC-PC model, we show that a nonlinear CROW can be described as a one-dimensional (1D) coupled map lattice system. For simplicity, we will limit the model to only structures with instantaneous Kerr nonlinearity.

This chapter is organized as follows. We will begin by providing a theoretical background of coupled map lattice systems in Section 4.1. In Section 4.2 we will formulate a CML description of long chains of CMRRs. With the help of the CML formalism, we will study the spatiotemporal dynamics of nonlinear CROW waveguides. The chapter is concluded in Section 4.3.

4.1 Theoretical background

Coupled Map Lattice was originally developed in the mid 1980's to study the formation of spatiotemporal patterns in extended nonlinear systems with 1D, 2D and 3D chaotic elements such as logistic, duffing, or Hénnon maps. Kuznetsov applied CML theory to electrical circuits by forming a renormalization group approach [59]. Kapral used CMLs to model chemical reactions in spatial platforms [60]. Rayleigh–Bénard convection has been studied using CML theory [88]. Kaneko is widely recognized as the pioneer and most active researcher in this area, and his focus was much broader than his contemporaneous researchers in this field [89]. During the last decade, CMLs have been expanded to study spatiotemporal dynamic behaviours and pattern formation in a broad spectrum of topics including biology, applied mathematics, engineering, and cryptography [90-92].

Like cellular automata, a CML describes the discrete features of a network consisting of discrete nonlinear elements [93]. A CML consists of a chain or lattice of elements in which the value at each site depends on its own nonlinear dynamics and the nonlinear dynamics of adjacent sites. In 1983 Kaneko introduced the following general equation to describe any CML system [58, 88, 89]:

$$u_{n_z}^{n_t+1} = (1-\kappa) f\left(u_{n_z}^{n_t}\right) + \frac{\kappa}{2}\left(f\left(u_{n_z+1}^{n_t}\right) + f\left(u_{n_z-1}^{n_t}\right)\right) \therefore n_t \in N; n_z \in N; \kappa \in [0,1] \qquad (4.1)$$

In the above equation, u, κ and f are the state variable, coupling strength, and local dynamic, respectively, and n_t and n_z represent the time and spatial steps of the state variable of u. We can depict the relation between adjacent sites by the graph diagram in

figure 4.1 [94]. The dynamics of the n_z^{th} site depends not only on its own dynamics but also the dynamics of the adjacent nodes. A CML is discrete by nature, with the system dynamics described at discrete time steps and spatial locations.

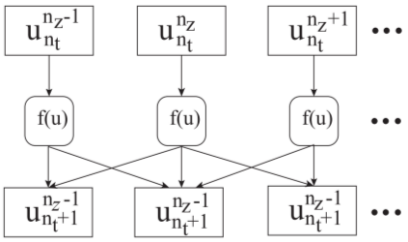

Figure 4.1, Schematic of the interactions between the dynamics of neighbors in a CML

A typical CML system consists of the following essential ingredients:

Local dynamics: The local dynamics describes how the state variable at a local node (or site) evolves with time. It is specified in the form of a discrete map (f) and is the source of the temporal pattern formation at a local node.

Coupling: The coupling or interaction term (κ) models how information transmission occurs between different nodes in the spatial network (lattice). For instance, in a chemical reaction the interaction term expresses the diffusion of concentration from one location to another. In general, there are two types of coupling depending on the nature of the information transmission. If the nodes interact only with adjacent nodes, the coupling is local. On the other hand, if the interaction occurs between nodes distributed over the network, the coupling is global. In addition, the coupling is said to be homogeneous if the coupling strength is constant between any two nodes. In the opposite case, the coupling is heterogeneous if the coupling strength between the two nodes depends on the location of the nodes.

Boundary conditions: Like wave propagation in a medium, boundary conditions are crucial in determining the output of a CML system for a given input. Specific boundary conditions will be described when we apply the CML theory to analyze CMRR structures.

In the next section, we will show how the CML theory can be used to describe the spatiotemporal dynamics of an optical wave propagating in a long or infinite chain of CMRRs with instantaneous nonlinearity.

4.2 CML Description of nonlinear CMRRs

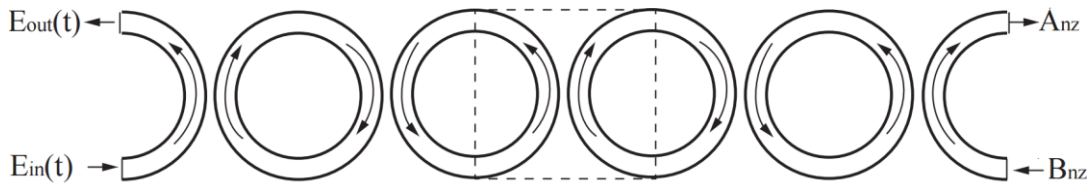

Figure 4.2,The structure of CROW waveguide

Figure 4.2 shows a schematic of a chain of CMRR. We denote the fields at the input port and the through (or reflection) port as E_{in} and E_{out}, respectively. We define the fields propagating in microring n_z as A_{nz} and B_{nz}, as shown in the figure. We assume the coupling between microrings are a constant value of κ. The transmission coefficient is given by $\tau_{cp} = \sqrt{1-\kappa^2}$. By defining the unit cell as shown in figure 4.2, we can relate the forward and backward waves in each unit cell by the following scattering matrix M:

$$\begin{bmatrix} A_{n_z+1} \\ B_{n_z+1} \end{bmatrix} = M \begin{bmatrix} A_{n_z} \\ B_{n_z} \end{bmatrix} \qquad (4.2.a)$$

$$M = \frac{j}{\kappa}\begin{bmatrix} -1 & \tau_{cp} \\ -\tau_{cp} & 1 \end{bmatrix} \tag{4.2.b}$$

Using the above relation and accounting for the nonlinear phase shift due to Kerr effect in microring n_z, we can express the evolution of the field in the n_z^{th} unit cell by [57]

$$A_{n_z}^{n_t+1} = a_{rt}\left[j\kappa A_{n_z-1}^{n_t} e^{-j\xi_{kerr}\left|A_{n_z-1}^{n_t}\right|^2} + \tau_{cp} B_{n_z}^{n_t} e^{-j\xi_{kerr}\left|B_{n_z}^{n_t}\right|^2} \right] e^{-j\Delta\varphi_{L,1}} \tag{4.3.a}$$

$$B_{n_z}^{n_t+1} = a_{rt}\left[j\kappa B_{n_z+1}^{n_t} e^{-j\xi_{kerr}\left|B_{n_z}^{n_t}\right|^2} + \tau_{cp} A_{n_z}^{n_t} e^{-j\xi_{kerr}\left|A_{n_z}^{n_t}\right|^2} \right] e^{-j\Delta\varphi_{L,1}} \tag{4.3.b}$$

where $\zeta_{kerr} = 4\pi^2 R n_2/\lambda_0$ and $\Delta\varphi_{L,1} = 4\pi^2 R n_g/\lambda_0$. The above equations indicate that the dynamics of the forward wave (A_{nz}) at the n_z^{th} node depends on the backward wave (B_{nz}) at same node and the forward wave (A_{nz-1}) at the n_z-1^{th} node, while the dynamics of the backward wave (B_{nz}) at the n_z^{th} node depends on the forward wave at the same node (A_{nz}) and the backward wave (B_{nz+1}) at n_z+1^{th} node.

It is apparent that equations (4.3) do not have the same form as the Kaneko equation (4.1) for a CML. Equations (4.3) are based on field coupling between two adjacent nodes through the scattering matrix M [95], whereas the CML equation is more closely associated with mean-field coupling between adjacent nodes. Thus, we need to derive an alternative formalism that encompasses some aspects of the EC model and some aspects of the PC model. More specifically, this new formalism should have the mean-field coupling nature of the EC model and the discrete nature of the PC model.

The first step to obtain the new model is to find the discrete solutions for the energies in the CMRRs. If we assume that the energy couplings (μ) between the microrings are

homogenous and the cavity lifetimes (τ_{ph}) and resonant frequencies (ω_0) are identical within the CROW waveguide, then the following differential equation describes the mean field dynamics of the stored energy in the n_z^{th} microring in the linear case:

$$\frac{da_{n_z}(t)}{dt} = \left(j\Delta\omega - \frac{1}{\tau_{ph}} \right) a_{n_z}(t) - j\mu\left(a_{n_z-1}(t) + a_{n_z+1}(t)\right) \tag{4.4}$$

where $\Delta\omega = \omega - \omega_0$. By integrating equation (4.4), we obtain the analytical solution at time $t+\Delta t$ as follows,

$$a_{n_z}(t+\Delta t) = e^{\left(j\Delta\omega - \frac{1}{\tau_{ph}}\right)\Delta t} a_{n_z}(t) - j\mu\left(a_{n_z-1}(t) + a_{n_z+1}(t)\right) \frac{\left[e^{\left(j\Delta\omega - \frac{1}{\tau_{ph}}\right)\Delta t} - 1 \right]}{\left(j\Delta\omega - \frac{1}{\tau_{ph}} \right)} \tag{4.5}$$

The above analytical solution of equation (4.4) is valid in the vicinity of the resonance wavelength. This region of operation is important for us because SP is most likely to occur in this region.

Taking Δt as the microring roundtrip time T_{rt}, we can express the stored energy in the microring after each roundtrip as

$$a_{n_z}(t+T_{rt}) = a_{rt} e^{-j\Delta\varphi_{L,1}} a_{n_z}(t) - j\mu\left(a_{n_z-1}(t) + a_{n_z+1}(t)\right) \frac{\left[a_{rt} e^{-j\Delta\varphi_{L,1}} - 1 \right]}{j\Delta\omega - \frac{1}{\tau_{ph}}} \tag{4.6}$$

In the above equation, we have made the substitution

$$a_{rt} e^{-j\Delta\varphi_{L,1}} = e^{\left(j\Delta\omega - \frac{1}{\tau_{ph}}\right)T_{rt}} \tag{4.7}$$

where $\Delta\phi_{L,1}$ and a_{rt} represent the linear roundtrip phase and roundtrip amplitude attenuation, respectively, in the microring.

By approximating the exponential term by a first-order Taylor series expansion, we can express equation (4.6) as

$$A_{n_z}^{n_t+1} = a_{rt} e^{-j\Delta\varphi_{L,1}} A_{n_z}^{n_t} - j\kappa\left(A_{n_z-1}^{n_t} + A_{n_z+1}^{n_t}\right) \tag{4.8}$$

where we have made the replacements

$$\mu T_{rt} = \kappa \tag{4.9.a}$$

$$a = A\sqrt{T_{rt}} \tag{4.9.b}$$

Equation (4.8) has a similar form as the Kaneko equation (4.1) for a CML in 1D. If we include the nonlinear phase shift in equation (4.8), the resulting equation will describe the spatiotemporal evolution of the power distribution in a nonlinear CROW. We will first examine the linear response of the CML model of a CROW waveguide.

4.2.1 Linear response of the CML model

To validate the hybrid EC-PC model (equation (4.8)) for the CMRR structure, we compare the band diagram and steady state response for a linear CMRR with the results obtained from the scattering matrix method (equation (4.3) for the linear case). To obtain the band diagram from the CML equation, we consider an infinite CROW with constant coupling coefficient κ and no loss, and derive the dispersion relation of the structure.

The steady state solution of equation (4.8) is obtained by setting $A(n_z, n_t + 1) = A(n_z, n_t) = A_{f,n_z}$:

$$A_{f,n_z} = a_{rt} e^{-j\Delta\varphi_{L,1}} A_{f,n_z} - j\kappa\left(A_{f,n_z-1} + A_{f,n_z+1}\right) \tag{4.10}$$

Based on the Floquet-Bloch theory, the field of a light wave propagating in the CROW structure should have solution of the form $A_{f,n_z} = A_0 e^{-jQn_z}$, where Q is the Bloch wave number. Substituting the Bloch wave solution into equation (4.10), we get

$$\left(1 - a_{rt} e^{-j\Delta\varphi_{L,1}}\right) A_0 e^{-jQn_z} - j\kappa\left(A_0 e^{-jQ(n_z+1)} + A_0 e^{-jQ(n_z-1)}\right) = 0 \tag{4.11}$$

By eliminating the common factor $A_0 e^{-jQn_z}$ and simplifying, we obtain the following dispersion relation for a lossless CROW

$$\left(\frac{1 - e^{-j\Delta\varphi_{L,1}}}{j2\kappa}\right) = \cos Q \tag{4.12}$$

The above dispersion relation is consistent with the well-known dispersion relation of a CROW waveguide obtained using the scattering matrix, $\frac{\sin\Delta\varphi_{L,1}}{\kappa} = \cos Q$.

To validate this analytical equation, we show in figure 4.3 the dispersion curves for a CROW structure with 1% power coupling between adjacent MRRs in the first Brillouin zone using the hybrid EC-PC method and the scattering matrix method.

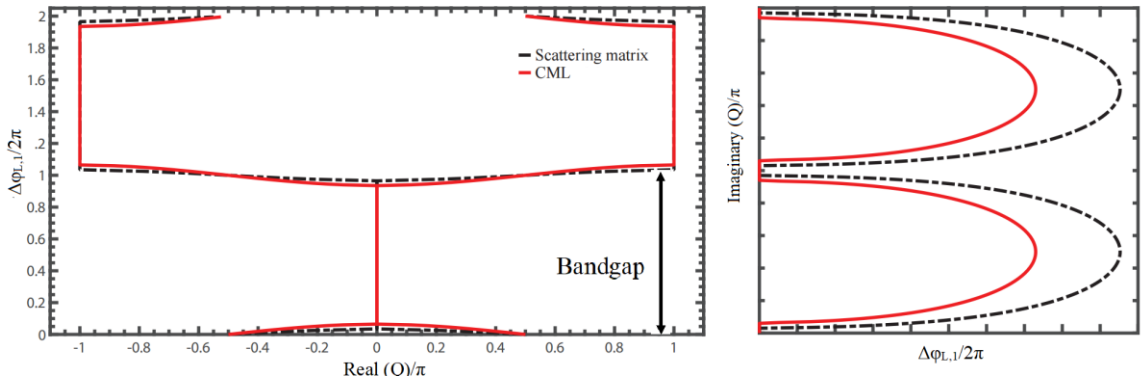

Figure 4.3, Band diagram of lossless CROW waveguide. Left) linear phase shift vs real part of Ω. Right) imaginary part of Ω as a linear phase detune

As expected, both dispersion curves show the formation of a band gap due to periodic reflections of an optical wave as it propagates along the CROW structure. Apart from a small discrepancy between these two methods caused by the Taylor approximation in equation 4.12 , the dispersion diagrams suggest that both models are consistent with respect to the linear behavior of an infinite CROW waveguide.

We next validate the hybrid EC-PC model for a CROW of finite length by computing the steady-state power distribution in a chain of 30 lossless CMRRs. The power coupling ratio between adjacent MRRs is 1%. In figure 4.4, we plot the stored power in the last MRR (n_z = 30) as a function of the linear phase detune. For comparison, the results obtained from the EC and PC models are also shown. We observe that the CML result falls between the EC and PC models. Specifically, it inherits multiple peaks (or ripples) within the passband from the PC model but has the same bandwidth as the EC model. Due to the periodic structure of the CROW waveguide, photonic band gaps exist (as shown in figure 4.3) in which light cannot propagate and the input power is mostly reflected.

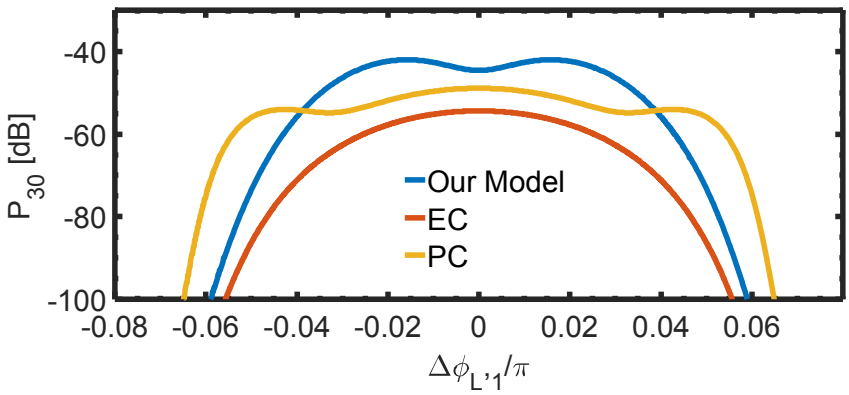

Figure 4.4, The stored power in 25th MRR vs linear phase detune

These frequencies fall outside the transmission bandwidth of the plot in figure 4.4. The finite bandwidth of the CROW waveguide also suggests that it has a phase-dependent (or frequency) linear attenuation, as can also be deduced from the band diagram. To show the phase-dependent attenuation, we plot the spatial distribution of the stored power in a CROW waveguide of 100 long CROW waveguide for various linear phase detunes in figure 4.5. We observe that the power attenuation increases with larger phase detune from the resonance which increases the threshold of nonlinear dynamic behavior.

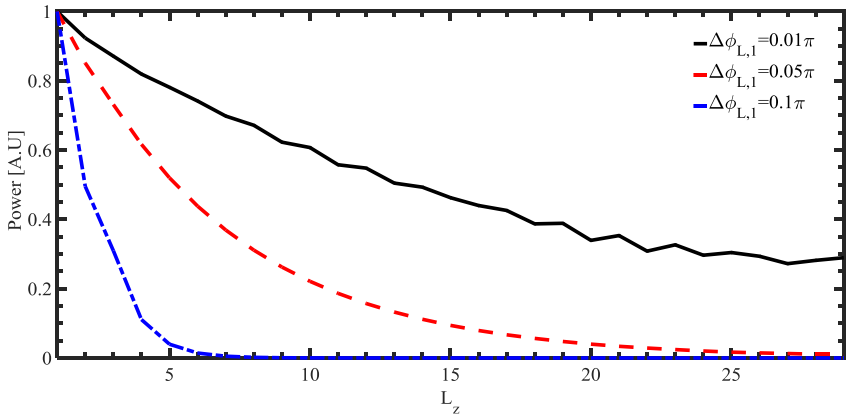

Figure 4.5, The stored power as a function of the MRR position in a 100 long CROW waveguide for different linear phase detunes and κ=1%

4.2.2 CML model of CMRRs with instantaneous Kerr nonlinearity

Having verified the CML model for linear CMRRs, we now modify the equation to study

the temporal dynamics of a CROW waveguide with instantaneous Kerr nonlinearity. The Kerr effect induces a nonlinear phase shift in each MRR given by $\zeta_{kerr}|A|^2$, where $|A|^2$ is the stored power in the MRR. This phase shift can be incorporated into the CML equation (4.10) to give

$$A_{n_z}^{n_t+1} = a_{rt} e^{-j\left(\Delta\varphi_{L,1}+\xi_{kerr}\left|A_{n_z}^{n_t}\right|^2\right)} A_{n_z}^{n_t} - j\kappa\left(A_{n_z-1}^{n_t} + A_{n_z+1}^{n_t}\right) \tag{4.13}$$

By defining the local dynamic function f as

$$A_{n_z}^{n_t+1} = f\left(A_{n_z}^{n_t}\right) = a_{rt} e^{-j\left(\Delta\varphi_{L,1}+\xi_{kerr}\left|A_{n_z}^{n_t}\right|^2\right)} A_{n_z}^{n_t} \tag{4.14}$$

we can express equation (4.14) in the form of the general Kaneko CML equation (4.1):

$$A_{n_z}^{n_t+1} = f\left(A_{n_z}^{n_t}\right) - j\kappa\left(f\left(A_{n_z-1}^{n_t-1}\right) + f\left(A_{n_z+1}^{n_t-1}\right)\right) \tag{4.15}$$

The above equation describes the spatiotemporal field evolution in a nonlinear CROW with homogeneous coupling as a 1D CML system. At the input end of the CROW (z = 0), we apply the boundary condition

$$A_{n_z}^{n_t+1} = f\left(A_{n_z}^{n_t}\right) - j\kappa f\left(A_{n_z+1}^{n_t-1}\right) - j\kappa E_{in} \tag{4.16}$$

where E_{in} is the input field. At the output end (at $z = n_z$) of the waveguide, we set $A\left(n_{z+1}, n_t\right) = 0$ to get the boundary condition

$$A_{n_z}^{n_t+1} = f\left(A_{n_z}^{n_t}\right) - j\kappa f\left(A_{n_z-1}^{n_t-1}\right) \tag{4.17}$$

We use the CML equation (4.15) along with the boundary conditions to simulate the nonlinear dynamics of a Chalcogenide CROW waveguide with instantaneous Kerr nonlinearity. The power coupling between adjacent MRRs is set to $\kappa^2 = 1\%$ and the

coupling between the input waveguide and the first MRR is 16%. Loss is specified in the MRRs by setting the photon lifetime of each resonator to 190ps. The linear and nonlinear parameters of Chalcogenide are the same as in section 3.1.3. These parameters are listed in table 4.1. The input wave is a CW optical signal at the wavelength of 1550 nm.

As discussed in [57], the effect of Kerr nonlinearity is to shift the dispersion relation of the CROW structure in the $\Delta\varphi_{L,1}$-Q plane and reduces its transmission bandwidth. In figure 4.6, we plot the stored power in the last MRR for a CROW waveguide with a length of 30 (N_z=30) as a function of the linear phase detune for different input powers. We observe that the bandwidth of the CROW waveguide is not a constant value but depends on the input power. Also, the center frequency of the passband increases with increasing input power because of Kerr effect. In order to reduce the threshold powers for observing nonlinear dynamics in the CROW waveguide, the operating wavelength should be within the bandwidth of the structure to reduce the phase-dependent propagation loss.

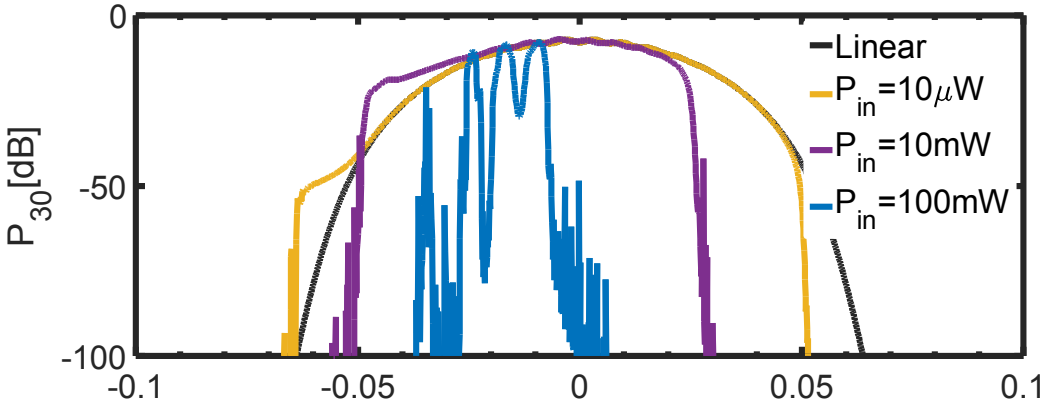

Figure 4.6, Plot of the stored power in the 30th MRR vs linear phase detune

To study the nonlinear dynamics of the CROW waveguide, we add a small perturbation $\varepsilon_{nz}(t)$ to the stationary field amplitude, $A_{nz}(t) = A_{f,nz} + \varepsilon_{nz}(t)$. The fixed point (or

stationary solution) $A_{nz,f}$ is the steady-state solution of the CML equation (4.15) with $A(n_z, n_{t+1}) = A(n_z, n_{t-1}) = A(n_z, n_t) = A_{f,nz}$:

$$A_{f.nz} - f(A_{f,nz}) = -j\kappa\left(f(A_{f,nz-1}) + f(A_{f,nz+1})\right) \tag{4.18}$$

By substituting the perturbed solution $A_{nz}(t) = A_{f,nz} + \varepsilon_{nz}(t)$ into equation (4.15) and linearizing the equation to keep only terms of first order in $\varepsilon_{nz}(t)$, we obtain the following system of coupled characteristic equations:

$$\begin{aligned}\varepsilon_{nz}(t+T_{rt}) = a_{rt} e^{-j\left(\Delta\varphi_{L,nz} + \xi_{kerr}\left|A_{f,n_z}\right|^2\right)}\left(1 - j\xi_{kerr}\left|A_{f,n_z}\right|^2\right)\varepsilon_{nz}(t) \\ - j\xi_{kerr}A_{f,n_z}^2\,\varepsilon_{nz}^*(t) - j\kappa\left(\varepsilon_{nz-1}(t) + \varepsilon_{nz+1}(t)\right)\end{aligned} \tag{4.19.a}$$

$$\begin{aligned}\varepsilon_{nz}^*(t+T_{rt}) = a_{rt} e^{j\left(\Delta\varphi_{L,nz} + \xi_{kerr}\left|A_{f,n_z}\right|^2\right)}\left(1 + j\xi_{kerr}\left|A_{f,n_z}\right|^2\right)\varepsilon_{nz}^*(t) \\ + j\xi_{kerr}A_{f,n_z}^{*2}\,\varepsilon_{nz}(t) + j\kappa\left(\varepsilon_{nz-1}^*(t) + \varepsilon_{nz+1}^*(t)\right)\end{aligned} \tag{4.19.b}$$

The perturbative terms at time step of $t+T_{rt}$ and t can be related to each other through the Jacobian matrix as follows,

$$\boldsymbol{\varepsilon}(t+T_{rt}) = \mathbf{J}\boldsymbol{\varepsilon}(t) \tag{4.20}$$

where $\boldsymbol{\varepsilon} = [\ldots.,\varepsilon_{nz-1}, \varepsilon_{nz-1}^*, \varepsilon_{nz}, \varepsilon_{nz}^*, \varepsilon_{nz+1}, \varepsilon_{nz+1}^*, \ldots.]^T$. The Jacobian matrix is as follows,

$$\begin{bmatrix} \varepsilon_{nz-1}(t+T_{rt}) \\ \varepsilon_{nz-1}^*(t+T_{rt}) \\ \varepsilon_{nz}(t+T_{rt}) \\ \varepsilon_{nz}^*(t+T_{rt}) \\ \varepsilon_{nz+1}(t+T_{rt}) \\ \varepsilon_{nz+1}^*(t+T_{rt}) \end{bmatrix} = \begin{bmatrix} U_{nz-1} & G_{nz-1} & -j\kappa & 0 & 0 & 0 \\ G_{nz-1}^* & U_{nz-1}^* & 0 & j\kappa & 0 & 0 \\ -j\kappa & 0 & U_{nz} & G_{nz} & -j\kappa & 0 \\ 0 & j\kappa & G_{nz}^* & U_{nz}^* & 0 & j\kappa \\ 0 & 0 & -j\kappa & 0 & U_{nz+1} & G_{nz+1} \\ 0 & 0 & 0 & j\kappa & G_{nz+1}^* & U_{nz+1}^* \end{bmatrix} \begin{bmatrix} \varepsilon_{nz-1}(t) \\ \varepsilon_{nz-1}^*(t) \\ \varepsilon_{nz}(t) \\ \varepsilon_{nz}^*(t) \\ \varepsilon_{nz+1}(t) \\ \varepsilon_{nz+1}^*(t) \end{bmatrix} \tag{4.21}$$

For simplicity in demonstration of Jacobian matrix we present

$a_{rt}e^{j\left(\Delta\varphi_{L,nz}+\xi_{kerr}\left|A_{f,n_z}\right|^2\right)}\left(1+j\xi_{kerr}\left|A_{f,n_z}\right|^2\right)$ and $-j\xi_{kerr}A_{f,n_z}^2$ with U_{nz} and G_{nz}, respectively. In the above Jacobian matrix, we only discussed information of nodes of n_{z-1},n_z and n_{z+1}.

The eigenvalues of the Jacobian matrix determine the temporal behavior of the CROW waveguide as follows:

1. If all the eigenvalues have absolute value less than one, the system is stable
2. If an eigenvalue is real and larger than one, the system exhibits bistability
3. If an eigenvalue is real and smaller than -1, the system exhibits Ikeda instability
4. If an eigenvalue is complex with the real part larger than one, self-pulsation occurs.

The first task in the analysis of the nonlinear behaviors of the CROW waveguide is to obtain the stability curve of the system, i.e., the plot of the power in the waveguide vs. input power at a fixed linear phase detune. As an example, we show in figure 4.7 the stability curve for a chalcogenide CROW waveguide with a short length of 4 MRRs at a linear phase detune of -0.1π. The parameters of the structure are listed in table 4.1. The power in the CROW waveguide is taken to be the stored power in last MRR. It is evident from the plot that multistability occurs in this system because the CML model developed for the CROW waveguide (equation (4.13)) allows each MRR to support an infinite number of resonance modes.

Table 4.1, Parameters of Chalcogenide CROW waveguide of length 4

Parameter	Discerption	Value	Dimension
R	Ring radius	200	μm
A_{eff}	Effective area	0.1326	μm^2
n_g	Group Index	3.363	-
n_{eff}	Effective index of Waveguide	1.836	-

n_2	Kerr Nonlinearity	11×10^{-18}	$m^2.W^{-1}$
a_{rt}	Round trip loss	.98	-
κ_1	Coupling between MRR and waveguide	.4	-
κ_2	Coupling between MRRs	.1	-

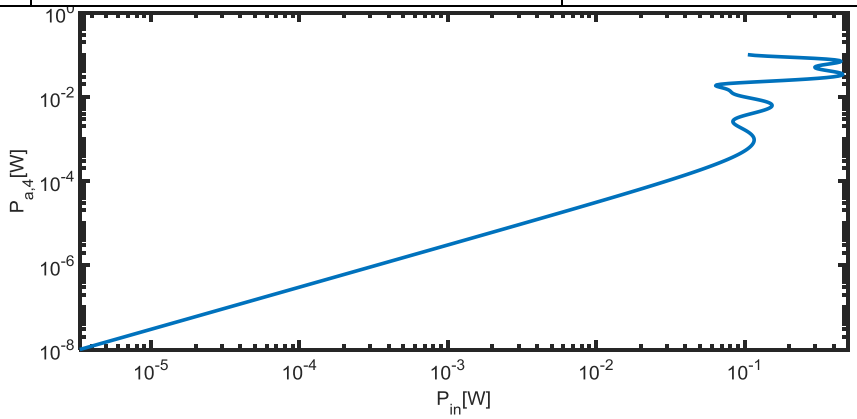

Figure 4.7, The stability curve of CROW waveguide of length 4 showing the stored power in microring 4 vs. the input power at a fixed linear phase detune of -0.1π.

In figure 4.8, we show the stability map of the same CROW waveguide, where the regions of stable, BS, Ikeda and SP are indicated by the colors blue, yellow, brown and azure, respectively. The map confirms that the CML formalism can also predict BS, SP and Ikeda instabilities as obtained with the PC model in the previous section. It is worth to mention that a longer CROW waveguide behaves more chaotic. Because chaotic behavior is not traceable by the 1st order perturbative stability analysis, it appears as a SP in stability map. As a result, figure 4.8 doesn't have a solid distinguished color codes . For example, in the yellow region, it seems that are also spots of brown.

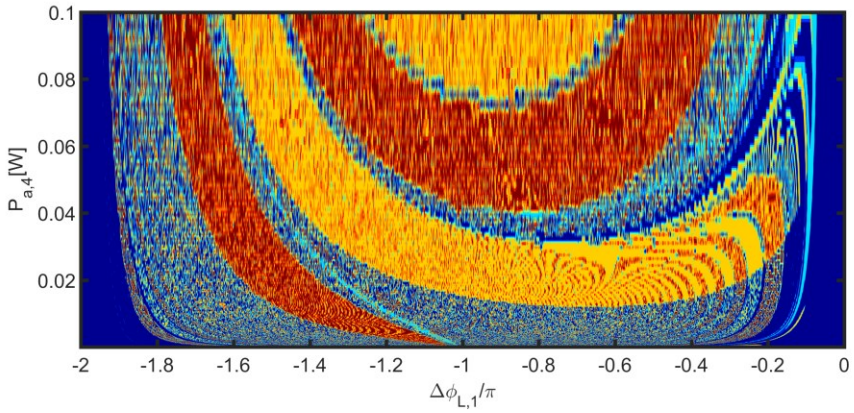

Figure 4.8, The stability map showing regions of BS, SP and Ikeda instabilities as a function of the power in the 4th MRR and the linear phase detune.

Next we investigate the threshold power required to reach SP in the CROW waveguide. The SP threshold power is defined as the minimum power to reach SP over the linear phase detuning range from 0 to -2π. Figure 4.9 plots the SP threshold power (blue line) and the frequency of oscillation (black line) as functions of the CROW length. We observe that the SP threshold initially decreases rapidly as the CROW length reaches up to about 5 MRRs, then settling to a relatively constant power level of around 44 mW with further increase in the CROW length. This result is in good agreement with result of matrix stability analysis (Chapter 3) where the optimum waveguide length to have SP is four. The relative independence of the SP threshold power on the CROW length can be explained in terms of the power distribution in a linear CROW waveguide. As figure 4.5 shows, the stored powers in the MRRs decay along the CROW length so the nonlinear effect in each MRR becomes less pronounced by increasing physical length of the CROW waveguide. These two competing effects (increasing interaction length and less nonlinear interaction) lead to the saturation of the SP threshold power for long CROW lengths.

The plot in figure 4.9 also shows that the oscillation frequency jumps from $0.004/T_{rt}$ to $0.07/T_{rt}$ as the CROW length increases. For a chalcogenide MRR with a 100 μm radius, the SP frequency can vary between 487 MHz and 8.2 GHz depending on the CROW length. We also note that it is possible to tune the SP frequency by varying the linear phase detune of the MRRs.

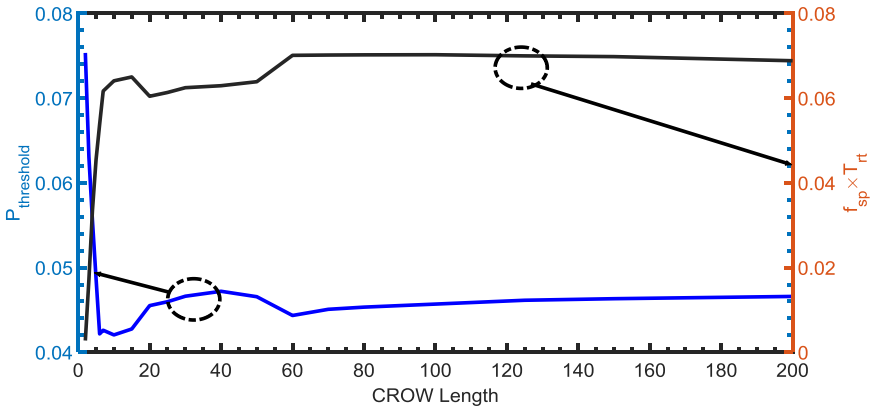

Figure 4.9, Threshold power and frequency of SP as a function of CROW length

We also study the threshold power required to reach Ikeda instability in a CROW waveguide. We recall that Ikeda instability arises due to four-wave mixing between adjacent modes of the MRRs and the minimum threshold power generally occurs when the linear roundtrip phases of the MRRs are tuned to around π. Figure 4.10 shows the threshold power for observing Ikeda instability and the associated phase detune versus the CROW waveguide length. We observe that in contrast to SP, the Ikeda threshold power in general increases with the CROW length. The reason for this behavior can be explained as follows. As the number of resonators increases, the CROW waveguide behaves more like an infinite CROW. In an infinite CROW with -π linear phase detune, the light experiences strong reflection so that very little optical power can build up in each resonator. As a result higher input power is required to cause four-wave mixing

in the resonators, resulting in higher threshold powers required to achieve Ikeda instability. The plot in figure 4.10 verifies that the phase shift needed to achieve minimum threshold power for Ikeda instability is about -π, and the threshold power grows substantially as the number of MRRs increases. This result shows that CROW waveguide is not a suitable platform for observing Ikeda instability.

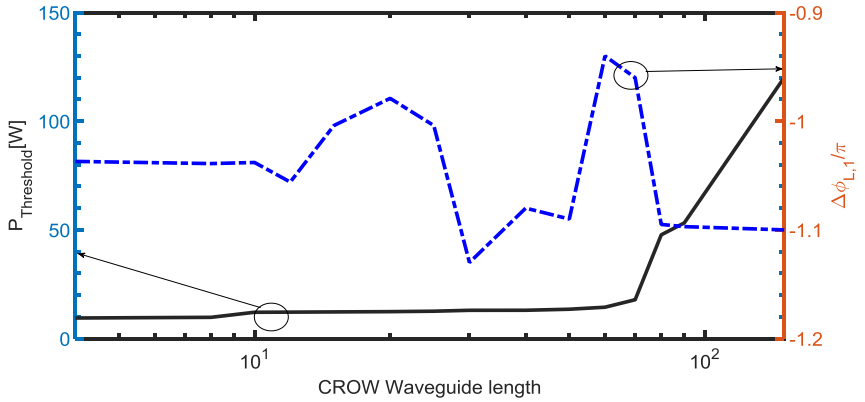

Figure 4.10, The threshold power for observing Ikeda instability (black) and corresponding phase detune (blue) versus the CROW length

4.2.3 Spatiotemporal instability in a nonlinear CROW with gain

The primary purpose of the CML formalism is to study spatiotemporal instabilities in an extended spatial system such as chemical reaction-diffusion system. In order for spatiotemporal patterns to form in these systems, the local dynamics must also have gain [91]. As we showed before, the local map of a nonlinear CROW waveguide is given by $f(u)=a_{rt}e^{-j\left(\Delta\varphi_{L1}+\xi_{kerr}|u|^2\right)}u$. Since this map does not have a gain mechanism, the only effects that can be observed are temporal instabilities such as BS, self-pulsation and Ikeda oscillations. We can modify the local dynamic of each MRR to include gain as follows:

$$f(u)=a_{rt}Ge^{-j\left(\Delta\varphi_{L,1}+\xi_{kerr}|u|^2\right)}u \tag{4.21}$$

where G is the gain factor. Depending on the G value, various spatial instabilities can occur in the CROW waveguide in addition to temporal instabilities.

One of the possible solution to implement a constant gain to each MRR is introducing erbium doped material to this platform. Also inserting a quantum well GaAs as a gain medium in MRR is an alternative solution.

Similar to temporal instability, if the stored optical power in a CROW waveguide experiences growth along the direction of propagation, the CROW structure becomes spatially unstable. To distinguish between temporal and spatial instabilities, we present below a study of CROW waveguides with different gain values.

For G=1, the system is a simple CROW waveguide where the optical power decays during propagation along the waveguide due to linear loss and limited bandwidth of the MRRs. Figure 4.11 shows the steady-state power in each MRR for a CROW waveguide with linear phase detune of 0.02π, coupling coefficient κ of 0.05, and roundtrip attenuation of 0.98. The stored power is seen to decay exponentially as a function of the waveguide length. We can achieve temporal SP by applying proper phase detuning of each MRR and appropriate input power to the structure. For example, for an input power of 0.1W and linear phase detune of 0.02π, each MRR exhibits temporal oscillations with a period of $40\times T_{rt}$. Figure 4.12 shows the time trace of the stored power in the 60^{th} and 80^{th} MRRs showing temporal oscillatory behavior. This temporal oscillatory signal is modulated by high intensity pulse shape signal.

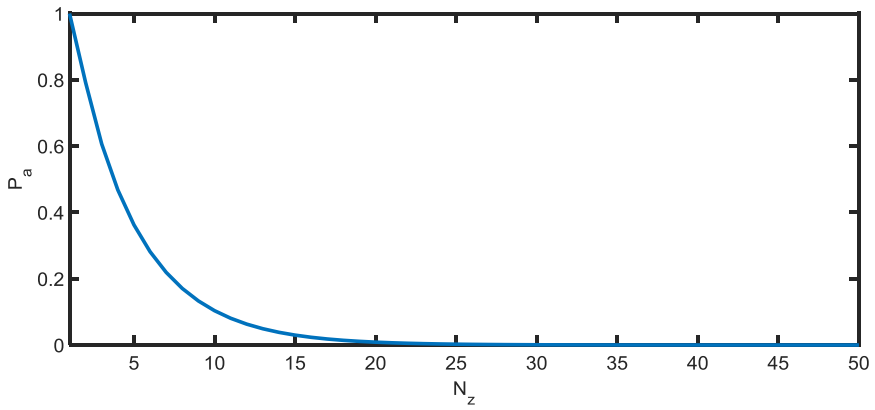

Figure 4.11, The steady state stored power vs waveguide length in a CROW waveguide with G = 1.

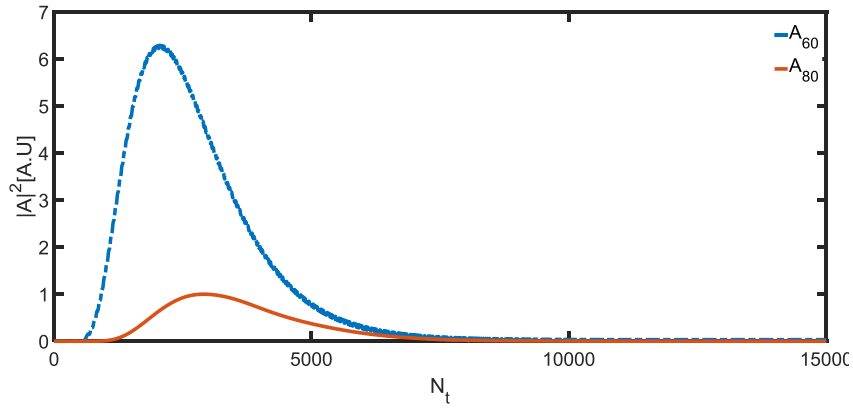

Figure 4.12, The temporal behaviors of the stored powers in different MRRs of the CROW waveguide.

If we introduce gain to each MRR, depending on the value of the linear phase detune of the cavities, an optical signal can experience spatial instability as it propagates along the CML lattice. For example, for the same CROW waveguide but with a gain of G = 1.005, linear phase detunes of 0 and input power of 0.1W, we can observe quasi spatial pulsation with a spatial period of 4 N_z. Figure 4.13 (a) shows the stored power in each MRR at time step of $15000T_{rt}$ versus its location (N_z) along the CROW waveguide. The power has a quasi-periodic pattern where it peaks in roughly every fourth MRR. The temporal behavior of the stored power in the MRRs is illustrated in figure 4.13(b) for two MRR at locations of 40 and 100.

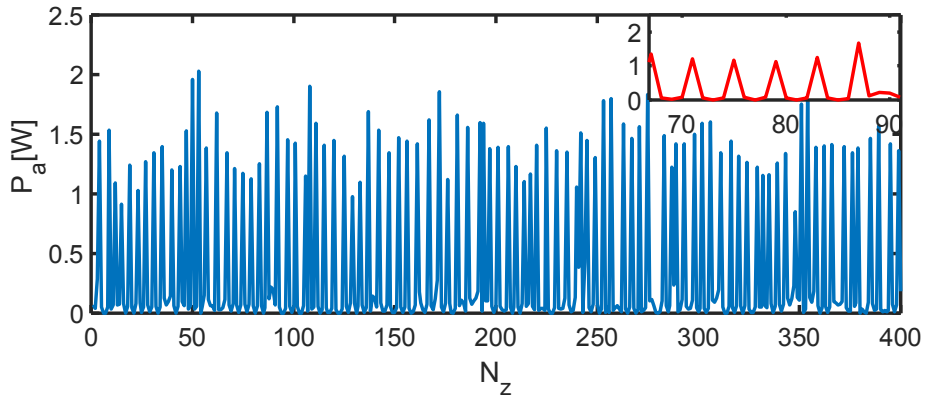

(a)

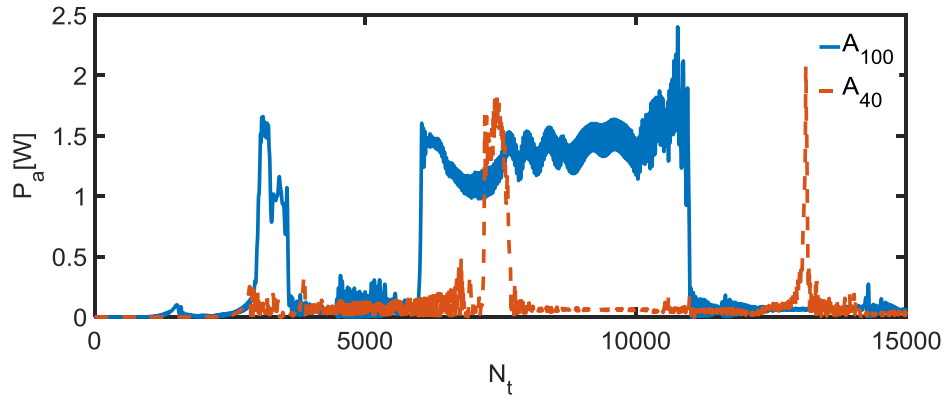

(b)

Figure 4.13, The stored power versus different location at time step 15000T_{rt}. (b) Time trace of stored power in 40th and 100th MRRR

In figure 4.14 (a) we show the spatiotemporal behavior of the CROW waveguide by plotting the stored power in each MRR as a function of both the time step (N_t) and spatial location (N_z). Also to show the spatial oscillatory behavior of this system, we plot the zoomed in 2D spatiotemporal behavior of this lattice in figure 4.14 (b).

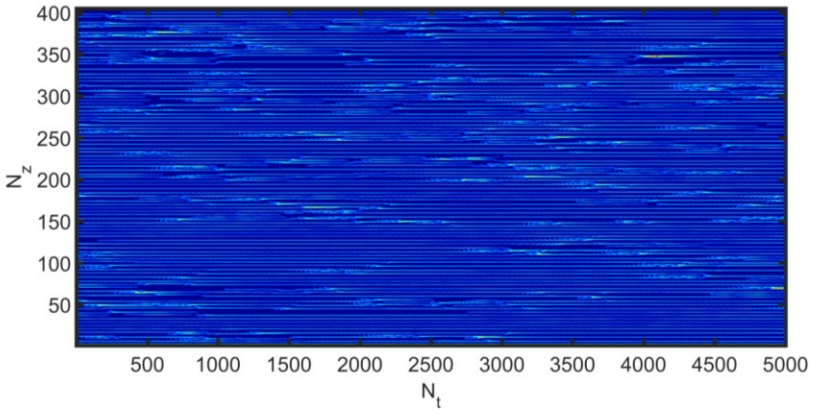

(a)

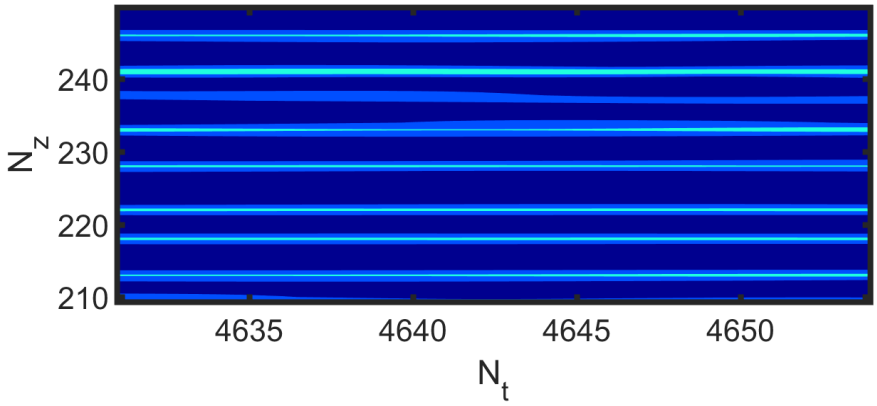

(b)

Figure 4.14, (a)2D plot of power vs. location (Nz) and time step (N_t) showing the spatiotemporal behavior of the CROW waveguide. (b) zoomed in plot of spatiotemporal behavior

The plot shows that the nonlinear CROW structure can exhibit spatiotemporal pattern forming which is characteristic of 1D CML systems. Results of figures 4.14(a) and 4.14 (b) have suggested to us that the quasi-spatial oscillation at different time step has a same period of oscillation and this pattern is independent of time.

It is interesting to point out that similar to temporal chaos in an optical cavity, spatial chaos may occur in a CROW waveguide with gain. For example, for the same input power and same linear phase detune, if we increase the gain of the CROW structure in the previous example to G = 1.018, the power distribution the CROW waveguide exhibits

spatial chaos, as shown in figure 4.15 (a). Figure 4.15 (b) shows the time trace of stored power at different locations of CROW waveguide experience temporal chaos.

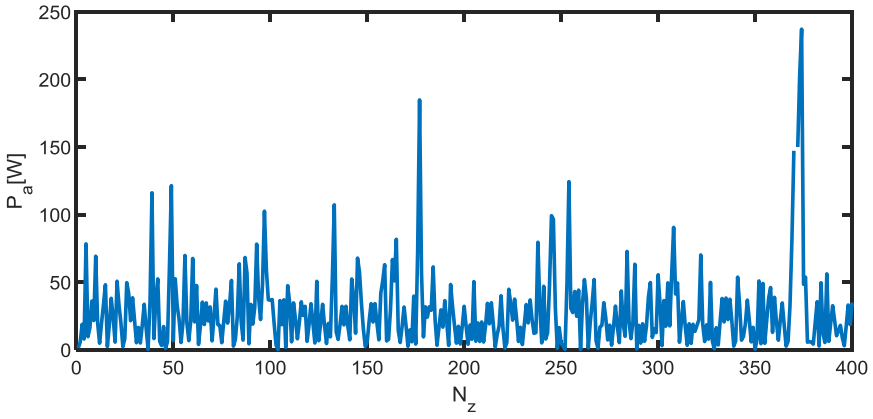

(a)

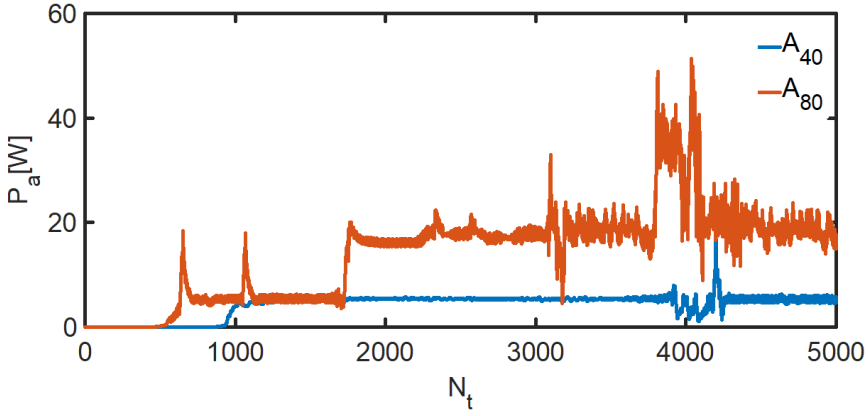

(b)

Figure 4.15, (a)Plot of the stored power at time step 15000Trt vs location of MRRs along the CROW waveguide showing spatial chaotic power distribution. (b) Time trace of stored power for different locations of 40 and 80

The spatiotemporal behavior of the structure is shown in the 2D map in figure 4.16 (a). The map shows that spatial chaos similar to figure 4.15 (a) exists in the CROW waveguide at any given time instant, and the power in at any location (MRR) in the CROW waveguide exhibits temporal chaos behavior similar to figure 4.15 (b) for two different locations of 40 and 80. A potential application of such a structure is for generating random sequences on an integrated photonic platform. To make

spatiotemporal chaotic behavior more pronounced, we plot the zoomed in of 4.16 (a) in figure 4.16 (b).

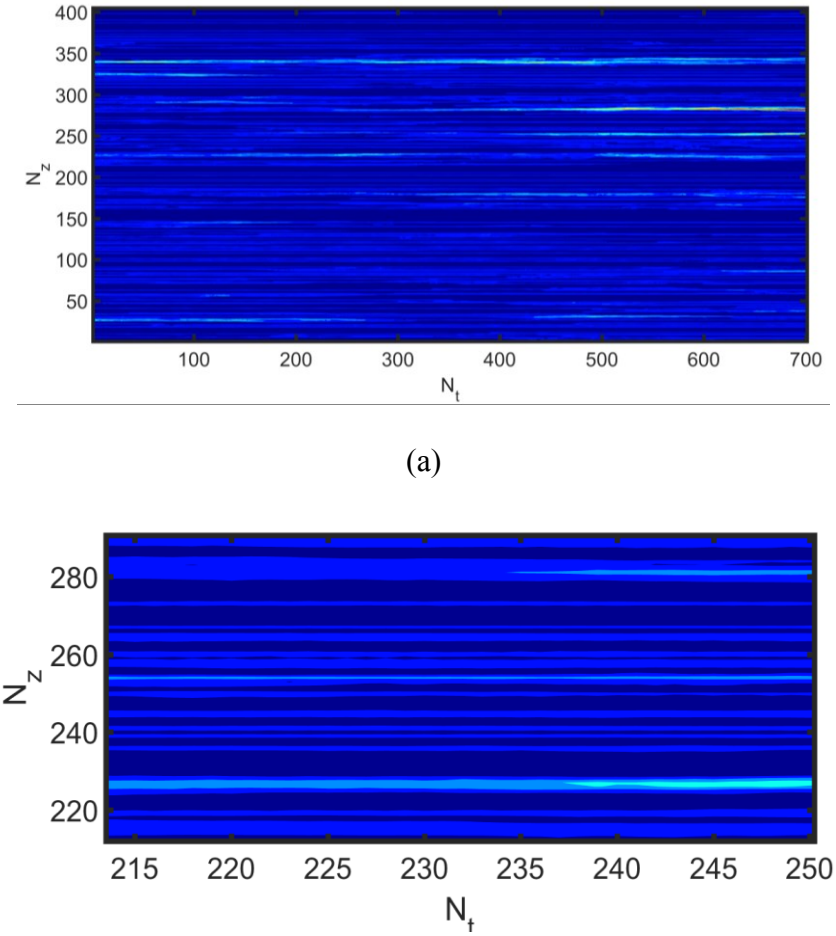

Figure 4.16, (a)2D plot of power vs. location (Nz) and time step (N_t) showing the spatiotemporal behavior of the CROW waveguide. (b) zoomed in plot of figure 4.16 (a)

4.3 Summary

In this chapter we developed a CML formalism for studying the nonlinear dynamics of spatially extended coupled MRRs, also known as nonlinear CROW waveguides. The main application of the CML theory is to study the formation of spatiotemporal patterns in a spatially extended system in the presence of two competing mechanisms in each local map. Since such competing mechanisms are lacking in a nonlinear MRR, we are

limited to studying the temporal instabilities such as self-pulsation and Ikeda oscillations in nonlinear CROWs. Nevertheless, several interesting conclusions can be drawn from our analysis. In particular, the CML model shows that the SP threshold power decreases with the CROW wavelength up to a critical length beyond which the threshold power becomes saturated (i.e., it becomes independent of the number of resonators). We attribute the main cause of this saturation effect to a reduction in the nonlinear interaction due to the decaying power distribution along the CROW waveguide. We also found that in contrast to SP, the threshold power for observing Ikeda instability in a nonlinear CROW generally increases with the CROW length since the device is operated within the photonic bandgap. We thus conclude that a CROW waveguide is not a suitable platform for observing Ikeda instability.

When we introduce gain to a nonlinear CROW, spatial instabilities can also emerge in addition to temporal instabilities. In particular, the power distribution along the CROW waveguide is shown to exhibit quasi-periodic spatial oscillations and even chaotic spatial patterns. These structures may have interesting applications, for example, in quasi-periodic and pseudo-random sequence generations.

5 Free Carrier Induced Nonlinear Relaxation in a Silicon Waveguide

In the previous chapters, we saw that free carriers generated by two-photon absorption in a semiconductor material such as silicon provide a significant source of nonlinearity, which can be exploited to achieve nonlinear processes such as bistability and self-pulsation in a resonator. We also found that the lifetime of the generated free carriers plays a critical role in determining the threshold powers required to observe these phenomena. Since the FC density is proportional to the FC lifetime at steady state, higher loss due to FC absorption also results from longer FC lifetime.

In general, the efficiency of a FC-induced nonlinear process in a silicon photonic device is limited by the additional loss due to free carrier absorption and by the finite lifetime of the free carriers. In particular, the FC lifetime limits the switching speed of a silicon microring resonator [1], reduces the wavelength conversion efficiency by four-wave mixing in a silicon waveguide [5], and places a lower limit on the threshold power required to achieve self-oscillations in a silicon micro-cavity [6]. While the dependence of the FC lifetime on the optical intensity in a silicon waveguide has been well studied, especially for silicon Raman laser applications [7, 8, 13], its effect on the relaxation time of light propagation in the waveguide has received much less attention, particularly at moderate to high powers where FCA dominates over TPA as the main source of nonlinear loss in the waveguide. An accurate analysis of the nonlinear transient behaviour of the power transmission could be important for all-optical switching and modulation

applications, as well as for FC lifetime measurements [9, 10]. For example, one of the methods used to determine the FC lifetime in a silicon waveguide is by propagating a high-intensity optical pulse in the waveguide and measuring the transient response of the transmitted power [9]. Due to the nonlinear loss caused by FCA, the optical pulse exhibits a temporal decaying behaviour and the decay time constant of the optical intensity is presumed to be the same as the relaxation time of the free carriers. This assumption, however, has not been rigorously validated, especially at moderate to high optical powers.

In this chapter we will perform a detailed analysis, through numerical simulations and experimental validation, of the effect of the FC lifetime on the transient response of the optical power in a silicon waveguide. Our model includes contributions to the FC lifetime from both surface/interface recombination and Auger recombination, the latter of which becomes important at high powers. We find that the decay time of the optical intensity is typically shorter than the FC lifetime, and is not constant but depends on the optical power. In particular, we find that the effective decay time is significantly reduced at high input powers. This result could have implications for nonlinear optics applications of silicon waveguides, such as the possibility of performing all-optical switching and modulation at speeds exceeding the limit set by the FC lifetime.

The chapter is organized as follows. In Section 5.1 we present a model for simulating nonlinear optical propagation in a silicon waveguide in the presence of free carriers generated by TPA. The model takes into account FC population relaxation times due to surface and interface recombination, Shockley-Reed-Hall recombination and Auger

recombination. Section 5.2 presents numerical simulations to study the transient responses of the FC density and power transmission in a silicon waveguide under step input and square wave input excitation. Section 5.3 presents the experiment performed and measurements obtained to validate the simulation results. A conclusion in provided in Section 5.4.

5.1 Theory and Background

When an optical signal with sufficiently high intensity in the telecommunication wavelength range propagates in a silicon waveguide, two-photon absorption causes electrons to be excited from the valence band to the conduction band (and holes from the conduction band to the valence band). This process causes the optical signal to lose a fraction of energy equal to $(\beta_{TPA}/A_{eff})\times P_a$, where P_a is the optical power, β_{TPA} is the TPA coefficient, and A_{eff} is the effective mode area of the silicon waveguide [96- 98]. The electrons in the conduction band can themselves interact with the optical field. In a process known as free carrier absorption, the optical signal excites the free electrons to higher energy levels within the conduction band [99, 100] and loses an amount of energy given by $\sigma_{FCA}N(t, z)$, where N is the FC density and σ_{FCA} is the FCA cross section. In addition, the optical signal also experiences linear loss given by the linear waveguide loss coefficient α_0. Taking these sources of loss together, we can write the equation for the optical power P(z, t) propagating in a silicon waveguide oriented along the z direction as [96, 97]:

$$\frac{\partial P(z,t)}{\partial z} = -\left(\alpha_0 + \frac{\beta_{TPA}}{A_{eff}} P(z,t) + \sigma_{FCA} N(z,t)\right) P(z,t) \qquad (5.1)$$

The free electrons generated by TPA diffuse throughout the waveguide and eventually recombine with the holes. Denoting τ_{fc} as the lifetime of the FC, we can also write the equation for the FC density N(z, t) as

$$\frac{\partial N(z,t)}{\partial t} = -\frac{N(z,t)}{\tau_{fc}} + \gamma_{FCA} P^2(z,t) \tag{5.2}$$

where $\gamma_{FCA} = \beta_{TPA}/(2\hbar\omega A_{eff}^2)$. The last term on the right-hand side gives the FC generation rate by TPA process.

In general, the generated free carriers diffuse and recombine through a number of processes, each with its own characteristic lifetime. The chain of events occurring when a high-intensity optical signal is applied to the silicon waveguide can be described as follows. In the first few femtoseconds, the optical field generates electron-hole-pairs through the TPA process [99- 100]. Assuming that the optical signal excites the fundamental transverse electric (TE_0) mode of the waveguide, most of the optical power is concentrated near the center of the waveguide as shown in figure 5.1. As a result, the majority of the free carriers are generated in this region. The generated free carriers then begin to diffuse out toward the sidewalls of the waveguide where the FC density is much smaller. The direction of carrier diffusion in the waveguide is shown by the arrow in figure 5.1.

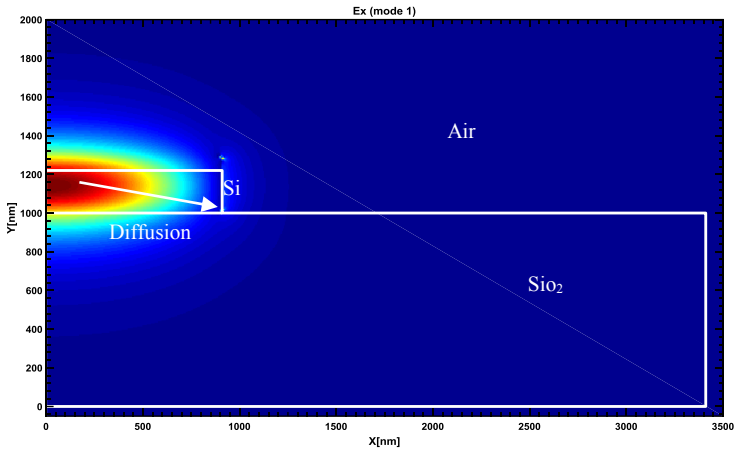

Figure 5. 1, Fundamental mode (TE0) distribution in cross section of the waveguide (only right half shown). The waveguide core had thickness H = 220 nm and width W = 1.82 µm, lying on a 1 µm-thick oxide layer with its top and sidewalls are exposed to air.

Depending on the location of the free carriers in the waveguide cross-section, they experience different nonradiative recombination mechanisms. Most free carriers recombine with surface states at the top and side walls of the waveguide, and also at its bottom interface with SiO_2. This is called surface/interface recombination (SIR) [101, 102]. The rate of SIR in a strip waveguide of width W and height H is given by

$$\frac{1}{\tau_{SIR}} = \frac{1}{\tau_b} + \frac{S}{H} + \frac{W + 2H}{W \times H} S' \qquad (5.3)$$

where S and S′ are the top and bottom surface recombination velocities, respectively, and τ_b is the bulk recombination lifetime. The surface recombination velocity for silicon waveguide highly depends on the fabrication technology and is reported to be between 10 m/s and 100 m/s [99].

Some carriers may undergo Shockley-Reed-Hall (SRH) recombination in the bulk silicon core before reaching the waveguide surface [101]. SRH is also known as defect recombination. A defect in the silicon crystalline structure introduces an energy state

within the bandgap of the material. A free electron can recombine with this state, with a probability (or recombination rate) determined by the distance of the energy level from either of the band edges. Recombination is more likely for energy levels near mid gap and becomes less likely for energy levels closer to either band edge. The SRH recombination rate highly depends on the band gap size and temperature [103, 104].

At high FC densities, another nonradiative recombination process called Auger recombination can also occur which involves three carriers. In this process, the energy released from the recombination of an electron-hole-pair is not transferred to a phonon but instead excites another free carrier to a higher energy level within the conduction band. This excited carrier then gives up its energy as a phonon and returns to the edge of the conduction band. Due to its involvement of three carriers, Auger recombination has a higher chance of occurrence in regions with high FC densities (high optical power) [105], leading to shorter FC lifetime in these regions [106]. The free carrier lifetime associated with Auger recombination is given by $\tau_{Aug} = (C_a N^2)^{-1}$ where C_a is the ambipolar Auger coefficient and N is the free carrier density. For lightly-doped silicon, the ambipolar Auger recombination coefficient is 3.79×10^{-43} m^6/s [106].

The effective FC lifetime in a silicon waveguide is due to SIR, SRH and Auger recombination, and can be expressed as,

$$\frac{1}{\tau_{fc}} = \frac{1}{\tau_{SRH}} + \frac{1}{\tau_{Aug}} + \frac{1}{\tau_{SIR}} \tag{5.4}$$

We can lump the SIR and SRH lifetimes, which do not depend on the FC density, into a single time constant τ_0, and rewrite equation (5.4) as

$$\frac{1}{\tau_{fc}} = \frac{1}{\tau_0} + C_a N^2 \tag{5.5}$$

Since the FC density depends on the optical power, it is evident from the above equation that the effective FC lifetime in a silicon waveguide is not a constant but depends on the power of the optical signal.

Using the expression for the effective FC lifetime in equation (5.5), we can express equation (5.2) for the time evolution of the FC density as

$$\frac{\partial N(z,t)}{\partial t} = -N(z,t)\left(\frac{1}{\tau_0} + C_a N^2(z,t)\right) + \gamma_{FCA} P^2(z,t) \tag{5.6}$$

5.1.1 Steady-state solutions

We first look at the solution to equations (5.1) and (5.6) under the steady-state condition, when an optical signal of constant optical power P_{bias} is applied to the waveguide. Setting the time derivative dN/dt = 0, we have

$$\frac{\partial P_{dc}(z)}{\partial z} = -\left(\alpha_0 + \frac{\beta_{TPA}}{A_{eff}} P_{dc}(z) + \sigma_{FCA} N_{dc}(z)\right) P_{dc}(z) \tag{5.7.a}$$

$$N_{dc}(z)\left(\frac{1}{\tau_0} + C_a N_{dc}^2(z)\right) = \gamma_{FCA} P_{dc}^2(z) \tag{5.7.b}$$

where $P_{dc}(z)$ and $N_{dc}(z)$ are the steady-state power and FC distributions along the waveguide. We can obtain the analytical solutions of equations (5.7) by ignoring Auger recombination as [107],

$$P_{dc}(z) = P_{bias} \frac{e^{-\alpha_0 z}}{\sqrt{1 + 2\sigma_{FCA}\tau_{fc}\gamma_{FCA} L_{eff}(z) P_{bias}^2}} \tag{5.8.a}$$

$$N_{dc}(z) = \tau_{fc}\gamma_{FCA} P_{dc}^2(z) \tag{5.8.b}$$

In equation (5.8.a), L_{eff} is the effective length of the waveguide due to linear loss [107],

$$L_{eff}(z) = \frac{1 - e^{-\alpha_0 z}}{\alpha_0} \tag{5.9}$$

We calculated the steady-state solutions for a sample silicon waveguide with similar dimensions to the one used in our experiment in section 5.3. The waveguide had thickness H = 220 nm, width W = 1.82 μm and length L_z = 5.3 mm. The silicon core lies on an oxide layer with 1 μm thickness and its top and sidewalls are exposed to air. The effective area of the fundamental TE mode at 1.55 μm wavelength is calculated to be $A_{eff} = 4.1\times10^{-13}$ m^2. The material parameters for silicon are α_0 = 5 $dB.cm^{-1}$, $\beta_{TPA} = 8\times10^{-11}$ $m\times W^{-1}$, and $\sigma_{FCA} = 1.45\times10^{-21}$ m^2 [82]. The free carrier lifetime associated with SRH and SIR (τ_0) of lightly doped SOI-waveguide is set to be 150 ns. This value was obtained from fitting simulation results to measurement data, as discussed in Section 5.3.

In figure 5.2 (a) we plot the steady-state power distribution along the waveguide for an input power of 50 mW in the presence of nonlinear loss due to FCA (red line). For comparison we also show the power distribution when only linear loss is present in the waveguide (black line). We observe that the effect of nonlinear loss is most pronounced near the input end of the waveguide, where the induced loss by FC is the largest. As the optical wave propagates along the waveguide, it experiences attenuation due to both linear and nonlinear losses. This power decay leads to decreasing free carrier generation by TPA along the waveguide, as confirmed by the plot of FC concentration vs. distance in figure 5.2 (b).

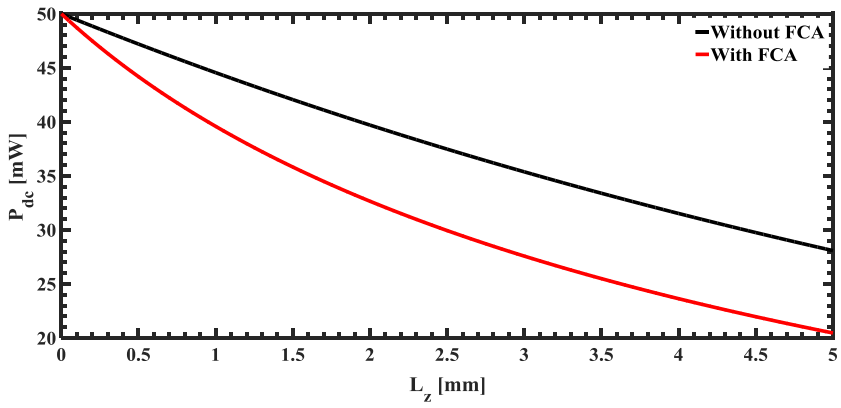

(a)

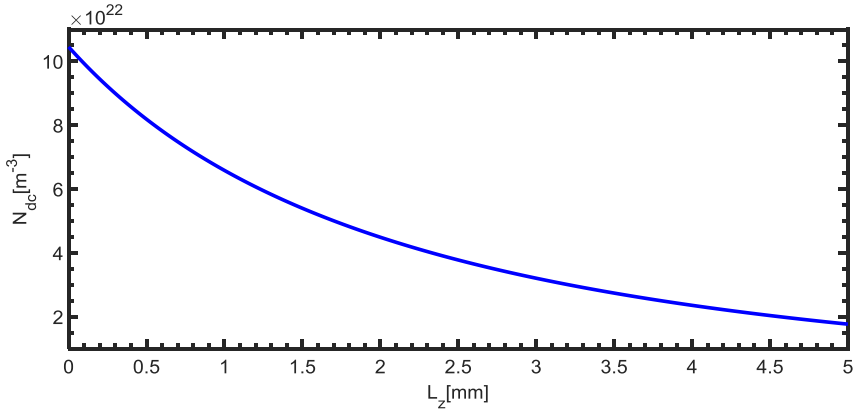

(b)

Figure 5.2, The Steady-state (a) power and (b) free carrier distribution along the SOI waveguide.

Figure 5.3 plots the transmitted power at the output of the 5.3 mm-long waveguide versus the input power in the absence (black line) and presence (red line) of nonlinear loss. We observe that the effect of nonlinear loss becomes more pronounced at higher input powers, as evident from the larger deviation between the two curves. To study the dependence of the transmitted power on the FC lifetime, we plot in figure 5.4 the output power versus the FC lifetime for a fixed input power of 50 mW. We observe that as the FC lifetime is increased, the FC density is also increased, which leads to a reduction in the output power.

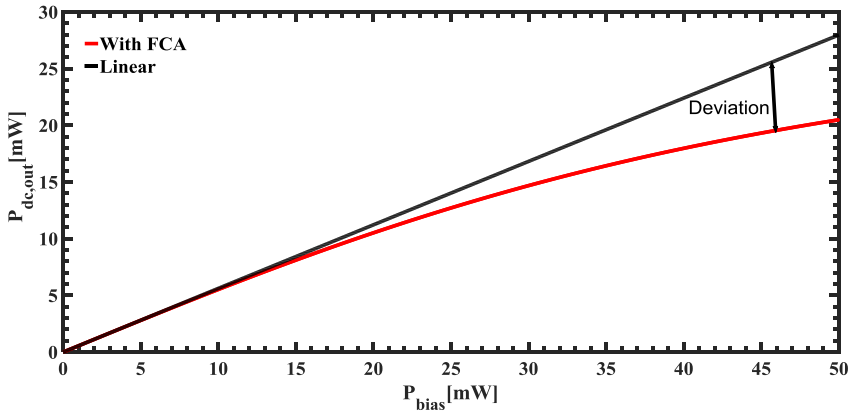

Figure 5.3, The steady-state output power versus input power for a 5.3 mm-long silicon waveguide in the presence (red line) and absence (black line) of nonlinear loss due to FCA

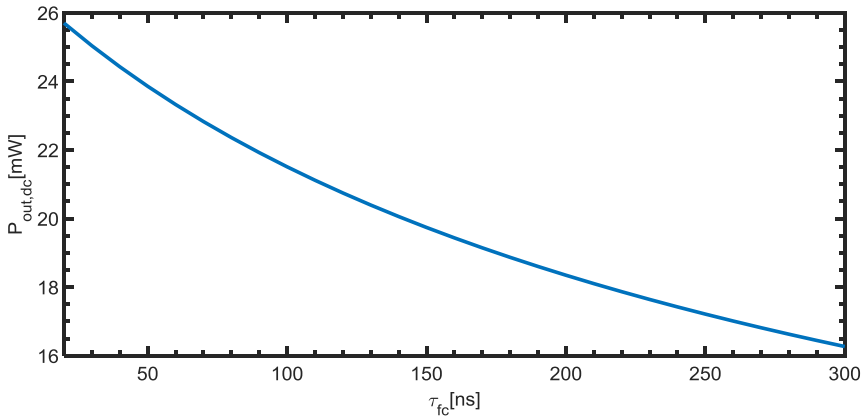

Figure 5.4, The steady-state output power versus free carrier lifetime for an input power of 50mW in a 5.3mm long silicon waveguide.

5.1.2 Transient solutions

To obtain the solutions to the coupled equations (5.1) and (5.2) to a time varying input power signal $P_{in}(t)$, we assume that the input power can be decomposed into a steady-state (DC) component and a small-signal transient (AC) component as $P_{in}(t) = P_{bias} + p_{in}(t)$. Similarly, we also separate the power and FC distributions in the waveguide into a DC part and a small-signal AC part as $P(z,t) = P_{dc}(z) + p(z,t)$ and $N(z,t) = N_{dc}(z) + n(z,t)$, respectively. Substituting these expressions into equations (5.1) and (5.2), we get

$$\frac{\partial\left(P_{dc}(z)+p(z,t)\right)}{\partial z}=-\left(\alpha_0+\frac{\beta_{TPA}}{A_{eff}}\left(P_{dc}(z)+p(z,t)\right)+\sigma_{FCA}\left(N_{dc}(z)+n(z,t)\right)\right)\times\left(P_{dc}(z)+p(z,t)\right) \tag{5.10.a}$$

$$\frac{\partial\left(N_{dc}(z)+n(z,t)\right)}{\partial t}=-\left(N_{dc}(z)+n(z,t)\right)\left(\frac{1}{\tau_0}+C_a\left(N_{dc}(z)+n(z,t)\right)^2\right)+\gamma_{FCA}\left(P_{dc}(z)+p(z,t)\right)^2 \tag{5.10.b}$$

The above equations can also be separated into a set of DC equations and a set of transient equations. The DC equations are the same as equations (5.7), whose solutions we have previously discussed. For the transient equations, we further simplify by neglecting high-order terms in p and n to obtain the system of coupled linear equations,

$$\frac{\partial p(z,t)}{\partial z}=-\left(\alpha_0+\sigma_{FCA}N_{dc}(z)\right)p(z,t)-\gamma_{FCA}P_{dc}(z)n(z,t) \tag{5.11.a}$$

$$\frac{\partial n(z,t)}{\partial t}=-\frac{n(z,t)}{\tau'_{fc}(z)}+2\gamma_{TPA}P_{dc}(z)p(z,t) \tag{5.11.b}$$

In the above equation, τ'_{fc} is the small-signal free carrier lifetime given by

$$\frac{1}{\tau'_{fc}(z)}=\frac{1}{\tau_0}+3C_aN_{dc}^2(z) \tag{5.12}$$

Equations (5.11.a) and (5.11.b) cannot be solved analytically. Instead, we resort to a semi-numerical method based on a time marching algorithm in which we discretize the time variable into small intervals of size Δt. Supposing that at time t, the solutions are given by p(z, t) and n(z, t). From equation (5.11.b), we obtain the time marching formula for the FC density at time $t + \Delta t$ as

$$n(z,t+\Delta t)=n(z,t)e^{-\frac{\Delta t}{\tau'_{fc}(z)}}+2\gamma_{TPA}\tau'_{fc}(z)\left(1-e^{-\frac{\Delta t}{\tau'_{fc}(z)}}\right)P_{dc}(z)p(z,t) \tag{5.13}$$

In the above analytical solution, we assumed that p(z,t) is constant in interval between t and $t+\Delta t$ because of its perturbative nature in comparison to $P_{dc}(z)$.

Next, the transient power distribution p(z, t + Δt) is updated using the expression

$$p(z,t+\Delta t)=\left(\Delta P-\gamma_{FCA}\int_0^z P_{dc}(z')e^{\left(\alpha_0 z'+\gamma_{FCA}\int_0^{z'} N_{dc}(z)dz\right)}n(z',t+\Delta t)dz'\right)e^{-\left(\alpha_0 z+\gamma_{FCA}\int_0^{z} N_{dc}(z')dz'\right)} \quad (5.14)$$

In the above equation, ΔP is the AC input power. At the initial time t = 0, the FC density is n(z, 0) = 0 and the power distribution is given by

$$p_{ac}(z,0)=\Delta P e^{-\left(\alpha_0 z+\sigma_{FCA}\int_0^{z} N_{dc}(z')dz'\right)} \quad (5.15)$$

In the next section we apply the above numerical method to simulate the nonlinear response of a silicon waveguide to step input and square wave optical signals

5.2 Numerical Simulations

In the following simulations, we use a silicon waveguide with the same dimensions and material parameters as described in Section 5.2.1.

5.2.1 Nonlinear response to a step input optical signal

We simulated the transient response of the transmitted power, $P_{out}(t)$, at the output of the waveguide for a step input signal of the form $P_{in}(t)=P_{bias}+\Delta P u(t)$, where P_{bias} is a constant bias power, ΔP is the step change in power and u(t) is the Heaviside function. The time responses of the transmitted power and the FC density at the input end of the waveguide are shown in figure 5.5 for a sample input signal with P_{bias} = 50 mW and ΔP = 1 mW. We observe that the output power becomes attenuated as free carriers are generated in the waveguide. However, due to the coupling dynamics between the FC

density and the optical power, the transient responses of both the output power and the FC density generally do not follow a pure exponential behavior with a fixed time constant. It is also evident from the plot that the relaxation times of the power and FC density are not the same.

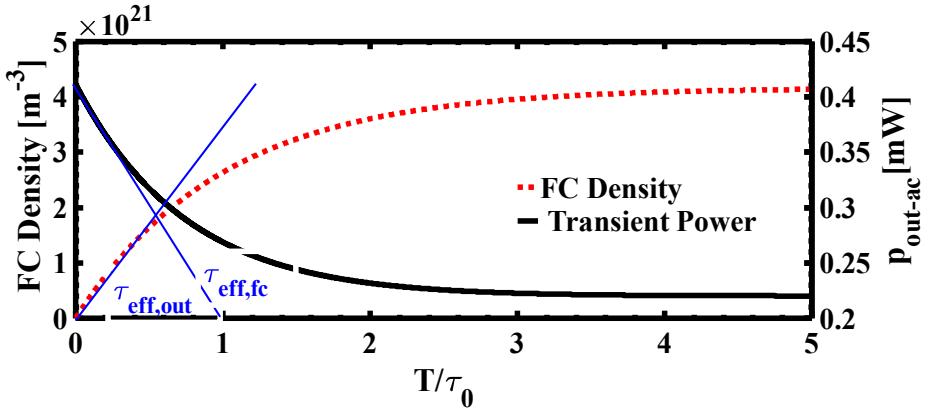

Figure 5.5, Simulated transient responses of the output power and the FC density at the waveguide input for a step input signal with P_{bias} = 50 mW and ΔP = 1 mW

Nevertheless, we can quantify the rate of decay of each curve by defining an effective time constant τ_{eff} as the initial decay constant of the transient response just after the input step change. For the results in figure 5.5, we obtain the effective time constants for the output power and FC density to be $\tau_{eff,out} = 0.74\tau_o$ and $\tau_{eff,fc} = 0.99\tau_o$, respectively, which indicates that the output power has a faster decay rate than the FC density.

Since the input bias power determines the level of FC density generated in the waveguide and hence the magnitude of the FC-induced nonlinear loss, we expect it to also have a direct impact on the relaxation time of the transient response. Figure 5.6 shows the dependence of the normalized effective time constant of the output power ($\tau_{eff,out}/\tau_o$) and the FC density ($\tau_{eff,fc}/\tau_o$) on the bias power (P_{bias}) with the step change ΔP fixed at 1 mW. Below about 10 mW (region I), the FC density and output power have roughly the same

relaxation time, which is approximately equal to the lifetime τ_o. Between 10 mW and 50 mW (region II), the effective decay time of the output power decreases noticeably as the bias power increases. However, the effective FC lifetime remains relatively constant in this region and only begins to drop when P_{bias} exceeds 50 mW (region III).

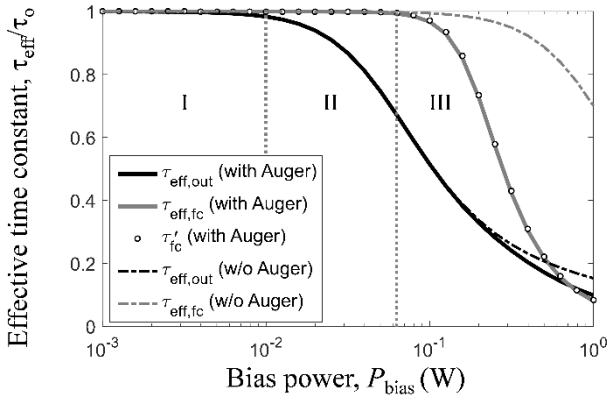

Figure 5.6, Dependence of the effective decay time of the output power and the effective FC lifetime on the input bias power (at a fixed step power change ΔP = 1 mW).

To understand the cause for the decrease in the decay times, we show in the plot the small-signal FC lifetime (open circles), which is seen to be nearly identical to the effective lifetime of the FC density, as may be expected from equation (5.12). Notably, the small-signal FC lifetime begins to exhibit a sharp drop-off at $P_{bias} \sim 50$ mW due to Auger recombination. However, in region II, the effect of Auger recombination is negligible but the effective decay time of the output power still shows a steep drop with the bias power. We attribute the reduction in the decay time of the output power in this region to the interaction between the FC population and the optical intensity in the waveguide. To gain further understanding of the effect of Auger recombination, we also plot in figure 5.6 the simulation results without Auger recombination (dotted curves). We observe that the results with and without Auger recombination begin to deviate from

each other for input bias powers greater than 50 mW, indicating again that Auger recombination becomes non-negligible at high powers. Finally we note that the reduction in the effective decay times is also observed if we increase the step power change ΔP of the input signal instead of the bias power level.

The dependence of the decay times on the power level suggests that care must be taken when determining the FC lifetime in a silicon waveguide from the relaxation time of the transmitted power. On the one hand, it is desirable to use a high input power in such a measurement so that the FC-induced power attenuation is large, making it easier to measure the decay time constant. On the other hand, a high input power may cause the FC lifetime to be underestimated. As shown by the simulation results in figure 5.6, the decay time of the transmitted power can be much shorter than the FC lifetime in the waveguide at moderate input powers. This result also suggests that it may be possible to perform all-optical switching in a silicon waveguide at speeds faster than the FC relaxation rate.

5.2.2 Nonlinear response to a square wave optical signal

In this section we investigate the nonlinear response of a silicon waveguide to an input pulse train with duty cycle D and modulation frequency $F_{modulation}$. The power levels of the signal during the on interval (T_{On}) and off interval (T_{Off}) are P_{On} and P_{Off}, respectively. The duty cycle of the pulse train is defined as $D = T_{On}/(T_{On} + T_{Off})$. To study the effect of the optical power on the effective FC lifetime and power decay rate, we apply two pulse trains with different bias levels of 35 mW and 130 mW, respectively. The pulse height of both inputs is 20 mW. Thus for the low-power signal, $P_{Off} = 35$ mW

and P_{On} = 55 mW, whereas for the high-power signal, P_{Off} = 130 mW and P_{On} = 150 mW. The modulation frequency is 1 MHz and the duty cycle is fixed at 70%. Figures 5.7(a) and (b) show the temporal profiles of the transmitted powers (solid lines) and the free carrier densities (dashed lines) at the output of the waveguide for the low-power and high-power input signals, respectively. We observe that during the On interval, the optical power is absorbed to generate free carriers so the transmission decreases. The reduction of the power in the waveguide due to nonlinear loss, however, eventually leads to a decrease in the FC density. During the Off interval, the drop in the optical power causes a fall-off in the density of the free carriers as they recombine. The decrease in the FC density is accompanied by a corresponding increase in the power transmission in the Off interval.

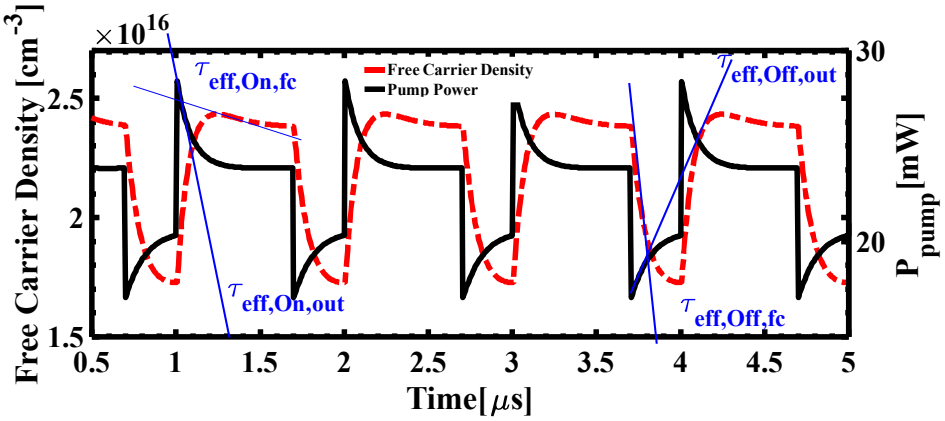

(a)

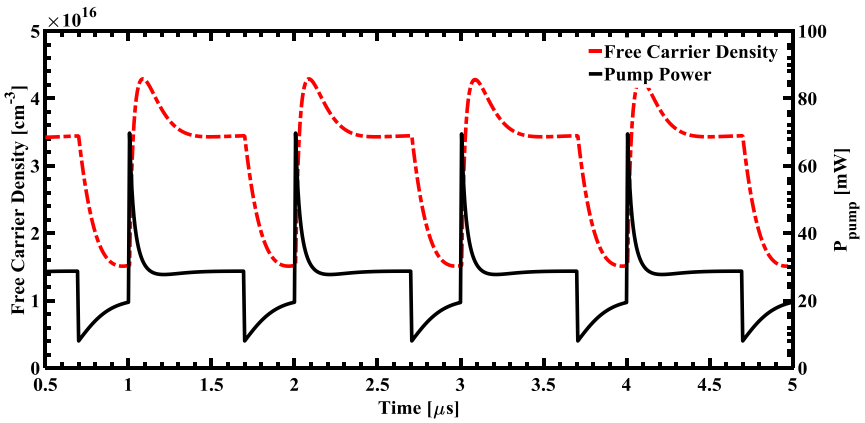

(b)

Figure 5.7, The time trace of power and free carrier density at the output of waveguide for bias level of (a) 35mW and (b) 130mW

To quantify the rise times and fall times of the transmitted power and FC density, we define the effective FC lifetimes during the Off and On intervals as $\tau_{eff,Off,fc}$ and $\tau_{eff,On,fc}$, respectively, and the effective power decay times as $\tau_{eff,Off,PWR}$ and $\tau_{eff,On,PWR}$, respectively, as shown in figure 5.7(a). The values for these time constants are obtained from the plots and tabulated in table 5.1. It is evident from the table that the time constants for both the FC density and the transmitted power are smaller at the higher input power (i.e., the rise times are shorter than the fall times), indicating that the time constants are dependent on the input power. These results correlate with the results from the step-input analysis of figure 5.5.

Table 5.1, The effective power decay and free carrier generation rate for various power levels and intervals

Input power	Interval	variable	value
		$\tau_{eff,Off,out}$	107 ns
		$\tau_{eff,Off,fc}$	94 ns
		$\tau_{eff,On,out}$	93.4 ns
		$\tau_{eff,On,fc}$	73.4 ns
		$\tau_{eff,Off,out}$	60.3 ns
		$\tau_{eff,Off,fc}$	33.33 ns

	On	$\tau_{eff,On,out}$	53.4 ns
		$\tau_{eff,On,fc}$	26.7 ns

To study the variation of the effective time constants with the modulation frequency of the input signal, we applied a square wave to the silicon waveguide with the modulation frequency varied from 1 MHz to 100 MHz. The input signals have a fixed bias power P_{bias} = 50 mW, step height ΔP = 20 mW and duty cycle D = 70%. Figure 5.8 shows the plot of the average power transmission as a function of modulation frequency.

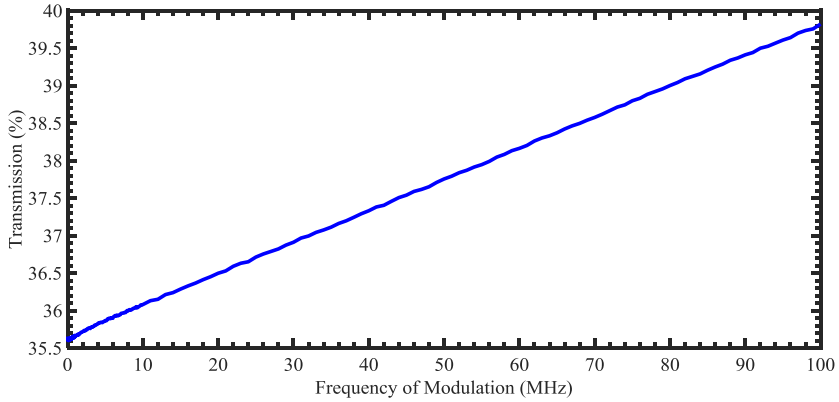

Figure 5.8, Average transmission ratio as a function of frequency of modulation

The average transmission is computed as

$$\text{Transmission} = \frac{\int_0^T P(z = L_z, t)dt}{\int_0^T P(z = 0, t)dt} \tag{5.16}$$

In the above equation, T is the period of the square wave and L_z = 5.3 mm is the waveguide length. Increasing the modulation frequency reduces the durations of the on and off intervals. As a result, smaller FC densities are generated during the on intervals, leading to lower nonlinear absorption in the waveguide. Thus, we observe from the figure 5.8 that the average transmission of the silicon waveguide increases with

increasing modulation frequency.

We also studied the variation of the effective time constants with the duty cycle D. Figure 5.9 plots the average power transmission as a function of the duty cycle for a square pulse train with modulation frequency of 1MHz, bias power level P_{bias} = 50 mW, and step height ΔP = 20 mW. We observe that the average transmission decreases with increasing duty cycle. As the duty cycle is increased (i.e., the ratio of the On interval to Off interval is increased), the density of free carriers generated during the On intervals increases while fewer free carriers are recombined in the Off intervals.

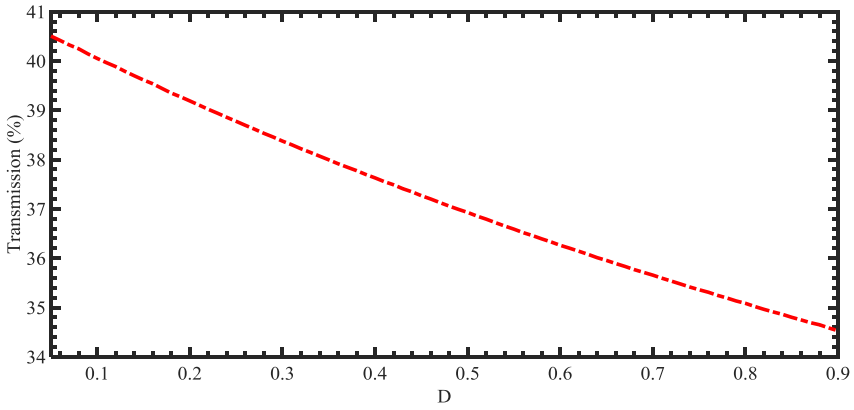

Figure 5.9, Average transmission ratio as a function of Duty Cycle for a 1MHz modulation frequency

As a result, the optical pulses experience more nonlinear absorption, leading to a decrease in the average power transmission, as observed in the plot.

5.3 Experimental Validation

In this Section we report our experimental work to validate the simulation results obtained in the previous section. We will first describe the silicon waveguide used in the experiment and the experimental setup used to perform time-domain measurements of the power transmission of the waveguide. Experimental results will then be presented and

compared to the simulation results.

5.3.1 Silicon-on-Insulator waveguide

The Silicon-on-Insulator (SOI) waveguide used in our study has a silicon core of 220 nm thickness and 1.82 μm width. The waveguide lies on a 1 μm-thick oxide layer with the top and sidewalls exposed to air. The effective area of the transverse electric (TE) mode at 1.55 μm wavelength is calculated to be $A_{eff} = 4.1\times10^{-13}$ m^2 and the total waveguide length is 5.3 mm. A diagram and SEM image of this waveguide is shown in figure 5.10 (a) and 5.10 (b), respectively.

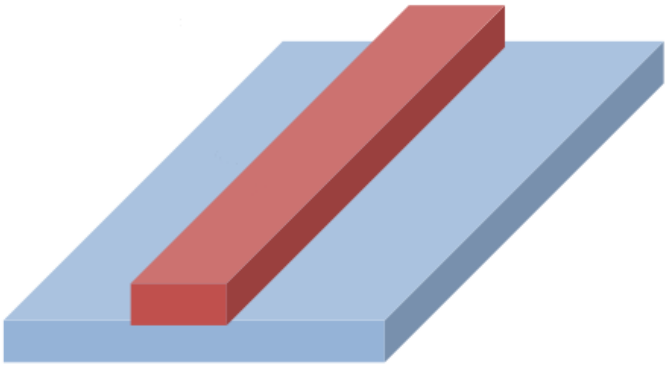

(a)

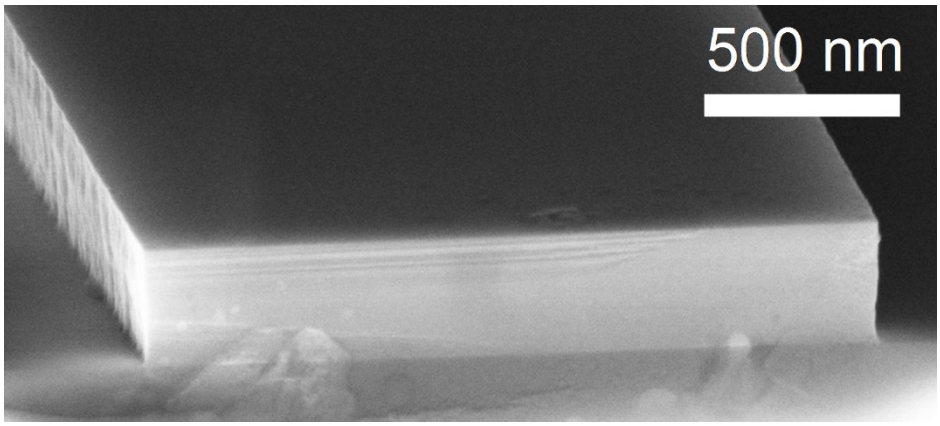

(b)

Figure 5.10, (a) A diagram of the waveguide. (b) an SEM image of the fabricated waveguide

The waveguide was fabricated in the University of Alberta Nanofabrication Facility. The procedure used to fabricate the waveguide is summarized in Appendix I.

5.3.2 Experimental setup

Figure 5.11 shows the experimental setup used to measure the transient response of the transmitted power of the silicon waveguide. In the experiment, we modulated a CW optical signal at the 1.55 μm wavelength from a tunable laser using a 40 Gbps intensity modulator. The CW signal had a power level of 25 mW (14.1dBm). We biased the modulator to V_π = 2.5 V from a DC power supply (V_π is called the half-wave voltage, which is the voltage required to induce a π phase shift in the modulator).

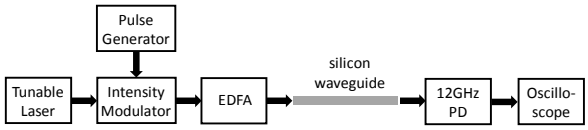

Figure 5.11, Schematic of the experimental setup used to measure the transient response of the transmitted power of a silicon waveguide for an input square wave.

A microwave arbitrary waveform generator (AFG3000) provided a square wave with peak-to-peak amplitude of 2.5 V to the intensity modulator. We then amplified the modulated optical signal with a DC-Erbium-doped fiber amplifier (EDFA). The amplification step provided by the EDFA is 10 mW with a maximum output power of 2 W.

To excite the TE mode of the silicon waveguide, we passed the modulated and amplified optical signal through a polarization controller to select the TE polarization. The light was then butt-coupled to the silicon waveguide using a lensed fiber. The transmitted

power is detected by a high-speed photodetector (12 GHz bandwidth) and the output time trace is recorded on an oscilloscope. In the experiment, we set the pulse repetition rate (or modulation frequency) of the signal generator to 1 MHz and the duty cycle to be D = 70%. By changing the power level of the EDFA, we could vary the power level of the input optical signal. Figures 5.12 (a) and (b) show the time traces of the transmitted powers of the silicon waveguide for two different input power levels. Excluding input coupling loss, the values for the bias power and step change of the input square waves were P_{bias} = 50 mW, ΔP = 20 mW (P_{Off} = 50 mW and P_{On} = 70 mW) for figure 5.12(a) and P_{bias} = 130 mW, ΔP = 20 mW (P_{Off} = 130 mW and P_{On} = 150 mW) for figure 5.12(b).

To extract $\tau_{eff,On}$ and $\tau_{eff,Off}$ values from experimental data we performed curve fitting to the function $f(t) = a + be^{-\frac{t}{\tau_{eff}}}$ where a, b, and τ are determined by least square method (L:SM). The values of a, b, and τ_{eff} are different for on and off intervals.

For the trace in figure 5.12(a), the effective time constants obtained from the output power response are $\tau_{eff,On}$ = 98 ns during the high-power (On) interval and $\tau_{eff,Off}$ = 115 ns during the low-power (Off) interval.

For the trace in figure 5.12(b), the corresponding values are $\tau_{eff,On}$ = 55 ns and $\tau_{eff,Off}$ = 72 ns. It is evident that the effective time constants are reduced at the higher bias power, by as much as 60% compared to those at the lower bias power. We note that the On and Off effective time constants are not equal because they depend on the FC concentration in the waveguide before the On or Off step change occurs.

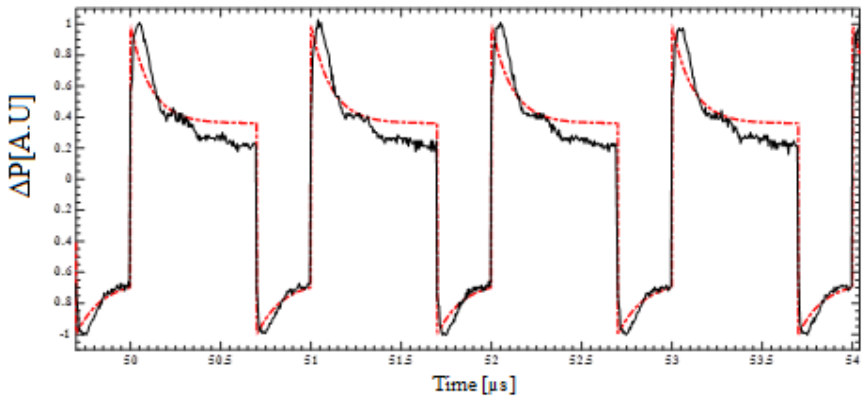

(a)

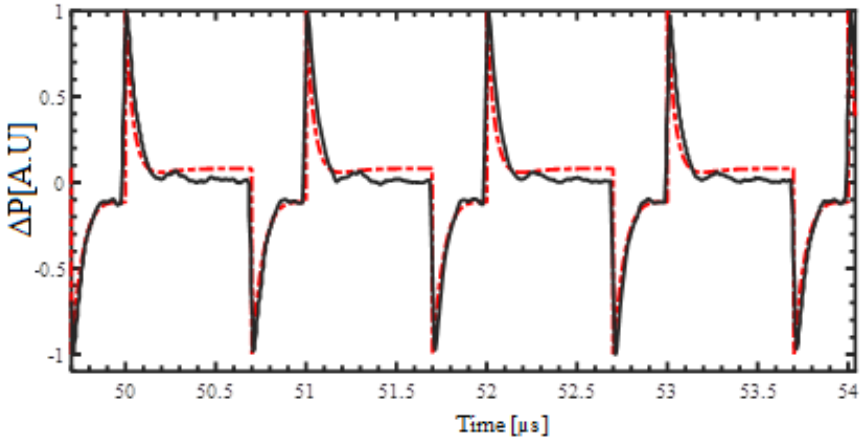

(b)

Figure 5.12, Measured (grey dots) and simulated (dashed line) transient responses of the transmitted power for a 1 MHz input square wave with (a) low bias power (P_{bias} = 35 mW, ΔP = 20 mW) and (b) high bias power (P_{bias} = 130 mW, ΔP = 20 mW).

To compare the measurement results with the results predicted by the model in equation (5.7), we performed numerical simulation of the silicon waveguide with the linear loss α_0 and the Auger-independent FC lifetime τ_0 optimized to obtain a good fit between the simulated and measured transmitted powers. The linear and nonlinear parameters of the SOI waveguide used in the simulation are listed in table 5.2. The Auger-independent FC lifetime value τ_o is 150 ns, which is larger than the typical lifetime in SOI waveguides because of the large width of our waveguide. It may also be due to the low surface

recombination velocities associated with the surfaces and Si/SiO_2 interface of our SOI waveguide since it is known that this parameter varies widely depending on the method of interface formation and surface treatment [104, 107]. On the other hand, the small SIR rate allows the effect of Auger recombination to be observed at lower powers.

Table 5.2, Linear and nonlinear parameters of SOI waveguide

Coefficient	Expression	Value	Dimension
α_0	Linear Loss	5	[dB/cm]
β_{TPA}	Two Photon Absorption	1.2×10^{-11}	$[m.W^{-1}]$
A_{eff}	Effective Area	0.41×10^{-12}	$[m^{-2}]$
τ_0	Auger independent free carrier lifetime	150	[ns]
Ca	Ambipolar Auger coefficient	3.79×10^{-43}	$[m^6/sec]$
σ_{FCA}	Free carrier Dispersion Cross Area	1.4×10^{-21}	$[m^{-2}]$
λ	wavelength	1.55	[μm]
ΔP	Step power	20	[mW]
L_z	Waveguide Length	5.3	[mm]

Since the measured time trace recorded by the high-speed photodetector only contains the transient (AC) component, we removed the DC part from the simulated output power to obtain the AC component as follows:

$$P_{out\_ac}(t) = P(L_z, t) - \frac{1}{T}\int_0^T P(L_z, t)dt \qquad (5.17)$$

The simulated results are shown by the dashed lines in figures 5.12(a) and (b) for both input power levels, showing excellent agreement with the measurement results.

We also studied the variation of the effective decay time with the frequency of the input signal. We applied a square wave to the silicon waveguide with bias power P_{bias} = 130 mW and step height ΔP = 20 mW. The duty cycle was fixed at 70% and the modulation

frequency was varied from 1 MHz to 10 MHz with 1 MHz step. By changing the repetition frequency of modulator (between 1MHz to 10 MHz), the DC value of modulated optical signal varies and we should modify the V_π in each step to have a consistent DC part during the entire experiment for the frequency range from 1MHz to 10MHz.

A sample measured transient response for a 4 MHz input square wave is shown in figure 5.13. Also shown is the simulated curve, which was obtained using the same parameters in Table 5.2 except for the frequency change.

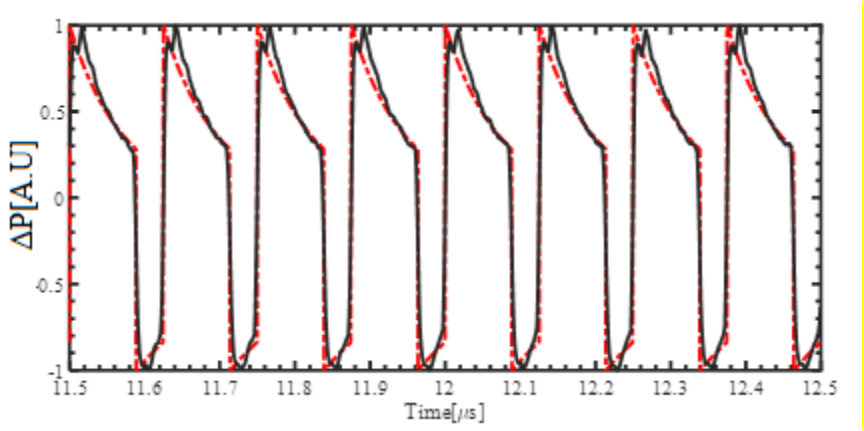

Figure 5.13, Measured and simulated time responses of the output power for a 4 MHz in square wave with P_{bias} = 130 mW and pulse height of 20 mW

In figure 5.14 we plot the measured effective time constant during the on interval of the output power versus the frequency. The values predicted by the model are also plotted, showing that the decay time increases only slightly with frequency.

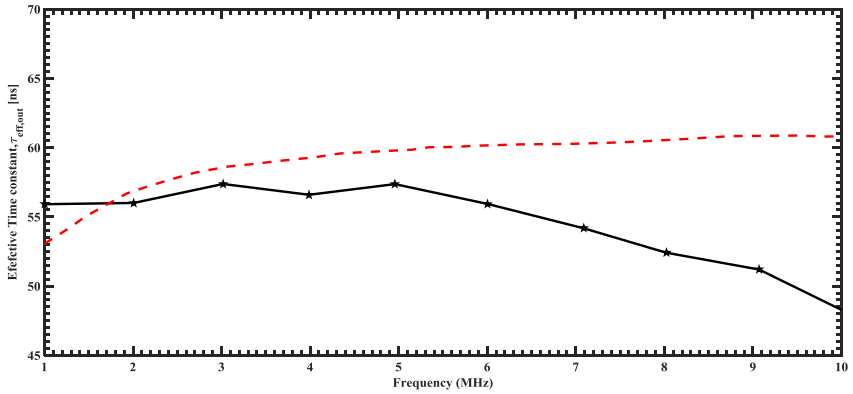

Figure 5.14, Plot of the measured (solid line) and simulated (dashed line) effective time constant of the output power versus the modulation frequency

Although the data for the measured time constant exhibit large variations ~~with simulation result~~ due to limited band width of oscilloscope (1MHz), they can be seen to be roughly in the same range of values as the simulation result.

5.4 Summary

In this chapter we reported a detailed analysis, through numerical simulations and experimental validation, of the effect of the FC lifetime on the transient response of the optical power in a silicon waveguide. Our model includes contributions to the FC lifetime from both surface/interface recombination and Auger recombination, the latter of which becomes important at high powers. We found that in general the output power exhibits a shorter decay time than the FC lifetime, and this decay time decreases with increasing input powers. Furthermore, the reduction in the decay time occurs well below the power levels at which Auger recombination becomes important, and is attributed to the coupling dynamics between the optical intensity and the FC population in the waveguide. This result could have implications for nonlinear optics applications of silicon waveguides, such as the possibility of performing all-optical switching and

modulation at speeds exceeding the limit set by the FC lifetime. As a validation to the model used, we also performed measurement of the transmitted power of a silicon waveguide for different input powers and frequencies, with the results obtained showing excellent agreement to simulations.

6 Conclusions

6.1 Summary of research contributions

In this thesis we investigated the nonlinear dynamics of single microrings and systems of coupled microring resonators. In addition to the interesting fundamental physics that these systems entail, they can also have potential applications in high-frequency optical clock generation and optical pulse generation. In particular, we studied self-pulsation behaviours in resonators with instantaneous nonlinearity where the nonlinear response time of the material is much shorter than the cavity roundtrip time, and in resonators with non-instantaneous nonlinearity where the nonlinear response time is longer than the roundtrip time. A specific example of instantaneous nonlinearity considered in the thesis is Kerr nonlinearity in chalcogenide glass. For resonators with non-instantaneous nonlinearity, we considered semiconductor materials such as silicon, where the nonlinear response is due to free carriers generated by two-photon absorption. For each type of nonlinearity, we developed models to analyze the nonlinear dynamic behaviours of single microrings and systems of coupled microrings, with the aim of understanding the mechanisms giving rise to instability and reducing the threshold powers required to achieve self-pulsation in practical integrated photonic devices.

In Chapter 2, we reviewed the EC and PC models for analyzing the stability of a microring resonator with instantaneous Kerr nonlinearity. Since the EC model is valid only for a narrow frequency range around a single resonance mode of the microring, it

cannot predict Ikeda instability, which relies on the mixing of adjacent resonator modes. On the other hand, the PC model accounts for an infinite number of resonance modes and can thus predict Ikeda instability and multistability phenomena in a single resonator. This observation motivated us to develop a PC model to study the nonlinear dynamics of a single MRR with non-instantaneous nonlinearity. The model allowed us to investigate, for the first time, higher-order SP behaviours in a silicon MRR with FC-induced nonlinearity. In particular, we showed that 2^{nd}-order SP can be achieved for much longer FC lifetimes than possible with 1^{st}-order SP, and the range of oscillation frequencies is also wider. We also proposed two alternative techniques for reaching SP on the second branch of the stability curve without requiring prohibitively high CW optical powers. The first technique is based on tuning the linear phase of the microring over more than one FSR, while the second technique is based on applying an ultrafast optical pulse with high peak power to overcome the bistability knee. These methods can potentially allow for the experimental observation of high-order SP in silicon microring resonators, leading to practical integrated optics devices for generating high-frequency optical clock signals on a silicon chip.

In Chapter 3, we extended the analysis of nonlinear dynamics to a system of coupled MRRs with the aim of lowering the threshold powers for reaching SP. Again we considered both systems with instantaneous Kerr type nonlinearity and FC-induced nonlinearity with finite relaxation time. A significant contribution arising from this study is that by using the PC formalism, we showed for the first time that Ikeda instability also exists in a system of coupled MRRs with instantaneous Kerr nonlinearity. In addition, for specific design parameters, we could achieve minimum threshold powers for SP with

four coupled MRRs. However, the threshold power for observing Ikeda instability in a chain of coupled MRRs is found to be higher than for a single MRR since the input power is distributed over many resonators.

Our work on the nonlinear dynamics of a chain of coupled MRRs led us to formulate an alternative description of such a system as a Coupled Map Lattice in Chapter 4. The CML formalism allows us to study the spatiotemporal distribution of the optical power in long nonlinear CMRR chains. It is well known that spatiotemporal patterns can form in a 1D CML system with gain. However, since the nonlinear CROW waveguides we studied do not have gain, the CML formalism only predicts temporal instabilities such as SP and Ikeda instability in these structures. On the other hand, by introducing a small gain in each microring in the chain, we showed that much richer spatiotemporal behaviours can exist in the CROW waveguide, such as quasi-periodic spatial pattern formations (i.e., spatial instability) and chaotic spatiotemporal behaviours. These structures can potentially have applications in quasi-periodic and random sequence generations.

In silicon photonic devices, free carriers generated by TPA provide the dominant source of nonlinearity, which can be exploited to achieve SP in single and coupled MRRs, as we showed in Chapters 2 and 3. In these devices, the FC lifetime is a critical parameter which affects the onset of SP. Given the important role of the FC lifetime in the nonlinear dynamics of silicon photonic devices (as well as other nonlinear processes such as four-wave mixing [108] and Raman gain [107]), we devoted Chapter 5 to the theoretical modeling and experimental study of the effect of the FC lifetime on the nonlinear relaxation of light propagation in a silicon waveguide, especially at moderate to

high powers where Auger recombination becomes significant. We showed that contrary to the usual assumption, the FC lifetime is generally different from the decay time of the optical intensity, and this decay time is not constant but depends on the optical power. In particular, we find that the effective decay time constant of the optical signal is significantly reduced at high input powers. This result could have implications for nonlinear optics applications of silicon waveguides, such as the possibility of performing all-optical switching and modulation at speeds exceeding the conventional limit set by the FC lifetime.

Our research contributions have been published in the following journal articles:

1. Siamak Abdollahi and Vien Van, "**Analysis of optical instability in coupled microring resonators,**" J. Opt. Soc. Am. B 31, 3081-3087 (2014)

2. Siamak Abdollahi and Vien Van, " **Free-Carrier-Induced Nonlinear Relaxation in a Silicon Waveguide**," IEEE Photonics Technology Letters, 29, 1112-1115 (2017)

3. Siamak Abdollahi and Vien Van, " **Free carrier induced high-order instability in an optical microcavity**," J. Opt. Soc. Am. B (2017)

6.2 Suggested directions for future research

The results obtained from our theoretical studies of instability in nonlinear MRRs in this thesis provide directions for achieving experimental demonstrations of these phenomena in practical integrated photonic devices. We list below suggested future research directions that can help further our understanding of the nonlinear dynamics of CMRR

systems and bring their practical applications closer to reality.

- Experimental demonstration of 2nd-order instability in silicon MRRs:

  Using the PC model developed in Chapter 2 for analyzing instability in an MRR with FC-induced nonlinearity, we can optimize parameters of silicon MRR such as waveguide width, ring size, Q factor to achieve minimum threshold power for observing SP on the 2nd branch. The device can then be fabricated and experiments based on the linear phase tuning technique proposed in Section 2.2.5 performed to demonstrate 2nd-order SP and the generation of high-frequency optical clock signals.

- Experimental demonstration of instability in nonlinear CROWs:

  Using the PC model developed in Chapter 3 for analyzing instability in nonlinear CROWs, we can optimize silicon CROWs of various lengths, coupling parameters, etc. to reduce the threshold powers for observing SP to practical levels. The devices can then be fabricated and experiments performed to demonstrate SP in nonlinear CROWs for fast optical pulse generation.

- Lyapunov stability analysis of CROW waveguide:

  The stability analysis performed in this thesis is based on the linearization of nonlinear coupled equations. Nonlinear stability analysis known as Lyapunov analysis can provide deeper insight into the nature of the nonlinear dynamics. For example chaotic dynamic behaviour could be detected only by Lyapunov stability analysis. Nonlinear Lyapunov analysis could enable us to design CMRRs for

novel applications in cryptography, signal processing and optical communication.

APPENDIX I

We listed the steps to fabricate SOI waveguide in figure A.1

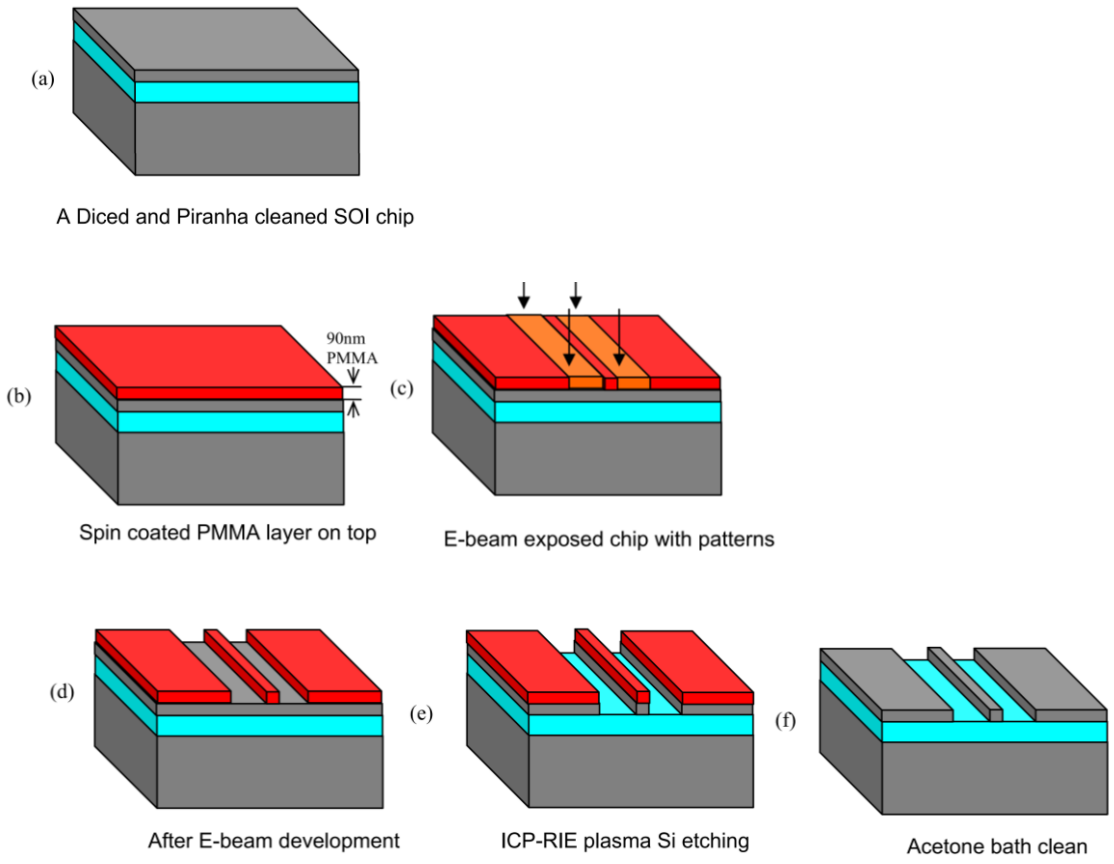

Figure A. 1, Silicon-on-insulator fabrication process for realizing [109]

(a) Dicing: The first step for fabrication of SOI waveguide is to cut up a 4" SOI wafer into 1×1 cm^2 chips using a wafer dicer. We should immerse the individual chips to an ultrasonic bath to clean the debris and dusts.

(b) Piranha clean: For additional cleaning the chips surface from organic remains, for about 15 minutes, we should immerse the chip into a Piranha solution. After Piranha cleaning step, we removed the surface moisture by washing with de-ionized water

and we finish this stage by nitrogen blow drying. The diced and cleaned chip is illustrated in figure A.1 (a).

(c) Resist coating: In the next step, we coat a layer of the electron beam lithography resist onto the chip by a resist spinner. We prebaked the chip at 100C on the hot plate to remove any surface moisture. After prebaking, we performed speed coating for 40 second at 4000 rpm. As illustrated in figure 1.A (b), the resist layer thickness was measured to be about 90 nm. We performed additional post baking for approximately 10 minutes at 180 ^{o}C, to remove any residual solvent from the resist.

(d) Electron beam lithography (EBL): The electron beam lithography system used to fabricate the waveguide is the 30 kV Raith 150 system. Unlike UV lithography system, Electron beam lithography can produce high resolution pattern which allows writing a pattern with 1nm resolution. Exposed resist to EBL is shown by figure A.1 (c).

(e) Resist development: PMMA (poly methyl methacrylate) is a polymeric material that is commonly used as a high resolution positive resist for EBL. Because PMMA is a positive EBL resist, the exposed portion of the resist becomes soluble to the resist developer. After an EBL exposure, the resist was developed in developer solution. Finally, we performed Nitrogen blow drying to eliminate any moisture. In figure A.1 (d), we showed the chip at the end of this stage.

(f) Reactive Ion etching (ICP-RIE): To remove material deposited on wafers, RIE uses chemically reactive plasma. This plasma is generated under low pressure (vacuum). The High-energy ions attack the wafer surface and react with it. The ICP-

RIE procedure shown by figure A.1 (e).

(g) Post-etch processing: Under ultrasonic vibrations in acetone bath, we removed the residual of resist. The final chip illustrated in figure A.1 (f). At the last stage, we cleaved the device to expose the waveguide facets for butt-coupling configuration. The facet of the cleaved waveguide facet is shown by figure 5.10

7 Bibliography

[1] He, Guang S., and Song H. Liu. *Physics of nonlinear optics*. World Scientific Publishing Co Inc, 1999.

[2] Franken, E. P., Hill, A. E., Peters, C. E., & Weinreich, G. "Generation of optical harmonics, " Physical Review Letters, 7(4), 118, 1961.

[3] Yin, Lianghong. "Study of nonlinear optical effects in silicon waveguides." PhD diss., University of Rochester, 2009.

[4] Aguinaldo, Ryan Francis. "Silicon Photonics with Applications to Data Center Networks." (2014).

[5] Del'Haye, P., A. Schliesser, O. Arcizet, T. Wilken, R. Holzwarth, and T. J. Kippenberg. "Optical frequency comb generation from a monolithic microresonator." Nature 450, no. 7173 (2007): 1214-1217..

[6] Basak, Juthika, Ling Liao, Ansheng Liu, Doron Rubin, Yoel Chetrit, Hat Nguyen, Dean Samara-Rubio, Rami Cohen, Nahum Izhaky, and Mario Paniccia. "Developments in gigascale silicon optical modulators using free carrier dispersion mechanisms." *Advances in Optical Technologies* 2008 (2008).

[7] Soref, Richard, and Brian. Bennett. "Electrooptical effects in silicon." *IEEE journal of quantum electronics* 23, no. 1 (1987): 123-129.

[8] Abdollahi, Siamak, and Mohammad Kazem Moravvej-Farshi. "Effects of heat

induced by two-photon absorption and free-carrier absorption in silicon-on-insulator nanowaveguides operating as all-optical wavelength converters." *Applied optics* 48, no. 13 (2009): 2505-2514.

[9] Turner-Foster, Amy C., Mark A. Foster, Jacob S. Levy, Carl B. Poitras, Reza Salem, Alexander L. Gaeta, and Michal Lipson. "Ultrashort free-carrier lifetime in low-loss silicon Nano waveguides." *Optics express* 18, no. 4 (2010): 3582-3591.

[10] Eggleton, Benjamin J., Barry Luther-Davies, and Kathleen Richardson. "Chalcogenide photonics." *Nature photonics* 5, no. 3 (2011): 141-148.

[11] Tsang, H. K., C. S. Wong, T. K. Liang, I. E. Day, S. W. Roberts, A. Harpin, J. Drake, and M. Asghari. "Optical dispersion, two-photon absorption and self-phase modulation in silicon waveguides at 1.55 μm wavelength." *Applied Physics Letters* 80, no. 3 (2002): 416-418.

[12] Ta'eed, Vahid G., Michael RE Lamont, David J. Moss, Benjamin J. Eggleton, Duk-Yong Choi, Steve Madden, and Barry Luther-Davies. "All optical wavelength conversion via cross phase modulation in chalcogenide glass rib waveguides." *Optics express* 14, no. 23 (2006): 11242-11247.

[13] Bloembergen, Nicolaas. Nonlinear optics. World Scientific, 1996.

[14] Chen, Shaowu, Libin Zhang, Yonghao Fei, and Tongtong Cao. "Bistability and self-pulsation phenomena in silicon microring resonators based on nonlinear optical effects." *Optics express* 20, no. 7 (2012): 7454-7468.

[15] Ikeda, Kensuke. "Multiple-valued stationary state and its instability of the transmitted light by a ring cavity system." *Optics communications* 30, no. 2 (1979): 257-261.

[16] Amiri, Iraj Sadegh, R. Ahsan, Ali Shahidinejad, Jalil Ali, and Preecha P. Yupapin. "Characterization of bifurcation and chaos in silicon microring resonator." *IET Communications* 6, no. 16 (2012): 2671-2675.

[17] Povinelli, Michelle L., Marko Lončar, Mihai Ibanescu, Elizabeth J. Smythe, Steven G. Johnson, Federico Capasso, and John D. Joannopoulos. "Evanescent-wave bonding between optical waveguides." *Optics letters* 30, no. 22 (2005): 3042-3044.

[18] Van, V., T. A. Ibrahim, P. P. Absil, F. G. Johnson, R. Grover, and P-T. Ho. "Optical signal processing using nonlinear semiconductor microring resonators." *IEEE Journal of Selected Topics in Quantum Electronics* 8, no. 3 (2002): 705-713.

[19] Afroozeh, Abdolkarim, Iraj Sadegh Amiri, Muhammad Arif Jalil, Mojgan Kouhnavard, Jalil Ali, and P. Preecha Yupapin. "Multi soliton generation for enhance optical communication." In *Applied Mechanics and Materials*, vol. 83, pp. 136-140. Trans Tech Publications, 2011.

[20] Levy, Jacob S., Alexander Gondarenko, Mark A. Foster, Amy C. Turner-Foster, Alexander L. Gaeta, and Michal Lipson. "CMOS-compatible multiple-wavelength oscillator for on-chip optical interconnects." *Nature photonics* 4, no. 1 (2010): 37-40.

[21] Armaroli, Andrea, Stefania Malaguti, Gaetano Bellanca, Stefano Trillo, Alfredo de Rossi, and Sylvain Combrié. "Oscillatory dynamics in nanocavities with noninstantaneous Kerr response." *Physical Review A* 84, no. 5 (2011): 053816.

[22] Malaguti, Stefania, Gaetano Bellanca, Alfredo de Rossi, Sylvain Combrié, and Stefano Trillo. "Self-pulsing driven by two-photon absorption in semiconductor nanocavities." *Physical Review A* 83, no. 5 (2011): 051802.

[23] Prabhu, Ashok M., Alan Tsay, Zhanghua Han, and Vien Van. "Ultracompact SOI microring add–drop filter with wide bandwidth and wide FSR." *IEEE Photonics Technology Letters* 21, no. 10 (2009): 651-653.

[24] Van, V., T. A. Ibrahim, K. Ritter, P. P. Absil, F. G. Johnson, R. Grover, J. Goldhar, and P-T. Ho. "All-optical nonlinear switching in GaAs-AlGaAs microring resonators." *IEEE Photonics Technology Letters* 14, no. 1 (2002): 74-76.

[25] Cardenas, Jaime, Mark A. Foster, Nicolás Sherwood-Droz, Carl B. Poitras, Hugo LR Lira, Beibei Zhang, Alexander L. Gaeta, Jacob B. Khurgin, Paul Morton, and Michal Lipson. "Wide-bandwidth continuously tunable optical delay line using silicon microring resonators." *Optics express* 18, no. 25 (2010): 26525-26534.

[26] De Vos, Katrien, Irene Bartolozzi, Etienne Schacht, Peter Bienstman, and Roel Baets. "Silicon-on-Insulator microring resonator for sensitive and label-free biosensing." *Optics express* 15, no. 12 (2007): 7610-7615.

[27] Zhang, Lin, Yunchu Li, Jeng-Yuan Yang, Muping Song, Raymond G. Beausoleil, and Alan E. Willner. "Silicon-based microring resonator modulators for intensity

modulation." *IEEE Journal of Selected Topics in Quantum Electronics* 16, no. 1 (2010): 149-158.

[28] Poon, Joyce KS, Jacob Scheuer, Shayan Mookherjea, George T. Paloczi, Yanyi Huang, and Amnon Yariv. "Matrix analysis of microring coupled-resonator optical waveguides." *Optics express* 12, no. 1 (2004): 90-103.

[29] Afroozeh, A., I. S. Amiri, K. Chaudhary, J. Ali, and P. P. Yupapin. "Analysis of optical ring resonator." *Journal of Optics Research* 16, no. 2 (2014): 135.

[30] Melloni, Andrea, Francesco Morichetti, and Mario Martinelli. "Linear and nonlinear pulse propagation in coupled resonator slow-wave optical structures." *Optical and Quantum Electronics* 35, no. 4 (2003): 365-379.

[31] Dumeige, Yannick, Carole Arnaud, and Patrice Feron. "Combining FDTD with coupled mode theories for bistability in micro-ring resonators." *Optics Communications* 250, no. 4 (2005): 376-383.

[32] Heebner, John E., and Robert W. Boyd. "Enhanced all-optical switching by use of a nonlinear fiber ring resonator." *Optics letters* 24, no. 12 (1999): 847-849.

[33] Rukhlenko, Ivan D., Malin Premaratne, and Govind P. Agrawal. "Analytical study of optical bistability in silicon ring resonators." *Optics letters* 35, no. 1 (2010): 55-57.

[34] Chamorro-Posada, P., P. Martín-Ramos, J. Sánchez-Curto, J. C. Garcia-Escartin, J. A. Calzada, C. Palencia, and A. Durán. "Nonlinear dynamics of a coupled micro-

ring resonator chain." *arXiv preprint arXiv:1012.3286* (2010).

[35] Maes, Bjorn, Martin Fiers, and Peter Bienstman. "Self-pulsing and chaos in short chains of coupled nonlinear microcavities." *Physical Review A* 80, no. 3 (2009): 033805.

[36] Grigoriev, Victor, and Fabio Biancalana. "Resonant self-pulsations in coupled nonlinear microcavities." *Physical Review A* 83, no. 4 (2011): 043816.

[37] Li, Hongpu, and Kazuhiko Ogusu. "Analysis of optical instability in a double-coupler nonlinear fiber ring resonator." *Optics communications* 157, no. 1 (1998): 27-32.

[38] Levy, Jacob S., Mark A. Foster, Alexander L. Gaeta, and Michal Lipson. "Harmonic generation in silicon nitride ring resonators." *Optics express* 19, no. 12 (2011): 11415-11421.

[39] Sanati, P., A. Afroozeh, I. S. Amiri, J. Ali, and Lee Suan Chua. "Femtosecond pulse generation using microring resonators for eye nano surgery." *Nanoscience and Nanotechnology Letters* 6, no. 3 (2014): 221-226.

[40] Xu, Qianfan, and Michal Lipson. "All-optical logic based on silicon micro-ring resonators." *Optics express* 15, no. 3 (2007): 924-929.

[41] Tanaram, C., C. Teeka, R. Jomtarak, P. P. Yupapin, M. A. Jalil, I. S. Amiri, and J. Ali. "ASK-to-PSK generation based on nonlinear microring resonators coupled to one MZI arm." *Procedia Engineering* 8 (2011): 432-435.

[42] Zhou, Linjie, Hui Chen, and Andrew W. Poon. "On-chip NRZ-to-PRZ format conversion using narrow-band silicon microring resonator-based notch filters." *Journal of lightwave technology* 26, no. 13 (2008): 1950-1955.

[43] Su, Zhaopin, Shiguo Lian, Guofu Zhang, and Jianguo Jiang. "Chaos-Based Video Encryption Algorithms." In Chaos-Based Cryptography, pp. 205-226. Springer Berlin Heidelberg, 2011.

[44] Hayashi, Shin'ichiro, et al. "Ultrabright continuously tunable terahertz-wave generation at room temperature." Scientific reports 4 (2014): srep05045..

[45] Matsko, A. B., A. A. Savchenkov, D. Strekalov, V. S. Ilchenko, and L. Maleki. "Review of applications of whispering-gallery mode resonators in photonics and nonlinear optics." *IPN Progress Report* 42, no. 162 (2005): 1-51.

[46] Walker, A. C. "Application of bistable optical logic gate arrays to all-optical digital parallel processing." *Applied optics* 25, no. 10 (1986): 1578-1585.

[47] Miller, D. A. B., S. D. Smith, and A. Johnston. "Optical bistability and signal amplification in a semiconductor crystal: applications of new low- power nonlinear effects in InSb." *Applied Physics Letters* 35, no. 9 (1979): 658-660.

[48] Silberberg, Yaron, and Israel Bar-Joseph. "Optical instabilities in a nonlinear Kerr medium." *JOSA B* 1, no. 4 (1984): 662-670.

[49] Abdollahi, Siamak, and Vien Van. "Analysis of optical instability in coupled microring resonators." *JOSA B* 31, no. 12 (2014): 3081-3087.

[50] Gibbs, Hyatt M., et al. "Observation of chaos in optical bistability." *Physical Review Letters* 46 (1981): 474-477

[51] Nakatsuka, H., et al. "Observation of bifurcation to chaos in an all-optical bistable system." *Physical Review Letters* 50.2 (1983): 109

[52] Konthasinghe, Kumarasiri, et al. "Self-sustained photothermal oscillations in high-finesse Fabry-Perot microcavities." *Physical Review A* 95.1 (2017): 013826.

[53] Zhang, Libin, Yonghao Fei, Tongtong Cao, Yanmei Cao, Qingyang Xu, and Shaowu Chen. "Multibistability and self-pulsation in nonlinear high-Q silicon microring resonators considering thermo-optical effect." *Physical Review A* 87, no. 5 (2013): 053805.

[54] Van Vaerenbergh, Thomas, Martin Fiers, Joni Dambre, and Peter Bienstman. "Simplified description of self-pulsation and excitability by thermal and free-carrier effects in semiconductor microcavities." *Physical Review A* 86, no. 6 (2012): 063808.

[55] Petrácek, Jirí, Yasa Ekşioğlu, and Anna Sterkhova. "Simulation of self-pulsing in Kerr-nonlinear coupled ring resonators." *Optics Communications* 318 (2014): 147-151.

[56] Yariv, Amnon, et al. "Coupled-resonator optical waveguide:? a proposal and analysis." *Optics letters* 24.11 (1999): 711-713.

[57] Chamorro-Posada, P., et al. "Nonlinear Bloch modes, optical switching and Bragg

solitons in tightly coupled micro-ring resonator chains." *Journal of Optics* 14.1 (2012): 015205.

[58] Kaneko, Kunihiko. "Coupled map lattice." *Chaos, Order, and Patterns*. Springer US, 1991. 237-247.

[59] Kuznetsov, S. P., and A. S. Pikovskii. "Universality of period doubling bifurcation in one-dimensional dissipative media." *Radiophysics and Quantum Electronics* 28.3 (1985): 205-214.

[60] Kapral, Raymond, and Simon J. Fraser. "Chaos and complexity in chemical systems." *Encyclopedia of Chemical Physics and Physical Chemistry* 3 (2001): 2737.

[61] Yariv, Amnon. "Universal relations for coupling of optical power between microresonators and dielectric waveguides." *Electronics letters* 36.4 (2000): 321-322.

[62] Agrawal, Govind P. *Nonlinear fiber optics*. Academic press, 2007.

[63] Xu, Dan-Xia, et al. "Silicon photonic integration platform—Have we found the sweet spot?." *IEEE Journal of Selected Topics in Quantum Electronics* 20.4 (2014): 189-205.

[64] Asobe, Masaki. "Nonlinear optical properties of chalcogenide glass fibers and their application to all-optical switching." *Optical Fiber Technology* 3, no. 2 (1997): 142-148.

[65] Deen, M. Jamal, and P. K. Basu. "Introduction to Silicon Photonics." *Silicon Photonics: Fundamentals and Devices*: 1-12.

[66] Schulz, S. A., Liam O'Faolain, Daryl M. Beggs, T. P. White, A. Melloni, and Thomas F. Krauss. "Dispersion engineered slow light in photonic crystals: a comparison." *Journal of Optics* 12, no. 10 (2010): 104004.

[67] Yin, Lianghong. *Study of nonlinear optical effects in silicon waveguides*. Diss. University of Rochester, 2009.

[68] Dekker, R., et al. "Ultrafast Kerr-induced all-optical wavelength conversion in silicon waveguides using 1.55 μm femtosecond pulses." *Optics express* 14.18 (2006): 8336-8346.

[69] Kim, Inwoong. "Synchronization In Advanced Optical Communications." (2006).

[70] Argyris, Apostolos, et al. "Chaos-based communications at high bit rates using commercial fibre-optic links." *Nature* 438.7066 (2005): 343-346..

[71] Yonenaga, K., et al. "Optical duobinary transmission system with no receiver sensitivity degradation." *Electronics Letters* 31.4 (1995): 302-304.

[72] Abrams, Daniel M., Alex Slawik, and Kartik Srinivasan. "Nonlinear oscillations and bifurcations in silicon photonic microresonators." *Physical review letters* 112.12 (2014): 123901.

[73] Zhang, Libin, et al. "Experimental observations of thermo-optical bistability and self-pulsation in silicon microring resonators." *JOSA B* 31.2 (2014): 201-206.

[74] Little, Brent E., et al. "Microring resonator channel dropping filters." *Journal of lightwave technology* 15.6 (1997): 998-1005.

[75] Van, Vien. "Circuit-based method for synthesizing serially coupled microring filters." *Journal of lightwave technology* 24.7 (2006): 2912.

[76] Levy, Jacob. "Integrated nonlinear optics in silicon nitride waveguides and resonators." (2011).

[77] Dorf, Richard C., and Robert H. Bishop. *Modern control systems*. Pearson, 2011.

[78] Meystre, Pierre, and Murray Sargent. *Elements of quantum optics*. Springer Science & Business Media, 2013.

[79] Zakery, A., and S. R. Elliott. "An introduction to chalcogenide glasses." Optical Nonlinearities in Chalcogenide Glasses and Their Applications, 1-28 (2007).

[80] Agrawal, Govind P. "Fiber-Optic Communication Systems, A John Wiley & Sons." *Inc., Publication* (2002).

[81] Xu, Qianfan, and Michal Lipson. "Carrier-induced optical bistability in silicon ring resonators." *Optics letters* 31.3 (2006): 341-343.

[82] Apiratikul, Paveen, Andrea M. Rossi, and Thomas E. Murphy. "Nonlinearities in porous silicon optical waveguides at 1550 nm." *Optics express* 17.5 (2009): 3396-3406.

[83] Nedeljkovic, Milos, Richard Soref, and Goran Z. Mashanovich. "Free-Carrier Electro refraction and Electro absorption Modulation Predictions for Silicon Over

the 1–14-μm Infrared Wavelength Range." *IEEE Photonics Journal* 3.6 (2011): 1171-1180.

[84] Huang, Chenguang, Jiahua Fan, and Lin Zhu. "Dynamic nonlinear thermal optical effects in coupled ring resonators." *AIP Advances* 2.3 (2012): 032131.

[85] Armaroli, Andrea, Patrice Feron, and Yannick Dumeige. "Stable integrated hyper-parametric oscillator based on coupled optical microcavities." *Optics letters* 40.23 (2015): 5622-5625.

[86] Grigoriev, Victor. "Coupled-mode theory for nonlinear multilayered structures and its applications in the design of all-optical devices." (2012).

[87] Pavesi, Lorenzo, and David J. Lockwood. *Silicon photonics*. Vol. 1. Springer Science & Business Media, 2004.

[88] Yanagita, Tatsuo, and Kunihiko Kaneko. "Coupled map lattice model for convection." *Physics Letters A* 175.6 (1993): 415-420.

[89] Kaneko, Kunihiko. "Spatiotemporal intermittency in coupled map lattices." *Progress of Theoretical Physics* 74.5 (1985): 1033-1044..

[90] Wang, Yong, et al. "One-way hash function construction based on 2D coupled map lattices." *Information Sciences* 178.5 (2008): 1391-1406.

[91] Freeman, Walter J. "Tutorial on neurobiology: from single neurons to brain chaos." *International journal of bifurcation and chaos* 2.03 (1992): 451-482.

[92] Zhang, Ying-Qian, and Xing-Yuan Wang. "A symmetric image encryption

algorithm based on mixed linear–nonlinear coupled map lattice." *Information Sciences* 273 (2014): 329-351.

[93] Wolfram, Stephen. *Theory and applications of cellular automata*. Vol. 1. Singapore: World scientific, 1986.

[94] Kazeto Shimonishi, Junya Hirose, and Takashi Iba, "Applying New Visualization Method to Coupled Chaotic Systems,".

[95] Houlrik, Jens M., Itzhak Webman, and Mogens H. Jensen. "Mean-field theory and critical behavior of coupled map lattices." *Physical Review A* 41.8 (1990): 4210.

[96] Liu, Y., and H. K. Tsang. "Nonlinear absorption and Raman gain in helium-ion-implanted silicon waveguides." *Optics letters* 31.11 (2006): 1714-1716.

[97] Chen, Xiaogang, Nicolae C. Panoiu, and Richard M. Osgood. "Theory of Raman-mediated pulsed amplification in silicon-wire waveguides." *IEEE journal of quantum electronics* 42.2 (2006): 160-170.

[98] Sang, Xinzhu, En-Kuang Tien, and Ozdal Boyraz. "Applications of two photon absorption in silicon." *Journal of optoelectronics and advanced materials* 11.1 (2009): 15.

[99] Reed, Graham T. "Device physics: the optical age of silicon." *Nature* 427, no. 6975 (2004): 595-596.

[100] Yin, Lianghong, and Govind P. Agrawal. "Impact of two-photon absorption on self-phase modulation in silicon waveguides." *Optics letters* 32, no. 14 (2007):

2031-2033.

[101] Sang, Xinzhu, En-Kuang Tien, and Ozdal Boyraz. "Applications of two photon absorption in silicon." *Journal of optoelectronics and advanced materials* 11, no. 1 (2009): 15.

[102] Reed, Graham T., and Andrew P. Knights. *Silicon photonics: an introduction*. John Wiley & Sons, 2004.

[103] Goudon, Thierry, Vera Miljanović, and Christian Schmeiser. "On the Shockley–Read–Hall Model: generation-recombination in semiconductors." *SIAM Journal on Applied Mathematics* 67, no. 4 (2007): 1183-1201.

[104] PUKSEC, Julijana Divkovic. "Recombination processes and holes and electrons lifetimes." *Automatika* 43, no. 1-2 (2002): 47-53.

[105] Kerr, Mark J., and Andres Cuevas. "General parameterization of Auger recombination in crystalline silicon." *Journal of Applied Physics* 91, no. 4 (2002): 2473-2480.

[106] Arafat, Yeasir, Farseem M. Mohammedy, and MM Shahidul Hassan. "Optical and other measurement techniques of carrier lifetime in semiconductors." *Int. J. Optoelectron. Eng* 2, no. 2 (2012): 5-11.

[107] Raghunathan, Varun. *Raman-based silicon photonic devices*. University of California, Los Angeles, 2008.

[108] Salem, Reza, Mark A. Foster, Amy C. Turner, David F. Geraghty, Michal Lipson,

and Alexander L. Gaeta. "Signal regeneration using low-power four-wave mixing on silicon chip." *Nature photonics* 2, no. 1 (2008): 35-38.

[109] Masilamani, Ashok Prabhu. "Advanced silicon microring resonator devices for optical signal processing." PhD diss., University of Alberta, 2012.